Visible Light Communications with Single-Photon Avalanche Diodes

by

Ibrahim Alsolami
Balliol College

A thesis submitted in partial fulfillment of the
requirements for the degree of
Doctor of Philosophy

Department of Engineering Science
University of Oxford
April 2014

Abstract

This thesis explores the use of single-photon avalanche diodes (SPADs) for visible light communications (VLC). The high sensitivity of SPADs can potentially enhance the performance of VLC receivers. However, a SPAD-based system has challenges that need to be addressed before it can be considered as a viable option for VLC.

The first challenge is the susceptibility of SPAD-based receivers to variations in ambient light. The high sensitivity of SPADs is advantageous for signal detection, but also makes SPADs vulnerable to variations in ambient light. In this thesis, the performance of a SPAD-based receiver is investigated under changing lighting conditions. Analytical expressions to quantify performance are derived, and an experiment is conducted to gain further understanding of system performance. It is shown that a SPAD-based receiver is highly sensitive to illumination changes when on-off keying (OOK) is employed, and that pulse-position modulation (PPM) is a preferred modulation scheme as it is more robust.

The second challenge is broadcasting to SPAD-based receivers with different capabilities. A traditional broadcasting scheme is time-sharing, whereby a transmitter sends data to receivers in an alternating manner. Broadcasting to SPAD-based receivers is challenging as receivers may have diverse capabilities. In this thesis, a new multiresolution modulation scheme is proposed, which can potentially improve system performance over the traditional time-sharing approach. The performance of the proposed scheme is analyzed, and a proof-of-concept experiment is performed to demonstrate its viability.

Acknowledgements

I would like to thank my dear mother, Aziza Alharbi, father, Mohammed Alsolami, sister, Sana Alsolami, and brother, Walid Alsolami, for their constant support, encouragement, and kindness throughout the years. I can't be grateful enough.

I would like to thank my supervisor Prof. Dominic O'Brien for his insightful comments, enthusiasm, and guidance. Special thanks to Dr Steve Collins for the fruitful discussions we had over the past years, and his continuous support. I'm eternally grateful to Dr Danial Chitnis for his comments, suggestions, and technical advice.

Many thanks to the staff of Balliol College for their assistance, and great efforts. I am deeply indebted to Glynis Price for her help when I first arrived at Oxford.

Last, but not least, I would like to thank my friends for the good times we had. My time in Oxford will always be looked back on with a smile and fondness.

Thank you all!

Ibrahim Alsolami
Holywell Manor, Oxford
April, 2014

Dedication

This thesis is dedicated to

my dear Mother, Father, Sister, and Brother.

Contents

List of Tables

List of Figures

List of Abbreviations

APD	Avalanche Photodiode
BEP	Bit-Error Probability
BER	Bit-Error Rate
FWHM	Full Width at Half Maximum
IM/DD	Intensity Modulation and Direct Detection
LED	Light-Emitting Diode
MAP	Maximum a Posteriori Probability
OOK	On-Off Keying
PDP	Photon-Detection Probability
PMT	Photonmultiplier tube
PPM	Pulse-Position Modulation
RF	Radio-Frequency
SNR	Signal-to-Noise Ratio
SPAD	Single-Photon Avalanche Diode
VLC	Visible Light Communications

Chapter 1

Introduction

Chapter Overview

The chapter begins with a discussion about the growing demand for spectrum, and the potential that lies within visible light communication (VLC) systems. This chapter also includes a discussion about the likely future of light-emitting diodes (LEDs) and VLC. Components of a VLC system are described in this chapter, and how VLC works is explained. This chapter also gives an overview of efforts made towards the development of VLC. The chapter concludes with a description of the thesis's objective, and a summary of the contributions made.

1.1 The need for VLC

Nowadays, wireless access to the Internet is becoming an important utility in our daily lives - just like electricity and water. Over the past years, radio-frequency (RF) systems, such as Wi-Fi, have successfully provided wireless access to end-users. However, RF systems are now facing a great challenge: the RF spectrum is becoming crowded. With the number of wireless devices increasing each year, a congestion crisis is looming.

Worldwide, the demand for spectrum is growing rapidly. The volume of data traffic generated by mobile devices is expected to grow by 6-fold between 2014 and 2018. Forecasts indicate that by the end of 2014 there will be more mobile-connected devices than people on the planet (7.2 billion). By 2018 it is estimated that there will be nearly 10 billion mobile-connected devices (1.4 per capita) [1, 2]. This rapid growth needs to be sustained by an equivalent growth in spectrum bandwidth. However, the RF spectrum is now scarce. It is anticipated that by 2020 Wi-Fi networks in the UK could face a "spectrum crunch" [3], should current trends continue.

The vast spectrum available to visible light communication[1] (VLC) can potentially accommodate the growing number of wireless devices. The visible light spectrum is about 10^4 times larger than the RF spectrum [4]. With this immense spectrum VLC can offer much higher data rates than are currently possible. Recently, data rates up to 10 $Gbits/sec$ have been experimentally demonstrated [5]. VLC is still in its infancy; however, it shows a great potential for wireless communication.

[1] VLC is defined as wireless communications that uses wavelengths visible to the human eye (380-780 nm).

1.2 The Future of LEDs and VLC

Recent trends indicate that VLC might be the next-generation indoor wireless communication technology. Currently, indoor lighting is shifting away from incandescent and fluorescent lamps to light-emitting diodes (LEDs). Power-efficiency, reliability, and brightness are just a few of the appealing features of LEDs [6, 7, 8]. It is now possible to purchase LED bulbs for home use [9]. The vision is that LEDs will be simultaneously used for indoor illumination and wireless communication [10, 11, 12].

In the future, LEDs will be prevalent in homes and offices. Haitz's Law - alike Moore's Law but for LEDs - states that every 10 years the amount of light an LED produces increases by a factor of 10, while its cost-per-lumen decreases by a factor of 20 [13]. In other words, LEDs become brighter and cheaper over time. As Haitz's Law continues to progress, it is likely that LEDs will become more widespread and their use for VLC will increase.

1.3 Visible Light Communications

Figure 1.1 depicts a VLC system. The transmitter modulates the intensity of light by a laser or LED, and uses shaping optics to spread light over a large area. The channel is the medium through which light travels. This channel adds noise to the transmitted signal, which could be from sunlight or artificial illumination. The receiver uses a lens to collect the incoming light and focuses it on a photodiode detector. The detector produces a photocurrent signal from which a data stream can be extracted by a decision-making device.

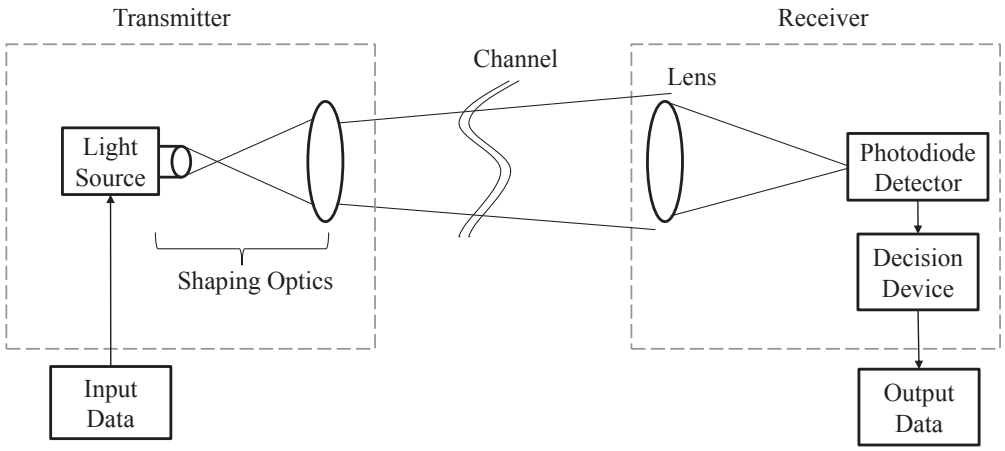

Figure 1.1: Visible light communication system.

This transmission/reception scheme is known as intensity modulation and direct detection (IM/DD). By far IM/DD is the most widely used scheme in optical communications as it is costly to build oscillators, for coherent communication, at optical frequencies [14].

Some of the attractive features of VLC are:

- The spectrum available to VLC is vast ($\sim$ 400 THz wide [15]).
- The bandwidth of VLC lies in a spectrum that is unlicensed [16]. This allows immediate deployment.
- RF signals can cause electromagnetic interference in electronic instruments, whereas VLC signals do not. This makes VLC suitable for use in sensitive areas such as airplanes [17].

However, these attractive features carry with them some drawbacks, namely:

- Ambient light, such as sunlight, can interfere with VLC systems; hence, impair performance [18].
- Unlike its RF counterpart, VLC systems are vulnerable to obstruction [19].
- Eye safety requirements limit the power that can be used by a VLC system [20].

In addition to wireless access to the Internet, VLC has a number of potential applications:

- *Indoor Positioning*:

  A promising application for VLC is indoor localization and navigation. Signals from GPS[2] satellites are usually unavailable in indoor environments, and RF systems are inaccurate due to multipath propagation [21]. However, VLC can potentially provide users with a centimetre-level position accuracy [22, 23], as the optical signal it uses is highly directional.

- *Vehicle Safety*:

  Vehicle-to-vehicle communications seeks to improve road safety. Collision-avoidance and lane-change-assistance are some of the safety features this technology could bring. However, it is required from this technology to meet some stringent specifications before it can be deployed. For example, restricting the latency to no more than 100 msec and a

[2]Global Positioning System.

communication range of 150 m [24]. VLC has the potential to satisfy these requirements [25]. Nowadays, LEDs can now be found in headlights and taillights of cars. With these LEDs, VLC can realize vehicle-to-vehicle communications [26, 27].

- *Underwater Communication*

  Underwater communication has received much research attention over the past few years. Applications range from offshore exploration to seismic monitoring [28, 29]. Seawater has a high absorption coefficient for optical signals except for wavelengths between 400-500 nm [30]. This bandwidth lies in the visible light spectrum, thus giving VLC a unique advantage in undersea communication.

1.4 Development of VLC

The concept of using visible light LEDs for wireless communications was introduced in 1999 by Pang *et al.* [31]. However, it was Komine *et al.* that suggested that LEDs used for indoor illumination can be simultaneously used for wireless communications [32, 33]. Today, some 15 years later, VLC has thrived. Research groups now exist worldwide, standards have been released [15, 34, 35], and commercialization of VLC has begun [36, 37].

To promote VLC, consortiums have been formed. In 2003 the visible light communications consortium (VLCC) was founded, followed by the light-fidelity (Li-Fi) consortium in 2011. Research, development and standardization of VLC are among the missions of the consortiums [38, 39].

Research projects towards the development of VLC have been undertaken. Characteristics of indoor VLC channels have been analyzed [40]. The feasibility of wireless communications using LEDs in the presence of high room illumination was experimentally verified [41, 42]. In [43], it was shown that a commercial off-the-shelf LED can deliver ~ 100 Mbit/sec. Parallel transmission in VLC requires alignment between transmitters and receivers to prevent crosstalk, and thus limits a receiver's mobility. This alignment restraint, however, can be removed by using multiple-input multiple-output (MIMO) signal processing [44, 45, 46]. The potential of orthogonal frequency division multiplexing (OFDM) to enhance data rates was investigated [47, 48]; it was recently shown that a single LED can deliver 3 Gbits/sec by OFDM [49].

1.5 Thesis Overview and Contributions

Photon-counting receivers are potentially attractive for VLC as they offer high link margins. Historically, photon-counting receivers relied on photonmultiplier tubes (PMTs). However, PMTs are bulky [50], and thus are not suitable for wireless communications. Today, single-photon avalanche diodes (SPADs) are providing a low-cost solid-state alternative for photon detection [51, 52]. However, there has been little research about employing SPADs in VLC systems (see, e.g., [53, 54]). This thesis explores the use of SPADs for VLC.

In *Chapter 2*, a general architecture of a SPAD-based VLC system is described, and its operating principles are explained. In *Chapter 3*, the

performance of a SPAD-based receiver is investigated under changing lighting conditions. *Chapter 4*, investigates broadcasting to SPAD-based receivers. A scheme is proposed to improve system throughput, when receivers with diverse capabilities share a common downlink channel. The performance of the proposed scheme is analyzed, and a proof-of-concept experiment is performed to demonstrate its viability. In *Chapter 5*, conclusions from the project are drawn.

The contributions of this thesis are the following:

- Analysis of the performance of a SPAD-based receiver under changing lighting conditions.
- Experimental assessment of the performance of a SPAD-based receiver under changing lighting conditions.
- Design of a multiresolution PPM, M/N-PPM, scheme to improve data rates when broadcasting to SPAD-based receiver with different slot durations [55].
- Analysis of the performance of the proposed M/N-PPM scheme [55].
- Experimental demonstration of the capability of the proposed M/N-PPM scheme [56].

Chapter 2

Communication System and Operation Principles

Chapter Overview

This chapter begins with a discussion on the operating principles of single-photon avalanche diodes (SPADs). The structure of a SPAD-based VLC system is presented, and figures of merit used to quantify its performance are explained. Simulation results are also provided and examined with respect to theory.

2.1 Single-Photon Avalanche Diodes

Single photon detection has traditionally relied on photonmultiplier tubes (PMTs). However, PMTs are bulky, require high voltages, and are sensitive to vibration [50, 57]; thus, are not suitable for communication systems. Today, single-photon avalanche diodes (SPADs) are providing a solid-state alternative for photon detection [51, 52]. High-sensitivity, low noise, and compactness are just some of the attractive features of SPADs. Nowadays, SPADs are finding many applications ranging from VLC [58] to quantum key distribution [59].

SPADs are avalanche photodiodes (APDs). What distinguishes SPADs from other APDs is that they are specially designed to operate with a reverse-bias voltage beyond the breakdown voltage [60]. This mode of operation is commonly referred to as the Geiger-mode [61]. In this mode, a single photon can trigger a signal of large-amplitude and short-duration.

Figure 2.1 shows a SPAD in a circuit, and Figure 2.2 shows its I-V characteristic curve. When in reverse-bias mode, a high electric field is established across a SPAD's p-n junction. Once a photon is absorbed in the electric field region an electron-hole pair is produced. The electric field drifts electrons towards the n side of the junction, and the holes towards the p side of the junction. As electrons, or holes, accelerate in the junction they gain kinetic energy. If the energy they gain is sufficient they can produce more electron-hole pairs as they collide with the crystal lattice. The secondarily created electrons and holes (and primary as well) can further generate electron-hole

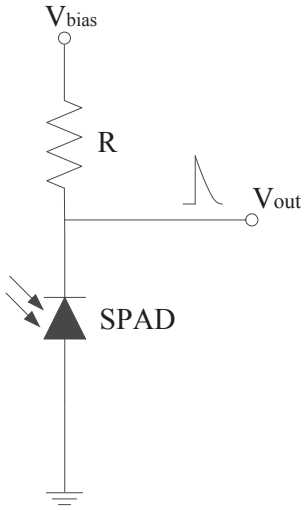

Figure 2.1: SPAD and circuitry for passive quenching.

pairs [62]. This creates an avalanche current that swiftly rises and continues flowing until the reverse-bias voltage across the SPAD is lowered by the series resistor. The resistor quenches the avalanche current, that is, it brings the SPAD out of the breakdown region (Figure 2.2). After the SPAD is quenched, it begins to recharge until the voltage across it reaches the reverse-bias voltage level. The SPAD then becomes ready to detect a new photon. The SPAD in Figure 2.1 is passively quenched. Another method to quench the SPAD is called active quenching. Figure 2.3 illustrates this method. An electronic controller senses an avalanche current and switches on a quenching voltage. The quenching voltage lowers the reverse-bias across the SPAD to a level below the breakdown voltage. Once the SPAD is quenched, the controller resets the SPAD to its initial state, where it recharges [63, 64].

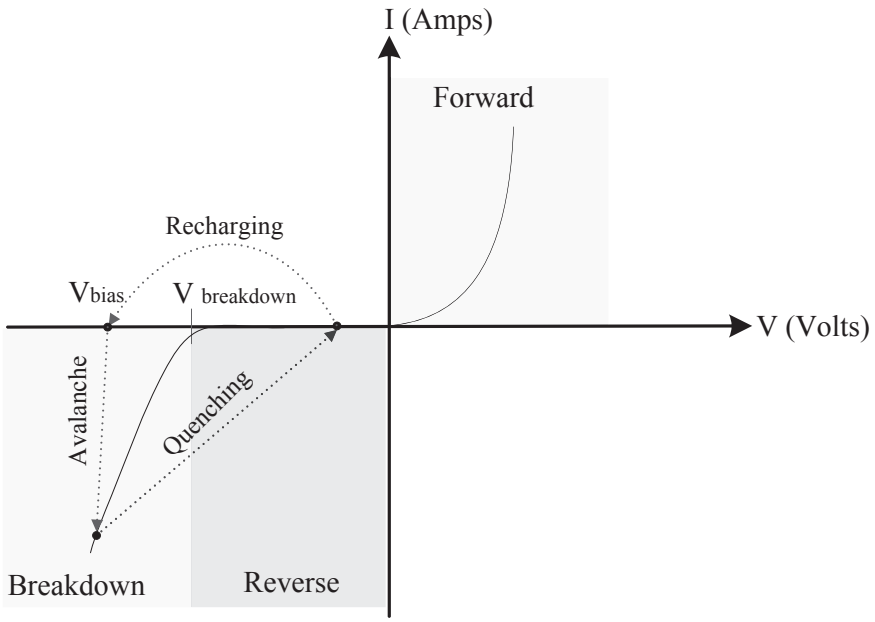

Figure 2.2: I-V characteristic curve.

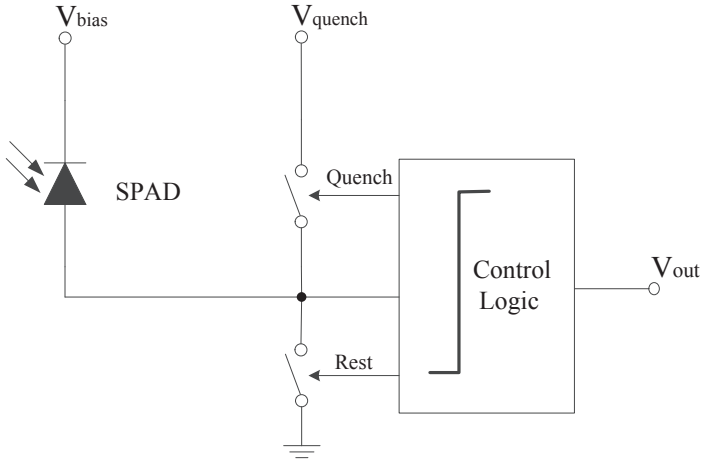

Figure 2.3: Active quenching of SPAD. Reproduced from [63] with modifications.

The impairments of a SPAD-based receiver are the following:

- *Afterpulsing*: temporarily trapped charges in defects of SPADs' *p-n* junctions can be released after a photon is detected. This phenomenon is known as afterpulsing [65]. Pulses generated by these charges are indistinguishable from signal pulses, and hence give rise to false photon counts.

- *Dark counts*: are false photon counts that arise in the absence of light incident on the SPAD. This noise is highly temperature dependent and thus can be reduced by cooling the SPAD [63]. Cooling is used in commercial SPADs, such as the one used in later experiments (*Chapter* 3).

- *Dead time*: a SPAD needs recovery time to reset to its initial state after an avalanche event. This period of time is called dead time [66]. There are two types of dead time: extensible and non-extensible [67]. Figure 2.4 and Figure 2.5 provide illustrations of non-extensible and extensible dead time, respectively. The dead time for non-extensible is fixed, whereas the dead time for extensible extends with the arrival of a photon. Photons that arrive during the dead time will go undetected; if the onset of an avalanche event is used to mark the arrival of a photon. The performance of a SPAD-based communication system is highly affected by the dead time as it limits the number of photons that can be detected.

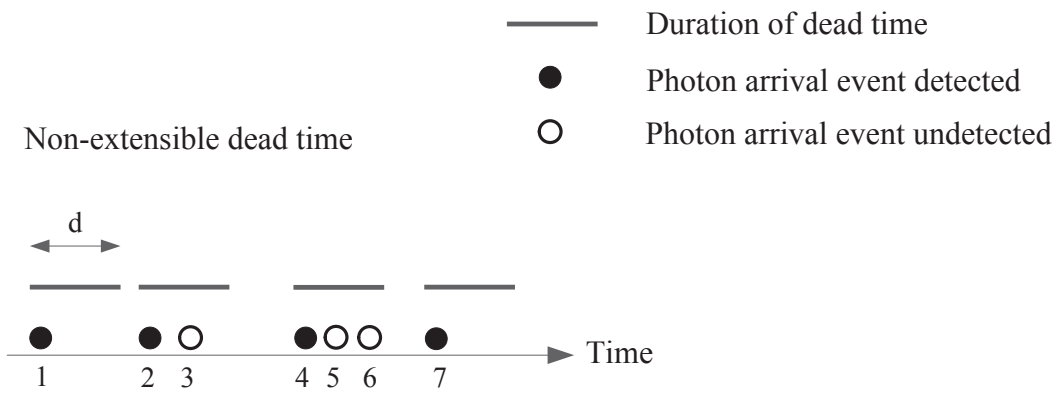

Figure 2.4: An illustration to show the effect of *non-extensible* dead time on the detection of photons. The dead time is fixed and is of duration d. Photon arrival events 1, 2, 4, and 7 are detected. However, photon arrival events 3, 5, and 6 go undetected as they lie within the dead time initiated by a previously detected photon.

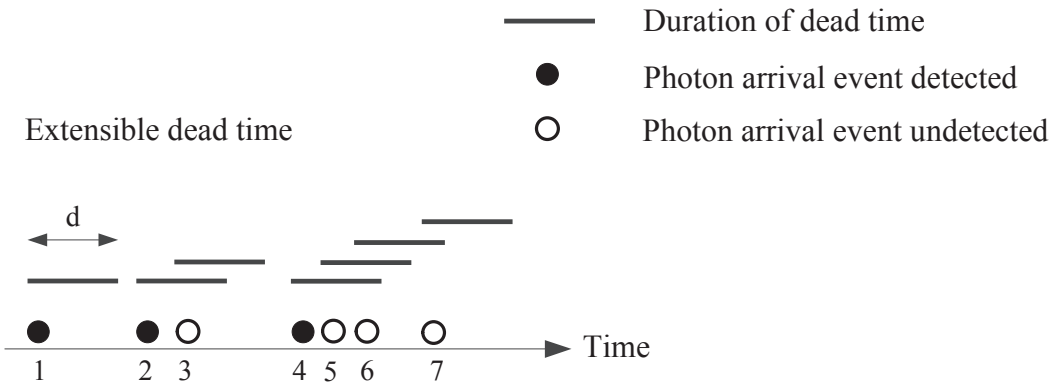

Figure 2.5: An illustration to show the effect of *extensible* dead time on the detection of photons. The dead time is of duration d and extends if a photon arrives during this period. Photon arrival events 1, 2, and 4 are detected. However, photon arrival events 3, 5, 6 and 7 go undetected as they lie within the dead time initiated by a preceding photon.

2.2 SPAD-based VLC system

Figure 2.6 shows a schematic of a SPAD-based VLC system, which consists of three main parts: a transmitter, receiver, and the channel between them. Electronics at the transmitter convert input data into a time-varying current that drives an LED. The LED emits photons, ideally, at a rate which is proportional to the input current. Photons travel through the wireless channel until they reach a SPAD at the receiver. Electronics at the receiver determine the arrival time of photons, and attempt to decode the received signal. For the low photon flux case considered here, the optical channel is modelled as a Poisson channel, given by [68, 69],

$$P(k) = \frac{\lambda^k}{k!} e^{-\lambda}, \qquad k \in \{0, 1, 2, \dots\}, \ \lambda \in [0, \infty) \tag{2.1}$$

where k is the number of photons observed in a time interval, Δt, and λ is the average number of photons observed in Δt. The impairments of the system are: a) dead time b) noise which is produced by dark counts and ambient light.

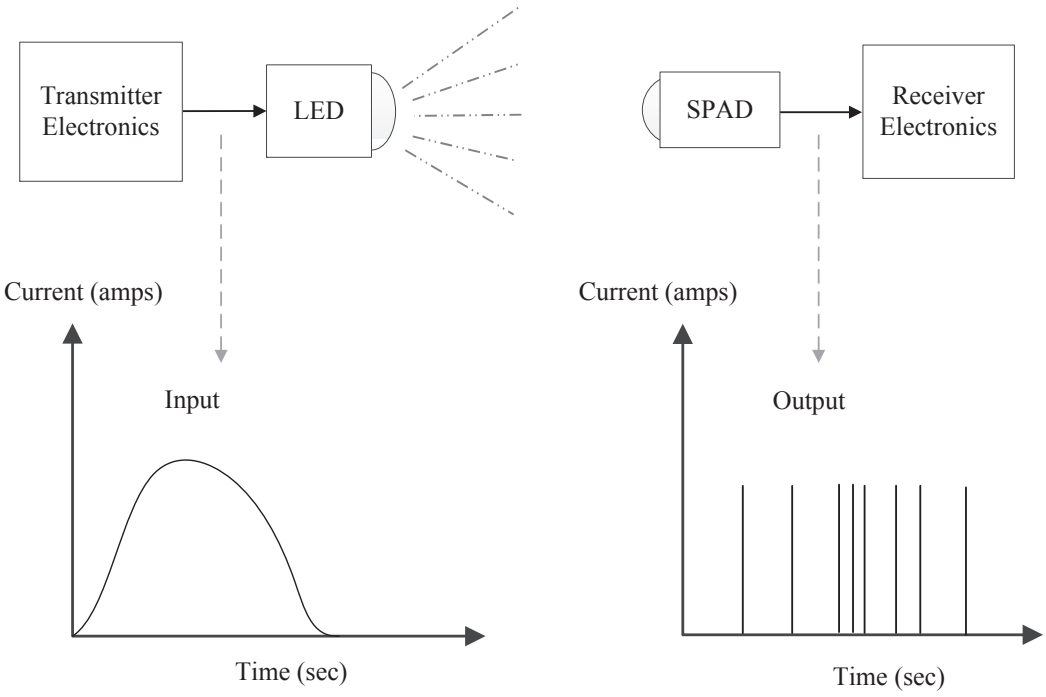

Figure 2.6: Generic structure of a SPAD-based VLC system. Spikes at the output represent short duration pulses produced by the SPAD in response to a detected photon.

2.3 Principles of Operation

Figure 2.7 shows a block diagram of an on-off keying (OOK) VLC system. In this system, an input bit is mapped to a channel symbol by an intensity modulator, such as an LED, whereby a pulse of light is used to represent binary *one* and the absence of it is used to represent binary *zero*. The modulated signal traverses the channel and noise caused by ambient light is added to it. A SPAD at the receiver end detects the incoming photons and adds dark counts to them. The number of photons detected by the SPAD in an OOK symbol is determined by a photon counter. The photon counts are then passed to a demodulator, which estimates the transmitted symbol.

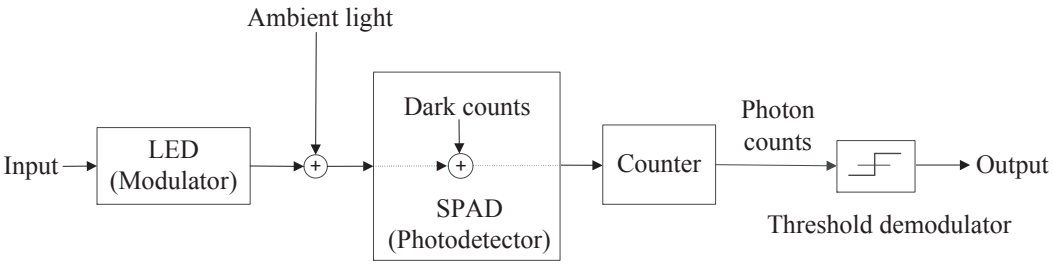

Figure 2.7: Block diagram of a SPAD-based VLC with OOK modulation.

Figure 2.8 shows a block diagram an M-ary pulse-position modulation (M-PPM) VLC system. In this system, an M-PPM encoder maps a block of $\log_2 M$ input bits to a codeword. The codeword is then passed to an intensity modulator, which sends a pulse in one of the M slots of a PPM symbol. Figure 2.9 provides an illustration of this process. The modulated signal traverses the channel and noise caused by ambient light is added to it. A SPAD at the receiver detects the incoming photons and adds dark counts

to them. A photon counter then counts the number of photons detected by the SPAD in each PPM slot, and passes the counts to a demodulator. After the elapse of a symbol duration the demodulator estimates the transmitted PPM symbol and subsequently maps it to a block of $\log_2 M$ output bits.

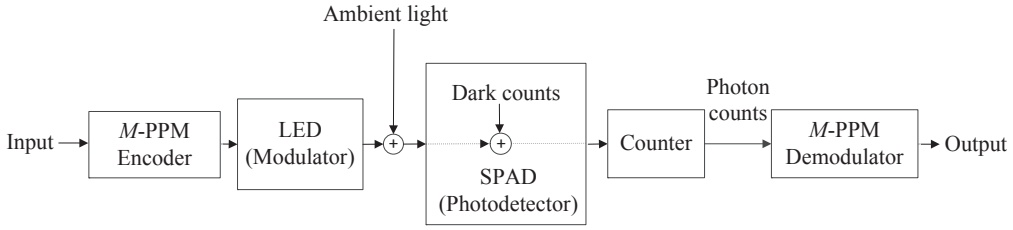

Figure 2.8: Block diagram of a SPAD-based VLC with M-PPM.

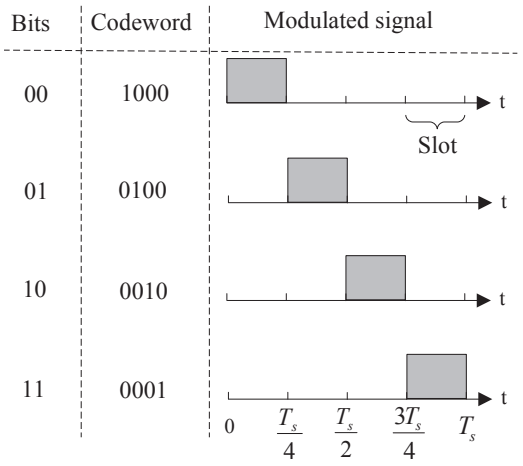

Figure 2.9: An illustration of codewords and signal set of 4-PPM. Here, T_s is the symbol duration, which is divided into four time slots of equal duration. Generally, information is encoded in M-PPM by sending a pulse in one of the M slots of an M-PPM symbol.

2.4 Figures of Merit

The following figures of merit are used to quantify the ability of a communication system:

- *Capacity*: The capacity is a fundamental limit of a communication system. It is defined as the highest rate at which a system can communicate reliably across a channel [70].
- *Photon-Efficiency*: The photon-efficiency, expressed in *bits/photon*, quantifies how well energy is used to achieve a given rate. It is defined as the amount of information conveyed on average by a photon [71].
- *Bit-Error Rate (BER)*: The BER quantifies the quality of a communication link. It is defined as the probability of an error in a received bit. Experimentally, the BER is measured by dividing the number of received bits that have errors by the total number of bits transmitted.

2.5 Simulation Results

This section provides BER simulation results to: a) predict the performance of a SPAD-based system when OOK and M-PPM are employed b) compare simulation results with theory.

Algorithm 1 and Algorithm 2 provide a step-by-step procedure to simulate the BER of OOK and PPM, respectively. Figure 2.10 - Figure 2.13 show BER simulation results, and provide a comparison with theory. The theoretical BERs for OOK and PPM were produced by using (3.30) and

(3.31), respectively. All algorithms were coded in MATLAB, with which a vector is used to represent the transmitted waveform with each element representing the number of photons (signal and/or noise) in a particular time slot. In the simulation and numerical results the value of the noise is set to $\lambda_n = 2.6 \times 10^{-4}$ and 1.5 (photons/slot), as these values are typical of those measured in later experiments (*Chapter* 3).

The accuracy of a BER simulation depends on the number of bits, L, that are simulated. The higher the value of L, the more the BER approaches its true value. However, the simulation time increases with L. Therefore, a compromise between accuracy and simulation time may be required. A practical value of L is $\frac{100}{p}$, where p is the theoretical BER [72]; this value is used in this section.

Algorithm 1 : algorithm to simulate the BER of OOK on a Poisson channel

Input: Mean value of signal photons: λ_s
Mean value of noise photons: λ_n
Probability of logic one: $P_X(1)$
Data length: L
Output: Bit-error rate
Initialize: Total number of errors $\leftarrow 0$
$A \leftarrow$ Randomly generate a bit stream of length L
$\tau \leftarrow \left\lfloor \frac{\lambda_s + \ln\left(\frac{1-P_X(1)}{P_X(1)}\right)}{\ln\left(1+\frac{\lambda_s}{\lambda_n}\right)} \right\rfloor$ % set decision threshold.
for $i \leftarrow 1$ to L **do**
  if $A(i) = 0$ **then**
    Generate the number of noise photons, $k(i)$, in an OOK slot according to the Poisson distribution: $P_K(k) = \frac{\lambda_n^k}{k!} e^{-\lambda_n}$
  else
    Generate the number of signal+noise photons, $k(i)$, in an OOK slot according to the Poisson distribution: $P_K(k) = \frac{(\lambda_s+\lambda_n)^k}{k!} e^{-(\lambda_s+\lambda_n)}$
  end if
  if $k(i) > \tau$ **then**
    $B(i) \leftarrow 1$ % decode data.
  else
    $B(i) \leftarrow 0$ % decode data.
  end if
  Error$\leftarrow A(i) \oplus B(i)$ % exclusive OR.
  Total number of errors $\leftarrow$ Total number of errors+Error
end for
Bit-error rate $\leftarrow$ Total number of errors$/L$

Algorithm 2 : algorithm to simulate the BER of PPM on a Poisson channel

Input: Mean value of signal photons: λ_s
Mean value of noise photons: λ_n
Modulation order of PPM: M
Data length: L such that $\frac{L}{\log_2 M} \in \{1, 2, 3, \dots\}$
Output: Bit-error rate
Initialize: Total number of errors $\leftarrow 0$
$A \leftarrow$ Randomly generate $\frac{L}{\log_2 M}$ numbers chosen from the set $\{0, 1, \dots, M-1\}$

$\mathbf{I} \leftarrow \begin{pmatrix} 1 & 0 & \dots & 0 \\ 0 & 1 & \dots & 0 \\ \vdots & \vdots & \ddots & \vdots \\ 0 & 0 & \dots & 1 \end{pmatrix}_{M \times M}$ % generate an identity matrix.

for $i \leftarrow 1$ to $\frac{L}{\log_2 M}$ **do**
  $D \leftarrow \mathbf{I}$(A(i)+1, 1 to M) % assign the $(A(i)+1)$th row of $\mathbf{I}$ to vector D.
  for $j \leftarrow 1$ to M **do**
    if $D(j) = 0$ **then**
      Generate the number of noise photons, $k(j)$, in the jth PPM slot according to the Poisson distribution: $P_K(k) = \frac{\lambda_n^k}{k!} e^{-\lambda_n}$
    else
      Generate the number of signal+noise photons, $k(j)$, in the jth PPM slot according to the Poisson distribution: $P_K(k) = \frac{(\lambda_s+\lambda_n)^k}{k!} e^{-(\lambda_s+\lambda_n)}$
    end if
  end for
  $B(i) \leftarrow \underset{m \in \{1,2,\dots,M\}}{\arg\max}\ k(m)$ % decode data: find the index of vector k which yields the maximum value.
  $\acute{B} \leftarrow$ Convert $(B(i)-1)$ from decimal to binary
  $\acute{A} \leftarrow$ Convert $A(i)$ from decimal to binary
  Error$\leftarrow \sum_{n=1}^{\log_2 M} \acute{A}(n) \oplus \acute{B}(n)$ % exclusive OR and summation.
  Total number of errors $\leftarrow$ Total number of errors+Error
end for
Bit-error rate $\leftarrow$ Total number of errors$/L$

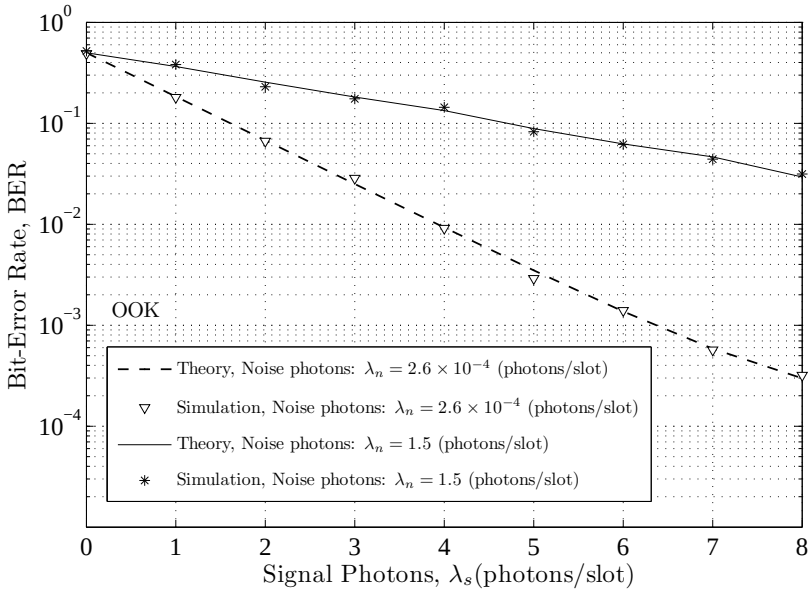

Figure 2.10: BER of OOK versus number of signal photons per slot on a Poisson channel. All modulation symbols are equiprobable.

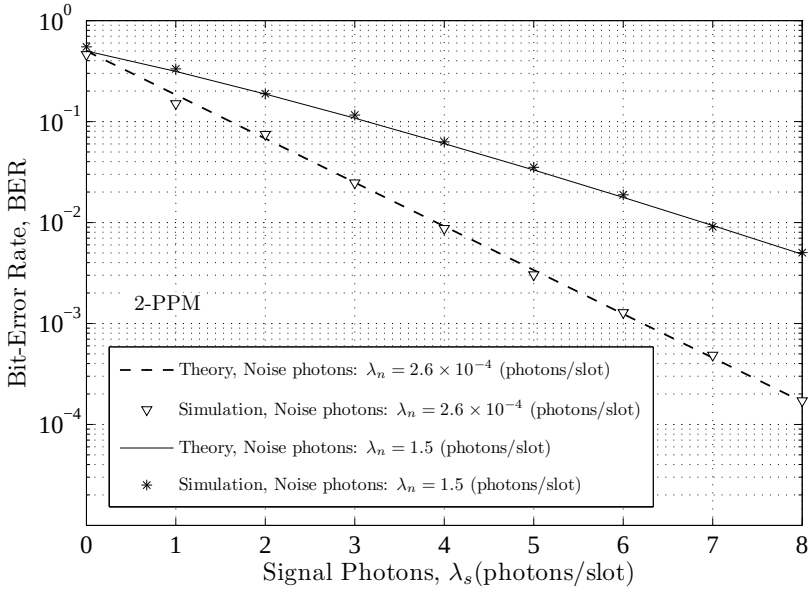

Figure 2.11: BER of 2-PPM versus number of signal photons per slot on a Poisson channel. All modulation symbols are equiprobable.

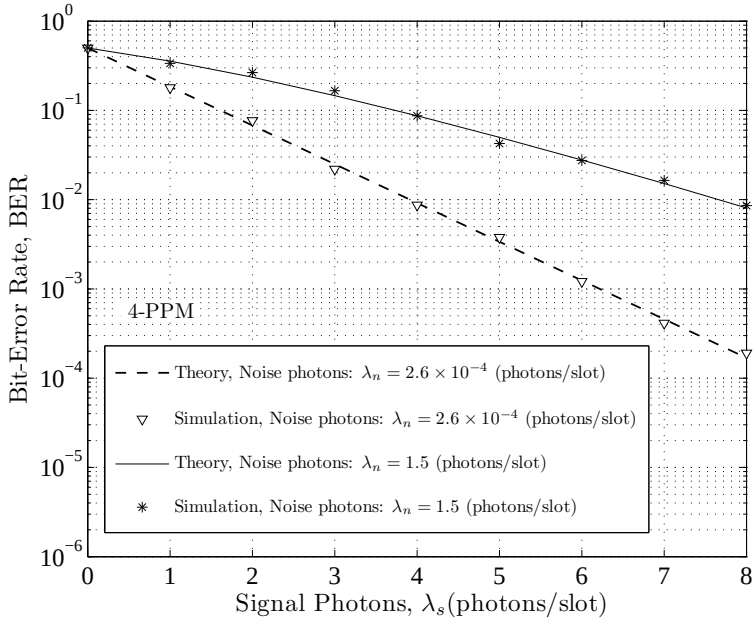

Figure 2.12: BER of 4-PPM versus number of signal photons per slot on a Poisson channel. All modulation symbols are equiprobable.

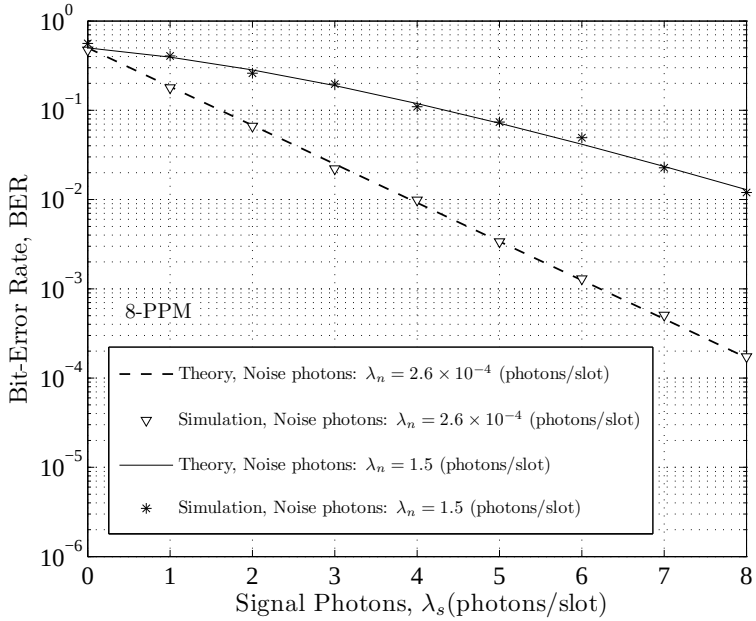

Figure 2.13: BER of 8-PPM versus number of signal photons per slot on a Poisson channel. All modulation symbols are equiprobable.

The simulation results and theory are in close agreement. In Figure 2.14, for the same number of signal photons, or average power, 2-PPM has an improved performance over OOK, since the Euclidean distance between its constellation points is larger. This is illustrated in Figure 2.15. The Euclidean distance between the constellation points of 2-PPM is $\|s_1 - s_0\| = \sqrt{2}\ \lambda_s$, whereas for OOK it is $\|s_1 - s_0\| = \lambda_s$. However, as the modulation order of PPM increases its performance degrades as more noise photons per PPM symbol are collected.

In this chapter, all modulation schemes have the same number of signal photons per slot, λ_s. In the next chapter, the performance of modulation schemes are studied when they are given the same average number of signal photons per symbol, $\bar{\mu}$.

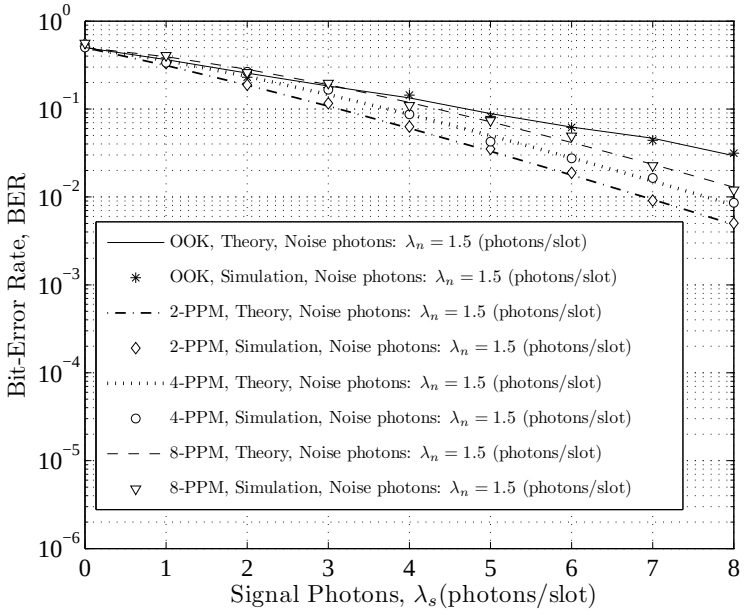

Figure 2.14: BER of OOK and M-PPM versus number of signal photons per slot on a Poisson channel. All modulation symbols are equiprobable.

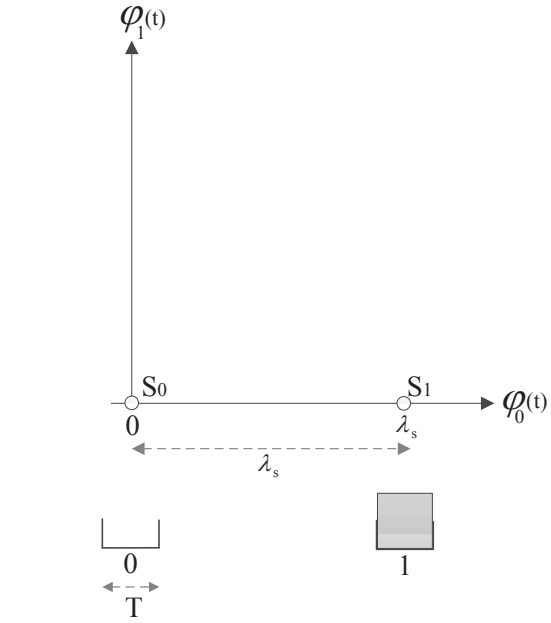

(a)

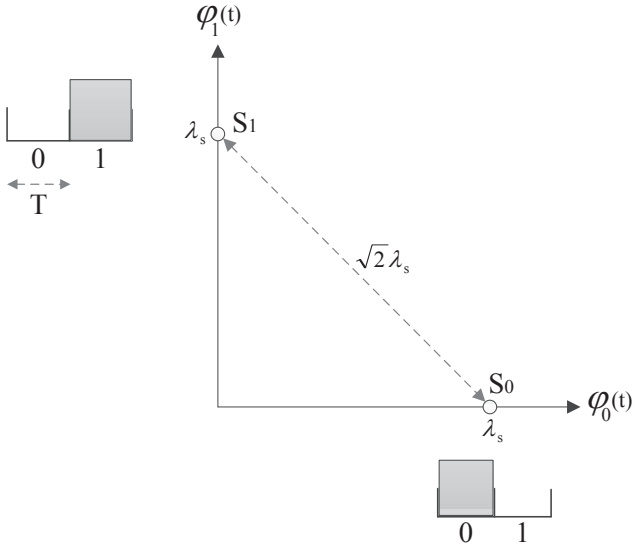

(b)

Figure 2.15: Signal space representations for: (a) OOK, (b) PPM.
$\varphi_0(t)$ and $\varphi_1(t)$ are orthonormal functions defined as:
$\varphi_0(t) = 1$ if $0 \leq t < T$ and $\varphi_0(t) = 0$ otherwise.
$\varphi_1(t) = 1$ if $T \leq t < 2T$ and $\varphi_1(t) = 0$ otherwise,
where T is the slot duration.

2.6 Conclusion

A SPAD-based VLC system operates in the photon counting regime where Poisson statistics are observed. After a photon is detected, a SPAD needs to be quenched to detect a subsequent photon. Photons that arrive during this time will go undetected. The high sensitivity of SPADs makes them a potential candidate for VLC receivers. In the next chapter, the performance of a SPAD-based VLC system will be studied.

Chapter 3

Communication over Noisy VLC Channels with SPADs

Chapter Overview

This chapter studies the performance of a SPAD-based VLC system in terms of capacity, photon-efficiency, and BER, when room illumination deviates from a given value. The problem is first studied analytically; then an experiment is conducted to gain an understanding of the performance of OOK and PPM, when SPADs are employed.

Chapter's guide to notations: we denote the set of non-negative real numbers, $[0, \infty)$, by $\mathbb{R}_0^+$, the set of natural numbers, $\{0, 1, 2, \dots\}$, by $\mathbb{N}$, and the set of non-zero natural numbers, $\mathbb{N}\backslash\{0\}$, by $\mathbb{N}^+$. Uppercase letters, *e.g.*, X, are used to denote random variables (RVs), lowercase letters, *e.g.*, x, to denote corresponding realizations of RVs, and calligraphic letters, *e.g.*, $\mathcal{X}$, to denote the alphabets of RVs. Subscripts of probability mass functions (pmf) specify the RV involved or the conditioning of a RV to another one, *e.g.*, the pmf of RV X is denoted as $P_X(x)$, whereas the conditional pmf of RV K given $X = x$ is denoted by $P_{K|X}(k|x)$. A time-index, i, is used to indicate the moment of an observation, *e.g.*, the ith outcome of RV K is denoted as k_i. We use $\max(\cdot)$ to denote the maximization operator, and $\arg\max(\cdot)$ to denote the argument which yields the maximum, *e.g.*, if function $f(x)$ has a global maximum at $x = x_0$, then we have the following: $f(x_0) = \max_x f(x)$, and $x_0 = \arg\max_x f(x)$. The integer part of real number τ is denoted as $\lfloor \tau \rfloor$.

3.1 Introduction

In the previous section, simulation results were used to predict the performance of a SPAD-based VLC system. In this chapter, the performance a SPAD-based VLC system is studied analytically and experimentally. First, an ideal case is considered in which the noise intensity is perfectly known by a receiver; then a case when it is not known is analyzed. This is of practical relevance to VLC as the room illumination level in an indoor environment may suddenly change, when, for instance, ambient light is switched from on to off, or *vice versa*.

On-off keying (OOK) is a commonly used modulation scheme in optical communication. For high-speed communication systems, such as VLC, OOK is appealing as it is relatively simple to implement on hardware. However, a drawback of using OOK is that it requires a decision threshold, which in practice needs to be determined in a dynamic environment. A sudden change in the indoor illumination level can cause an imprecise estimation of the channel's noise. As a result, the threshold of OOK could be at a suboptimal value. This can cause the BER of a VLC system to increase, and may reduce the quality-of-service (QoS). For planning purposes, it is desirable to understand the impact of indoor illumination changes on performance.

A considerable amount of research has been published on communication over photon counting channels (see e.g. [73, 74, 75, 76, 77, 78, 79]). However, this chapter builds upon the following research work:

In [80], the authors studied the BER performance of OOK, when noise photon counts were known and signal photon counts were estimated from pilot symbols, from which the threshold of OOK was estimated. This thesis takes a different approach: the performance of OOK is studied in terms of capacity, photon-efficiency, and BER, when noise photon counts deviate from an assumed value. Once noise photon counts deviate from an assumed value, the decision threshold of OOK could be set to a suboptimal value, and thereby impair performance. Though pilot symbols can be used to estimate noise photon counts, there will be measurement uncertainties in practice. Therefore, the exact value of noise photon counts may not be perfectly known.

In [81], the capacity of OOK and M-ary pulse position modulation (M-PPM) were studied, in which the duty cycle of OOK was restricted. This thesis expands upon this work by considering hard-decision demodulation with no constraint on the duty cycle of OOK. Although hard-decision demodulation is suboptimal, it is an attractive scheme for high-speed communication systems, such as VLC, as it has a low complexity.

In [82], the performance of OOK and M-PPM were compared by considering an ideal channel, that is, a channel in which a receiver is limited by shot noise due to the Poisson statistics of photon arrivals. This thesis extents

this work by considering a non-ideal channel, where a receiver is subjected to shot noise, dark counts and background noise.

3.2 System Model

The transmitter sends photons, and receivers count the number of photons, k, which arrive according to a Poisson distribution. The probability that k photons are observed by the receiver when the intensity modulator is *off* is given by

$$P_{K|X}(k|0) = \frac{\lambda_n^k}{k!} e^{-\lambda_n}, \tag{3.1}$$

and when it is *on*

$$P_{K|X}(k|1) = \frac{(\lambda_s + \lambda_n)^k}{k!} e^{-(\lambda_s+\lambda_n)}, \quad \lambda_s, \lambda_n \in \mathbb{R}_0^+, \quad k \in \mathbb{N}, \tag{3.2}$$

where λ_s is the average number of signal photons per slot, and λ_n is the average number of noise photons per slot due to ambient noise and dark counts.

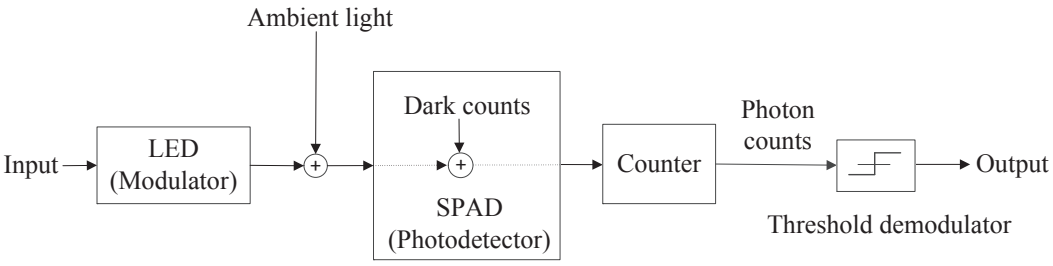

Figure 3.1: Block diagram of optical communication system with OOK.

For the OOK system, shown in Figure 3.1, let discrete RVs X, K, and $\hat{X}$ denote the system input, the number of photons detected, and the output of the demodulator, respectively. Here, X takes on values from the set $\mathcal{X} = \{0, 1\}$ with *a priori* probabilities $P_X(0)$ and $P_X(1)$.

At the receiver, a maximum *a posteriori* probability (MAP) demodulator is used to estimate the transmitted symbol; by which if k photons are observed, the input is estimated according to

$$\hat{x} = \arg\max_{x \in \mathcal{X}} P_{K|X}(k|x) P_X(x), \tag{3.3}$$

this produces an output alphabet $\hat{\mathcal{X}} = \{0, 1\}$ and the following crossover probabilities specified by the channel probability transition matrix

$$\mathbf{P} = \begin{pmatrix} P_{\hat{X}|X}(0|0) & P_{\hat{X}|X}(1|0) \\ P_{\hat{X}|X}(0|1) & P_{\hat{X}|X}(1|1) \end{pmatrix}. \tag{3.4}$$

For the M-PPM system, shown in Figure 3.2, let discrete RV U denote the system input, which is uniformly distributed over $\mathcal{U} = \{0, 1, \ldots, M-1\}$.

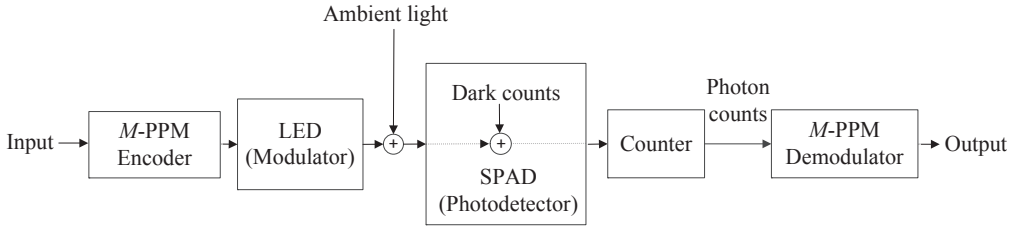

Figure 3.2: Block diagram of optical communication system with M-PPM.

Here, M is the PPM modulation order, which takes a value from the finite set $\mathcal{M} = \{2^n | \ n \leq m \ \text{ and } \ n, m \in \mathbb{N}^+\}$, and 2^m is the maximum modulation order of the system. The number of photons observed in a received M-PPM symbol can be written as

$$\mathbf{k} = (k_0, k_1, \ldots, k_{M-1}) \in \mathbb{N}^M, \tag{3.5}$$

where k_i is the number of photons detected in ith slot. The distribution of the number of photons in each slot is given by (3.1) if the observation is during a non-signal slot, otherwise the distribution is given by (3.2). The sequence of photon counts $\mathbf{k}$, (3.5), is then passed to a hard-decision demodulator, which estimates the transmitted symbol according to

$$\hat{u} = \arg \max_{i \in \ \mathcal{U}} k_i \ . \tag{3.6}$$

This hard-decision demodulator selects the slot with the most photon counts as the transmitted signal slot. In case of a tie, the demodulator randomly selects a slot among those with the most photon counts. If no photons arrive in an M-PPM symbol, *i.e.*, an erasure occurs, the demodulator randomly

chooses one of the M-PPM slots. Accordingly, the output RV $\hat{U}$ takes on values from the set $\hat{\mathcal{U}} = \{0, 1, \ldots, M-1\}$. This channel is an M-ary input M-ary output channel, which can be described by the following channel probability transition matrix

$$\mathbf{T} = \begin{pmatrix} P_{\hat{U}|U}(0|0) & P_{\hat{U}|U}(1|0) & \ldots & P_{\hat{U}|U}(M-1|0) \\ P_{\hat{U}|U}(0|1) & P_{\hat{U}|U}(1|1) & \ldots & P_{\hat{U}|U}(M-1|1) \\ \vdots & \vdots & \ddots & \vdots \\ P_{\hat{U}|U}(0|M-1) & P_{\hat{U}|U}(1|M-1) & \ldots & P_{\hat{U}|U}(M-1|M-1) \end{pmatrix}; \quad (3.7)$$

where, each row of $\mathbf{T}$ represents the conditional pmf of the output given a specific value of the input.

3.3 Analysis

3.3.1 Performance

Capacity: In this section, the capacity of a SPAD-based receiver with OOK and M-PPM signalling constraints is studied.

The MAP rule in (3.3) compares the weighted conditional probability $P_{K|X}(k|0)P_X(0)$ with $P_{K|X}(k|1)P_X(1)$ to make a binary decision. Treating k as continuous, the argument τ of the OOK threshold $\lfloor\tau\rfloor$ is defined as the value of k at which

$$P_{K|X}(\tau|0)P_X(0) = P_{K|X}(\tau|1)P_X(1); \tag{3.8}$$

substituting (3.1) and (3.2) into (3.8), and taking the natural logarithm of both sides yields

$$\tau = \frac{\lambda_s + \ln\left(\frac{P_X(0)}{P_X(1)}\right)}{\ln\left(1+\frac{\lambda_s}{\lambda_n}\right)} \ . \tag{3.9}$$

Using (3.9), one can compute the transition probabilities of (3.4) as follows

$$P_{\hat{X}|X}(0|1) = \sum_{k=0}^{\lfloor\tau\rfloor} P_{K|X}(k|1), \tag{3.10}$$

$$P_{\hat{X}|X}(1|0) = \sum_{k=\lfloor\tau\rfloor+1}^{\infty} P_{K|X}(k|0), \tag{3.11}$$

$$P_{\hat{X}|X}(0|0) = 1 - P_{\hat{X}|X}(1|0), \tag{3.12}$$

$$P_{\hat{X}|X}(1|1) = 1 - P_{\hat{X}|X}(0|1); \tag{3.13}$$

from which we can obtain the marginal distribution

$$P_{\hat{X}}(\hat{x}) = \sum_{x \in \mathcal{X}} P_{\hat{X}|X}(\hat{x}|x) P_X(x). \tag{3.14}$$

The capacity of the OOK system, C_o, is given by

$$C_o = \max_{P_X(x)} I(X; \hat{X}) \ \ \text{(bits/slot)}; \tag{3.15}$$

here $I(X; \hat{X})$ is the mutual information between RVs X and $\hat{X}$, which can be computed as follows

$$I(X; \hat{X}) = H(\hat{X}) - H(\hat{X}|X) \ \ \text{(bits/slot)}, \tag{3.16}$$

where $H(\hat{X})$ is the entropy of RV $\hat{X}$, and $H(\hat{X}|X)$ is the conditional entropy of $\hat{X}$ given X, and are given by

$$H(\hat{X}) = -\sum_{\hat{x} \in \hat{\mathcal{X}}} P_{\hat{X}}(\hat{x}) \log_2 P_{\hat{X}}(\hat{x}) \ \ \text{(bits/slot)}, \tag{3.17}$$

$$H(\hat{X}|X) = -\sum_{x \in \mathcal{X}} P_X(x) \sum_{\hat{x} \in \hat{\mathcal{X}}} P_{\hat{X}|X}(\hat{x}|x) \log_2 P_{\hat{X}|X}(\hat{x}|x) \ \ \text{(bits/slot)}; \tag{3.18}$$

substituting (3.17) and (3.18) into (3.16), yields

$$\begin{aligned} I(X; \hat{X}) = {} & H_b\{P_X(0) P_{\hat{X}|X}(0|0) + P_X(1) P_{\hat{X}|X}(0|1)\} \\ & - P_X(0) H_b\{P_{\hat{X}|X}(1|0)\} - P_X(1) H_b\{P_{\hat{X}|X}(0|1)\} \ \ \text{(bits/slot)}, \end{aligned} \tag{3.19}$$

where $H_b\{\cdot\}$ is the binary entropy function defined as

$$H_b\{p\} \triangleq -p\log_2 p - (1-p)\log_2(1-p).$$

Figure 3.3 shows numerical evaluations of the capacity of OOK, (3.15), and its mutual information, (3.19), for various values of λ_s. In the numerical results the value of the noise, λ_n, is set to 1.5. This value was measured experimentally (Section 3.4.3). The discontinuities in $I(X;\hat{X})$ are due to the step changes in the threshold as the threshold can only take discrete values. An example to illustrate this is shown in Figure 3.4. When λ_s increases $\lfloor\tau\rfloor$ shifts from one integer value to another, (3.9); these transitions give rise to the discontinuities in $I(X;\hat{X})$. In Figure 3.3, the capacity increases with λ_s, and occurs at various values of $P_X(1)$. The optimal input distribution, that is, the capacity-achieving input distribution, is given by

$$P_X^*(x) = \arg\max_{P_X(x)} I(X;\hat{X}). \tag{3.20}$$

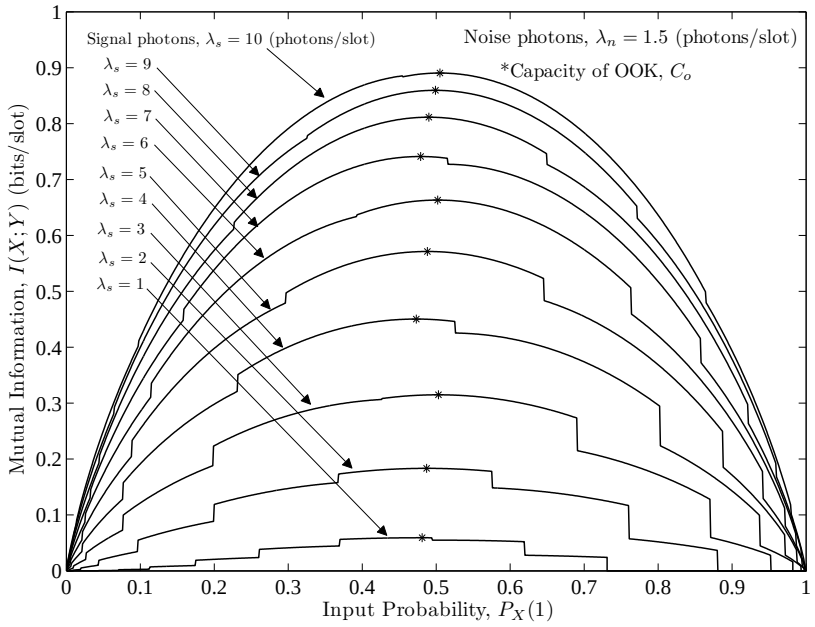

Figure 3.3: Mutual information versus input probability for OOK.

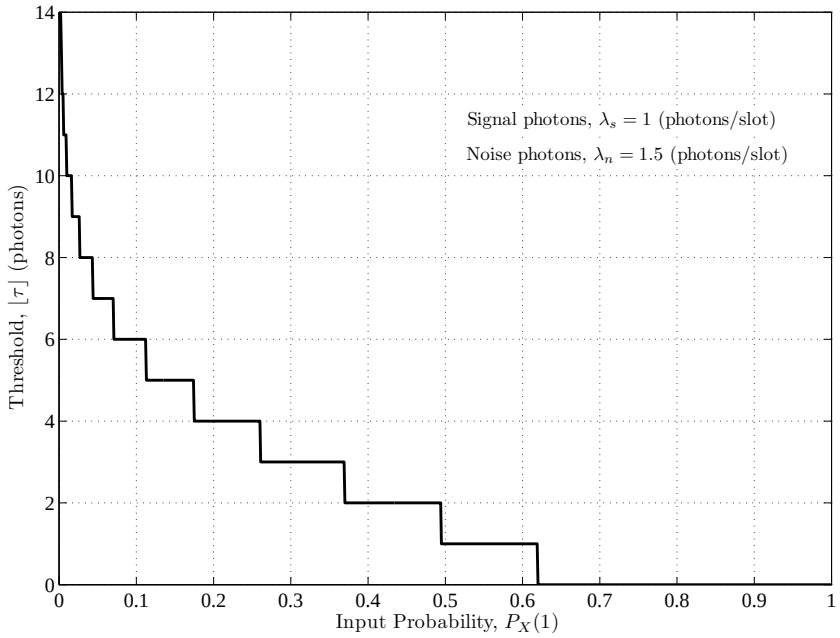

Figure 3.4: Threshold versus input probability.

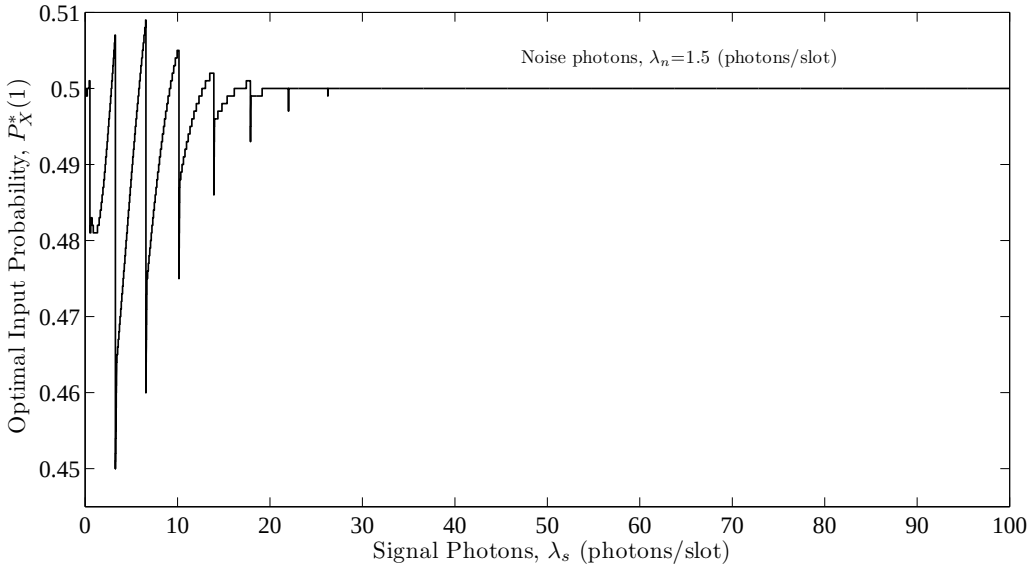

Figure 3.5: Optimal value of input probability for OOK versus number of signal photons per slot.

Figure 3.5 shows numerical results of the optimal input distribution, (3.20), as λ_s varies. Here, the value of λ_n is set to 1.5 as this value was measured experimentally (Section 3.4.3). In this plot, it can be seen that $P_X^*(1)$ fluctuates at low values of λ_s, since the channel is generally asymmetric, $P_{\hat{X}|X}(0|1) \neq P_{\hat{X}|X}(1|0)$. However, as λ_s increases the channel becomes less asymmetric, $P_{\hat{X}|X}(0|1) \approx P_{\hat{X}|X}(1|0)$, for which the capacity-achieving input distribution approaches a uniform distribution, $P_X^*(x) = \frac{1}{2}\ \forall x \in \mathcal{X}$.

An implication of using a hard-decision decoder in the photon-counting regime, (3.3), is that there exists a value of $P_X(1)$ denoted by ϵ, such that if $P_X(1) > \epsilon$ then $C_o = 0$ as $P_{\hat{X}}(1) = 1$; this occurs when

$$P_{K|X}(k|0)P_X(0) < P_{K|X}(k|1)P_X(1) \quad \forall k. \tag{3.21}$$

Letting $k = 0$ and solving for $P_X(1)$ in (3.21), yields the following condition under which $C_o = 0$

$$P_X(1) > \frac{1}{1 + e^{-\lambda_s}} \triangleq \epsilon, \tag{3.22}$$

or equivalently, by the law of total probability,

$$P_X(0) < 1 - \epsilon. \tag{3.23}$$

The transition probabilities of PPM, (3.7), can be computed as follows

$$P_{\hat{U}|U}(\hat{u}|u) = \begin{cases} 1 - P_s, & \text{if } \hat{u} = u \\ \dfrac{P_s}{M-1}, & \text{if } \hat{u} \neq u \end{cases}, \tag{3.24}$$

where P_s is the symbol-error probability[1], given by [68]

$$P_s = 1 - \sum_{k=0}^{\infty} \frac{P_{K|X}(k|1)}{P_{K|X}(k|0)M} \left(F_{K|X}(k|0)^M - F_{K|X}(k-1|0)^M \right), \quad \lambda_n > 0, \tag{3.25}$$

[1]Numerical evaluation of (3.25) for small values of P_s could be difficult as computers represent numbers with a finite precision. For example, a computer running MATLAB® would evaluate $1 - (1 - 10^{-30})$ as zero. See [83, 84] for methods to overcome this issue.

and here $F_{K|X}(k|0)$ is the cumulative-mass function of (3.1)

$$F_{K|X}(k|0) = \sum_{i=0}^{k} \frac{\lambda_n^i e^{-\lambda_n}}{i!}.$$

Referring to (3.7) and noting (3.24), this channel is symmetric as all rows of the channel probability transition matrix $\mathbf{T}$ are permutations of one another, and likewise for the columns. The capacity of this M-ary symmetric channel is achieved by a uniform distribution on the input alphabet [85], $P_U(u) = \frac{1}{M} \ \forall u \in \mathcal{U}$, and is given by [86, 87]

$$C_p = \frac{1}{M}\left(\log_2 M + (1-P_s)\log_2(1-P_s) + P_s \log_2\left(\frac{P_s}{M-1}\right)\right) \quad \text{(bits/slot)}. \tag{3.26}$$

Figure 3.6 shows some numerical evaluations of (3.15) and (3.26). In these numerical results, the value of λ_n is set to 1.5 as this value was measured experimentally (Section 3.4.3). The average number of received photons is $\bar{\mu} = \lambda_s P_X^*(1)$ for OOK and $\bar{\mu} = \frac{\lambda_s}{M}$ for PPM. At low values of $\bar{\mu}$ the capacities, C_o and C_p, increase with $\bar{\mu}$. At high values of $\bar{\mu}$, the capacity of OOK and PPM saturate, and OOK has an improved performance over PPM due to the following reasons: at high values of $\bar{\mu}$ the error probabilities of OOK become $P_{Y|X}(1|0) \approx 0$ and $P_{Y|X}(0|1) \approx 0$, and from (3.15) and (3.19) the capacity of OOK can be approximated as $C_o \approx 1$. However, at high values of $\bar{\mu}$ the symbol-error probability of PPM $P_s \approx 0$, and (3.26) can be approximated as $C_p \approx \frac{\log_2 M}{M} \leq \frac{1}{2}$.

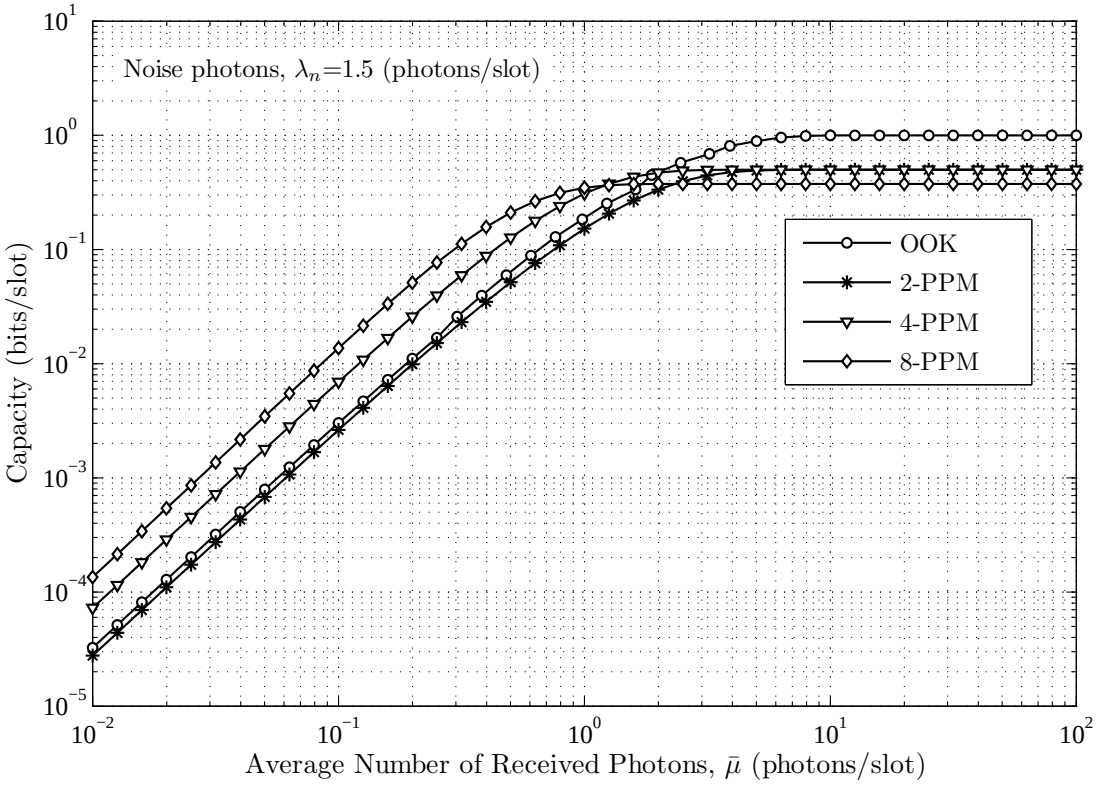

Figure 3.6: Capacity of OOK and PPM versus average number of received photons. Here, $\bar{\mu} = \lambda_s P_X^*(1)$ for OOK, and $\bar{\mu} = \dfrac{\lambda_s}{M}$ for PPM.

Photon-Efficiency: For OOK the photon-efficiency is given by

$$\rho_o = \frac{C_o}{\bar{\mu}} \text{ (bits/photon)}, \tag{3.27}$$

and for PPM it is given by

$$\rho_p = \frac{C_p}{\bar{\mu}} \text{ (bits/photon)}. \tag{3.28}$$

Figure 3.7 shows some numerical evaluations of (3.27) and (3.28). Here, the value of λ_n is set to 1.5 as this value was measured experimentally (Section 3.4.3). At low values of $\bar{\mu}$ the capacity of OOK and PPM improves with $\bar{\mu}$, but simultaneously the average number of received photons per slot increases. The overall effect is an increase in ρ_o and ρ_p with $\bar{\mu}$. However, at high values of $\bar{\mu}$ the capacity of OOK and PPM become approximately constant, $C_o \approx 1$ and $C_p \approx \frac{\log_2 M}{M}$. As a result, from (3.27) and (3.28), OOK has an improved performance over PPM since its photon-efficiency decreases as $\frac{1}{\bar{\mu}}$, whereas the photon-efficiency of PPM decreases as $\frac{\log_2 M}{M\bar{\mu}} \leq \frac{1}{2\bar{\mu}}$.

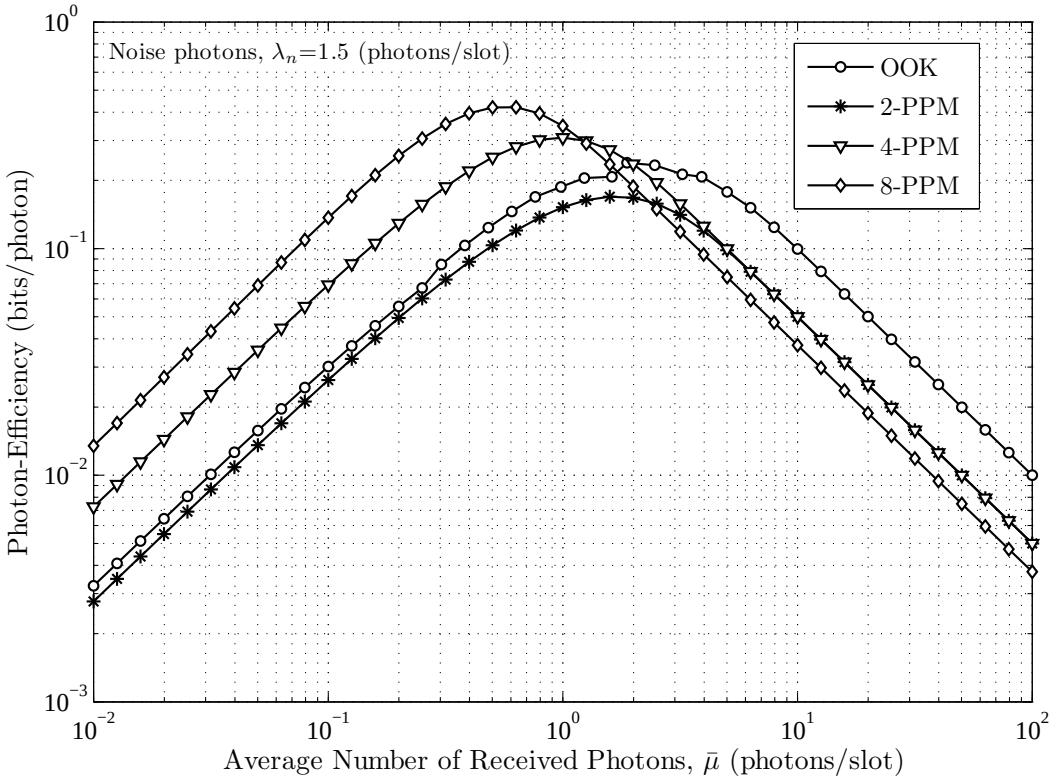

Figure 3.7: Photon-efficiency of OOK and PPM versus average number of received photons.

Bit-Error Probability

For OOK the BEP can be expressed as

$$P_o = \sum_{\hat{x}\in\hat{\mathcal{X}}} \sum_{\substack{x\in\mathcal{X} \\ x\neq\hat{x}}} P_{\hat{X}|X}(\hat{x}|x) P_X(x); \tag{3.29}$$

using (3.10) and (3.11), the preceding can be explicitly written as

$$P_o = P_X(0) \sum_{k=\lfloor\tau\rfloor+1}^{\infty} P_{K|X}(k|0) + P_X(1) \sum_{k=0}^{\lfloor\tau\rfloor} P_{K|X}(k|1), \tag{3.30}$$

and the BEP of PPM is given by [68]

$$P_p = \frac{M}{2(M-1)} P_s. \tag{3.31}$$

Figure 3.8 shows the BEP performance of OOK and PPM. The value of λ_n here is set to 1.5 as this value was measured in our experiment. PPM has an improved performance over OOK; however, the trade-off made for this improvement is an increase in the signal photons, λ_s, by a factor of $\frac{M}{2}$.

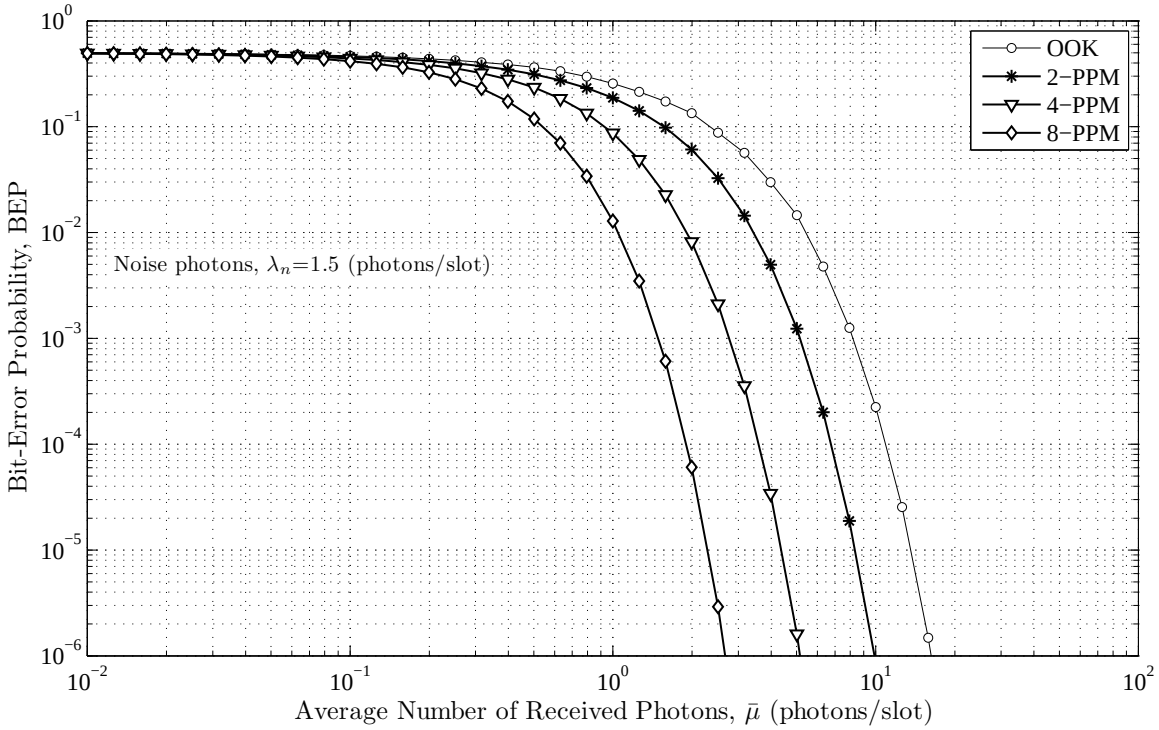

Figure 3.8: Bit-error probability of OOK and PPM on a Poisson channel. All modulation symbols are equiprobable.

3.3.2 Impact of Noise Deviation on Performance

Here, the performance of OOK and PPM is investigated, when the noise intensity deviates from an assumed value. Let λ_σ be the assumed value of the noise, by which the threshold of OOK and modulation order of PPM are set according to

$$\lfloor \tilde{\tau} \rfloor = \left\lfloor \frac{\lambda_s + \ln\left(\frac{P_X(0)}{P_X(1)}\right)}{\ln\left(1+\frac{\lambda_s}{\lambda_\sigma}\right)} \right\rfloor, \tag{3.32}$$

and

$$\tilde{M} = \arg\max_{M \in \mathcal{M}} C_p(M, \lambda_s, \lambda_\sigma), \tag{3.33}$$

respectively. The threshold, (3.32), is obtained by substituting λ_σ in lieu of λ_n in (3.9). The modulation order search in (3.33) is performed by replacing λ_n in (3.26) with λ_σ, setting $\lambda_s = M\bar{\mu}$, and varying the value of M. The value of M, denoted by $\tilde{M}$, that maximizes C_p is selected as the PPM modulation order.

OOK with Noise Deviation

The BEP of OOK in this setting can be obtained by replacing $\lfloor \tau \rfloor$ in (3.30) by $\lfloor \tilde{\tau} \rfloor$, (3.32); this yields

$$\tilde{P}_o = P_X(0) \sum_{k=\lfloor \tilde{\tau} \rfloor + 1}^{\infty} P_{K|X}(k|0) + P_X(1) \sum_{k=0}^{\lfloor \tilde{\tau} \rfloor} P_{K|X}(k|1). \tag{3.34}$$

In the following, $P_X^*(x)$ is obtained by substituting λ_σ in lieu of λ_n in (3.20).

Accordingly, (3.32) becomes

$$\lfloor \tilde{\tau} \rfloor = \left\lfloor \frac{\lambda_s + \ln\left(\frac{P_X^*(0)}{P_X^*(1)}\right)}{\ln\left(1+\frac{\lambda_s}{\lambda_\sigma}\right)} \right\rfloor ; \tag{3.35}$$

using the above one can compute the transition probabilities of OOK as follows

$$\begin{aligned}
\tilde{P}_{\hat{X}|X}(0|1) &= \sum_{k=0}^{\lfloor \tilde{\tau} \rfloor} P_{K|X}(k|1), && (3.36)\\
\tilde{P}_{\hat{X}|X}(1|0) &= \sum_{k=\lfloor \tilde{\tau} \rfloor+1}^{\infty} P_{K|X}(k|0), && (3.37)\\
\tilde{P}_{\hat{X}|X}(0|0) &= 1 - \tilde{P}_{\hat{X}|X}(1|0), && (3.38)\\
\tilde{P}_{\hat{X}|X}(1|1) &= 1 - \tilde{P}_{\hat{X}|X}(0|1), && (3.39)
\end{aligned}$$

Referring to (3.19) and using (3.36)-(3.39), we get the information rate of OOK

$$\begin{aligned}
\tilde{I}(X;\hat{X}) = {} & H_b\{P_X^*(0)\tilde{P}_{\hat{X}|X}(0|0) + P_X^*(1)\tilde{P}_{\hat{X}|X}(0|1)\} \\
& - P_X^*(0)H_b\{\tilde{P}_{\hat{X}|X}(1|0)\} - P_X^*(1)H_b\{\tilde{P}_{\hat{X}|X}(0|1)\} \quad \text{(bits/slot)}. \quad (3.40)
\end{aligned}$$

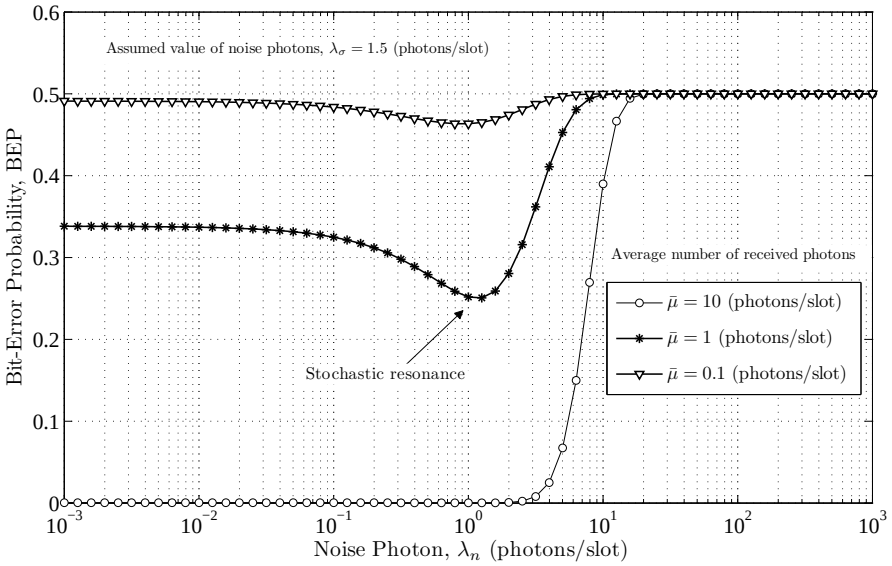

Figure 3.9: Bit-error probability of OOK when noise deviates from an assumed value ($\lambda_\sigma = 1.5$). Here, stochastic resonance is most apparent when $\bar{\mu} = 1$. All modulation symbols are equiprobable.

From (3.40) we can obtain the photon-efficiency

$$\tilde{\rho_o} = \frac{\tilde{I}(X;\hat{X})}{\bar{\mu}} \quad \text{(bits/photon)}. \tag{3.41}$$

Figures 3.9, 3.10, and 3.11 show numerical evaluations of (3.34), (3.40), and (3.41), respectively. In these numerical results the value of λ_n is set to 1.5 as this value was measured experimentally (Section 3.4.3). The higher the value of $\bar{\mu}$ the better the performance of the system is in terms of BEP and information rate. However, this is not necessarily the case for the photon-efficiency (Figure 3.11). For example, at low values of λ_n the system has a higher photon-efficiency when $\bar{\mu} = 1$ than when $\bar{\mu} = 10$. This is because at high values of $\bar{\mu}$, $\tilde{I}(X;\hat{X})$ saturates, and the photon-efficiency, (3.41), decreases as $\frac{1}{\bar{\mu}}$.

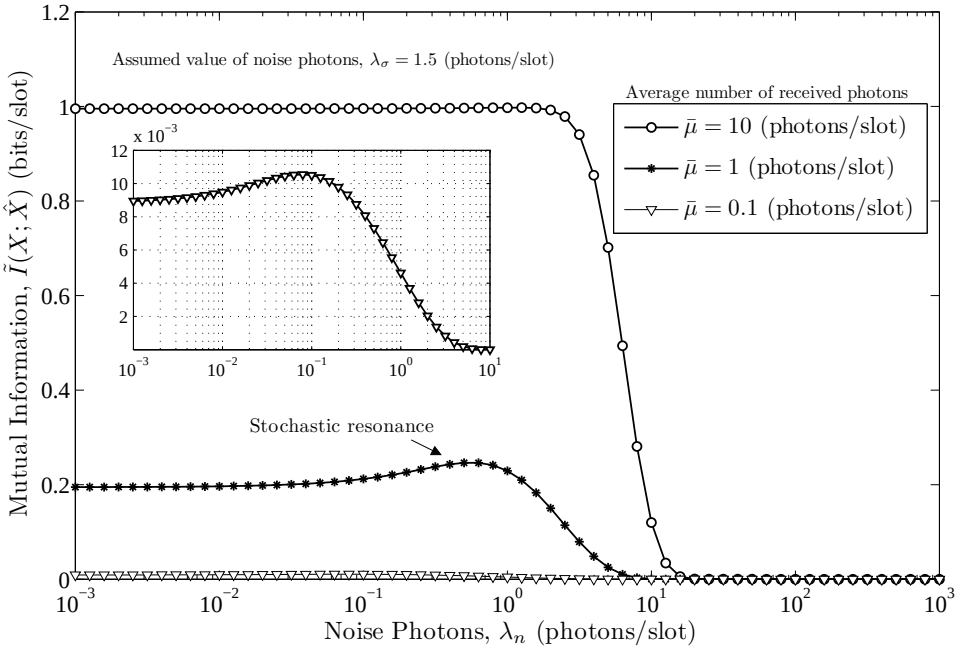

Figure 3.10: Mutual information of OOK when noise deviates from an assumed value ($\lambda_\sigma = 1.5$). Here, stochastic resonance is most apparent when $\bar{\mu} = 1$.

Additionally, there is an increase in $\tilde{I}(X;\hat{X})$ and $\tilde{\rho_o}$, and decrease in $\tilde{P}_o$ as λ_n increase. That is to say, the performance of the system temporarily improves with noise. The intuitive explanation for this is the following: when the actual value of the noise, λ_n, approaches its assumed value, λ_σ, less errors occur as the threshold approaches its optimal value (*i.e.*, $\lfloor\tilde{\tau}\rfloor \to \lfloor\tau\rfloor$ as $\lambda_n \to \lambda_\sigma$). As a result, system performance improves. This effect is known as *stochastic resonance* [88].

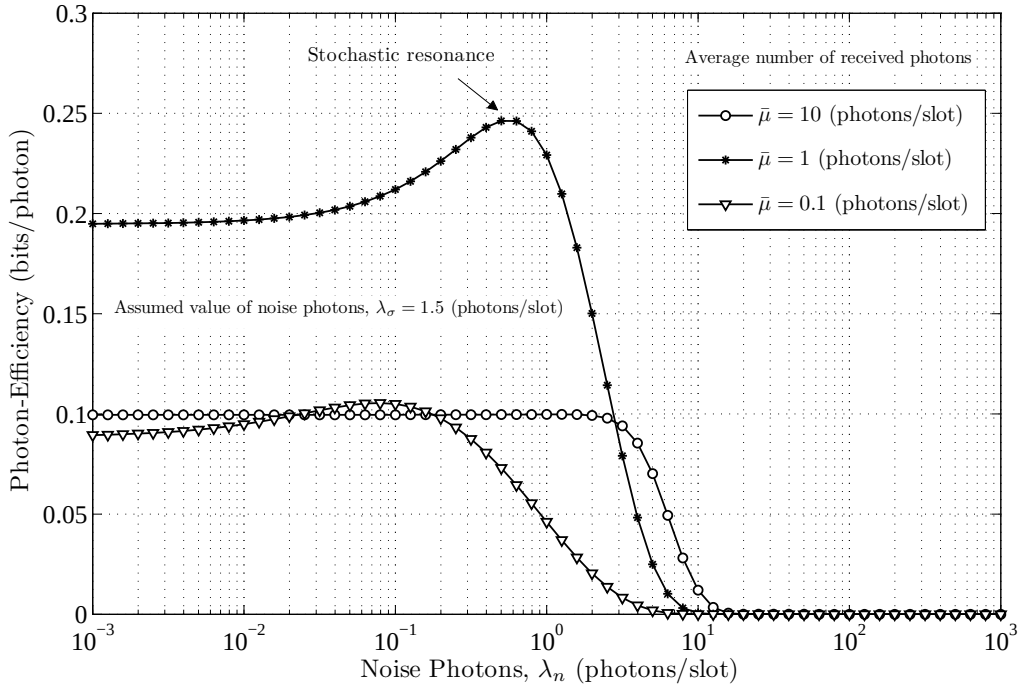

Figure 3.11: Photon-efficiency of OOK when noise deviates from an assumed value ($\lambda_\sigma = 1.5$). Here, stochastic resonance is most apparent when $\bar{\mu} = 1$.

PPM with Noise Deviation

Similar to (3.25); using (3.33) the symbol-error probability of PPM in this setting is

$$\tilde{P}_s = 1 - \sum_{k=0}^{\infty} \frac{P_{K|X}(k|1)}{P_{K|X}(k|0)\tilde{M}} \left(F_{K|X}(k|0)^{\tilde{M}} - F_{K|X}(k-1|0)^{\tilde{M}} \right), \quad \lambda_n > 0. \tag{3.42}$$

Using (3.42) with (3.33) and noting (3.31) one can obtain the BEP of PPM

$$\tilde{P}_p = \frac{\tilde{M}}{2(\tilde{M}-1)} \tilde{P}_s. \tag{3.43}$$

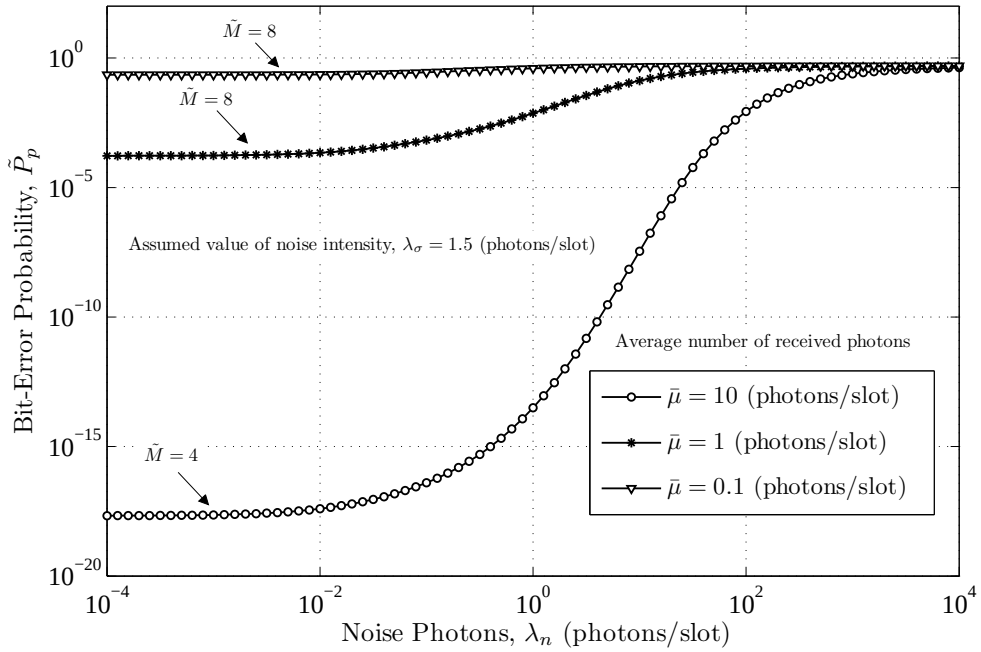

Figure 3.12: Bit-error probability of PPM versus noise on a Poisson channel. The PPM modulation order, $\tilde{M}$, is chosen by using (3.33). All modulation symbols are equiprobable.

The capacity of PPM here can be obtained by substituting (3.33) and (3.42) into (3.26); this yields

$$\tilde{C}_p = \frac{1}{\tilde{M}} \left(\log_2 \tilde{M} + (1 - \tilde{P}_s) \log_2 (1 - \tilde{P}_s) + \tilde{P}_s \log_2 \left(\frac{\tilde{P}_s}{\tilde{M} - 1} \right) \right) \quad \text{(bits/slot)}. \tag{3.44}$$

From the above one can obtain the photon-efficiency of PPM

$$\tilde{\rho}_p = \frac{\tilde{C}_p}{\bar{\mu}} \quad \text{(bits/photon)}. \tag{3.45}$$

Figures 3.12, 3.13, and 3.14 show numerical evaluations of (3.43), (3.44), and (3.45), respectively. Here, the value of λ_σ is set to 1.5 as this value was

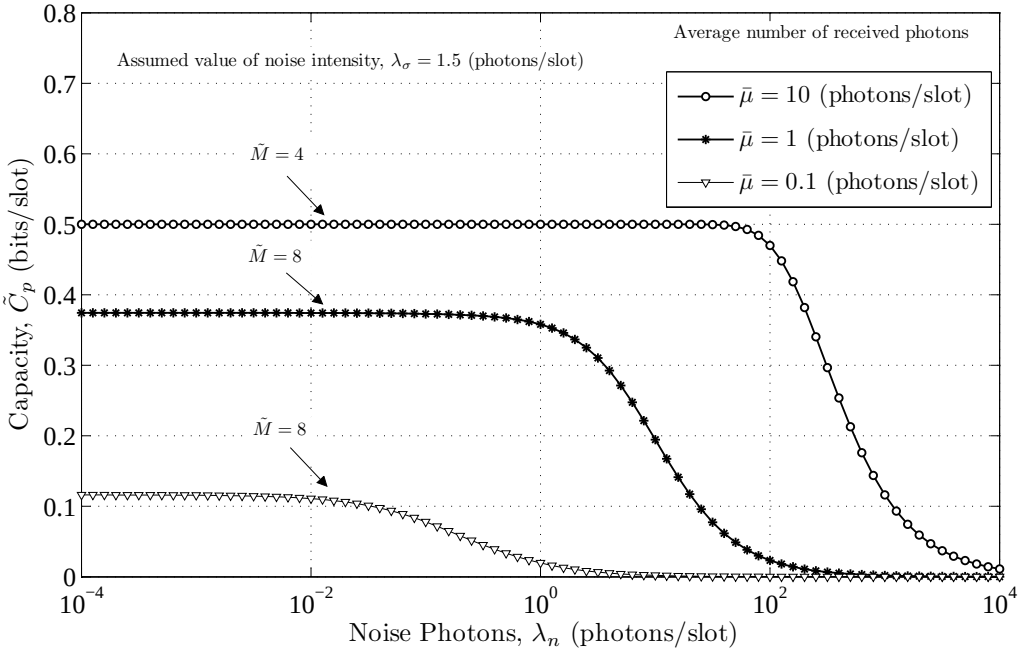

Figure 3.13: Capacity of PPM versus noise. The PPM modulation order, $\tilde{M}$, is chosen by using (3.33).

measured in our experiment. In our numerical results the modulation order of PPM, $\tilde{M}$, was set according to (3.33), which yields $\tilde{M} = 8$ for $\bar{\mu} = 0.1, \text{and } 1$. For $\bar{\mu} = 10$, (3.33) yields $\tilde{M} = 4$. $\tilde{M} = 2$ was not chosen as it achieved the least capacity.

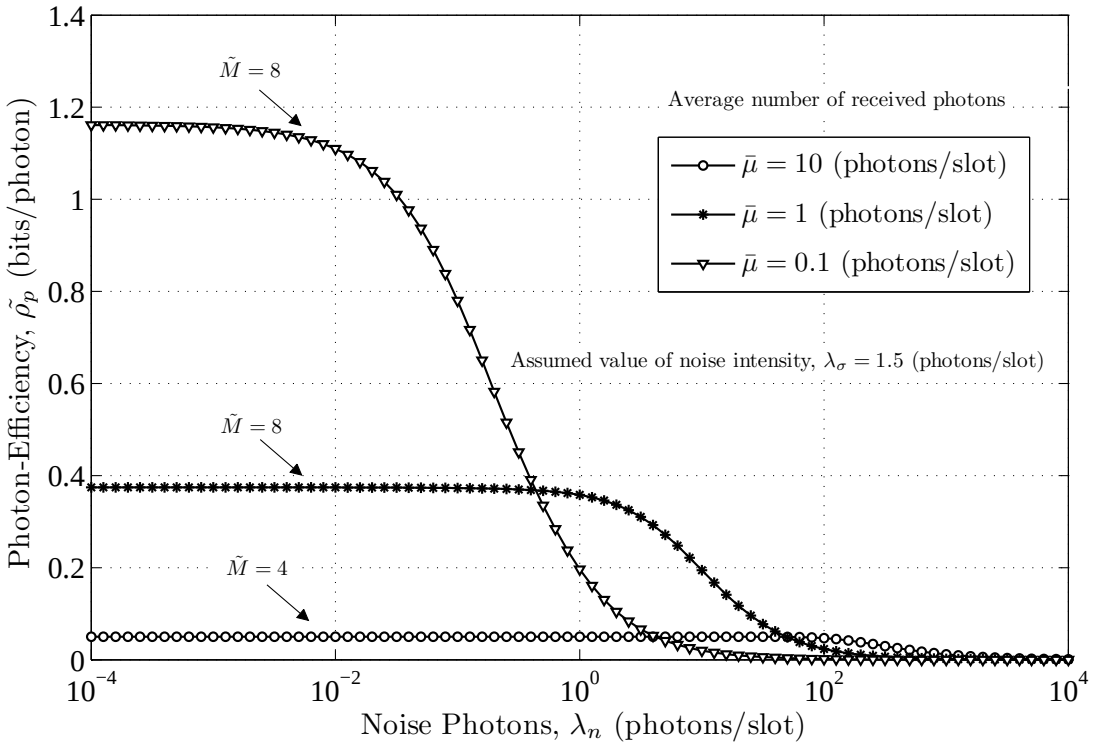

Figure 3.14: Photon-efficiency of PPM versus noise. The PPM modulation order, $\tilde{M}$, is chosen by using (3.33).

Relative Performance

Absolute quantities such as capacity, photon-efficiency, and BEP, can be used to assess the performance of modulation schemes. However, the gain of using a modulation scheme over another when the noise deviates can be revealed by considering the relative information rate, given by

$$\Lambda = \frac{\tilde{I}(X;\hat{X})}{\tilde{C}_p}, \tag{3.46}$$

and the relative BEP

$$\Gamma = \frac{\tilde{P}_o}{\tilde{P}_p}; \tag{3.47}$$

in the above equations we have used (3.34), (3.40), (3.43), and (3.44). As the noise decreases Λ and Γ approach a constant value

$$\Theta \triangleq \lim_{\lambda_n \to 0^+} \Lambda = \frac{\tilde{M}\left(H_b\{P_X^*(1)(1-\tilde{P}_{Y|X}(0|1))\} - P_X^*(1)H_b\{\tilde{P}_{Y|X}(0|1)\}\right)}{\log_2 \tilde{M} - H_b\{\frac{\tilde{M}-1}{\tilde{M}}e^{-\lambda_s}\} - \frac{\tilde{M}-1}{\tilde{M}}e^{-\lambda_s}\log_2(\tilde{M}-1)}, \tag{3.48}$$

and

$$\Phi \triangleq \lim_{\lambda_n \to 0^+} \Gamma = 2P_X(1)\sum_{k=0}^{\lfloor \tilde{\tau} \rfloor} \frac{\lambda_s^k}{k!}. \tag{3.49}$$

Here, Θ and Φ represent the maximum gain (or loss) of OOK over M-PPM at low noise intensities. Figure 3.15 shows some numerical results of (3.46). PPM yields a higher gain than OOK in terms of information rate. However, at low values of λ_n, OOK has a higher gain than PPM when $\bar{\mu} = 10$. Since

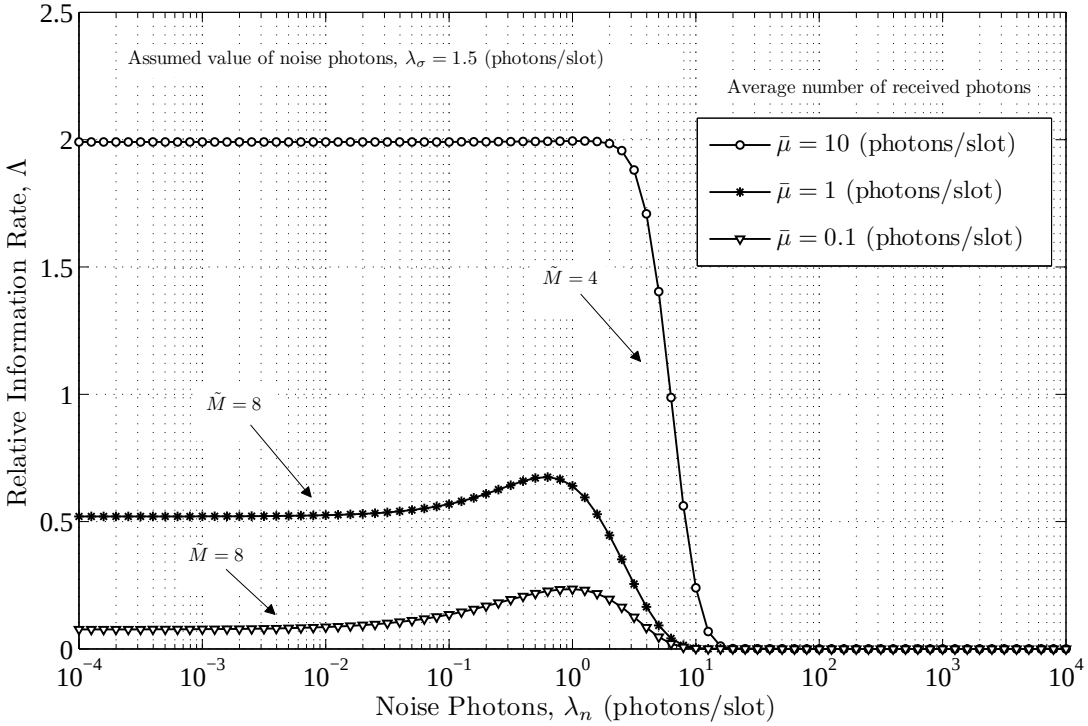

Figure 3.15: Relative information rate of OOK to PPM as noise deviates from an assumed value. The PPM modulation order, $\tilde{M}$, is chosen by using (3.33).

the loss due to the threshold being at a suboptimal value, $\lfloor \tilde{\tau} \rfloor$, is compensated by the high value of $\bar{\mu}$.

Figure 3.16 shows some numerical results of (3.47). PPM has a higher BEP gain than OOK. This is due to the following reasons: a) for a given value of $\bar{\mu}$, PPM has a higher number of *photons/slot* than OOK; explicitly, by a factor of $\frac{M}{2}\lambda_s$ b) the threshold of OOK is fixed at $\lfloor \tilde{\tau} \rfloor$, which causes the BER of OOK to increase when noise deviates.

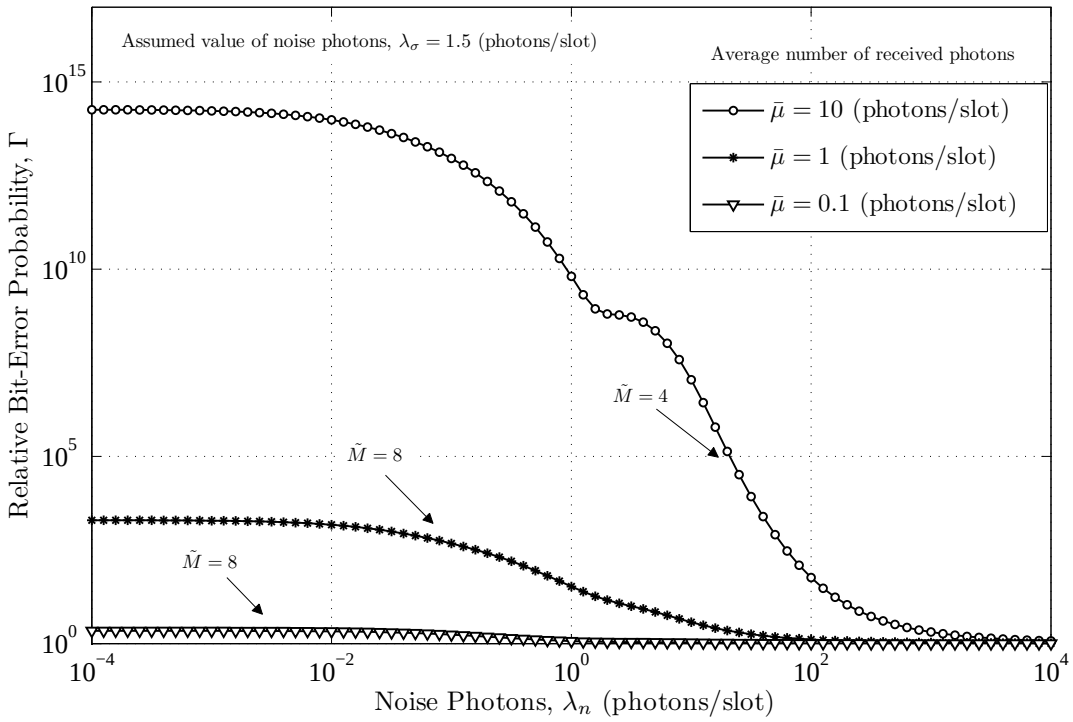

Figure 3.16: Relative Bit-Error Probability of OOK to PPM as noise deviates from an assumed value. The PPM modulation order, $\tilde{M}$, is chosen by using (3.33).

3.4 Experiment

The aim of this section is to experimentally investigate the performance of OOK and PPM, when noise deviates. Two main experiments are conducted:

- Case I: this experiment investigates the performance of OOK and PPM, when room illumination increases.
- Case II: this experiment investigates the performance of OOK and PPM, when room illumination decreases.

Before these two main experiments were conducted, an initial experiment was carried out to determine the threshold of OOK. An example to show how the threshold is obtained is provided in Section 3.4.2. This was followed by an initial run of the experiment to attain a BER of 10^{-3}. Figure 3.17 and Figure 3.18 shows the experimental apparatus.

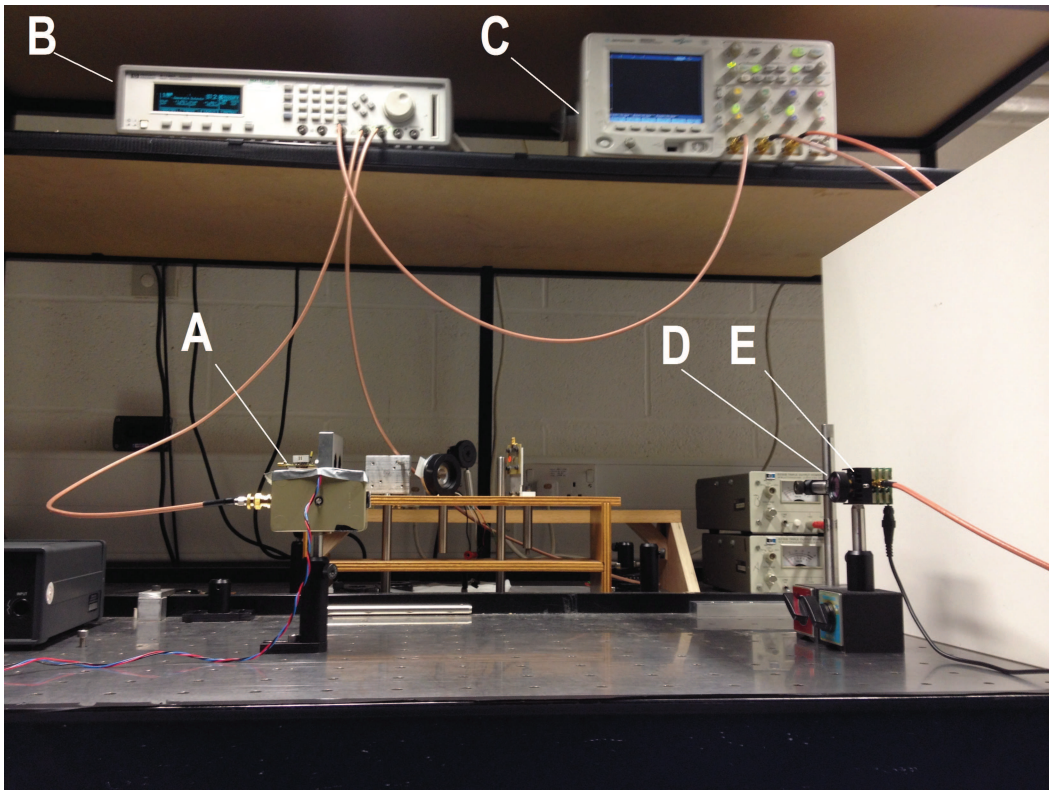

Figure 3.17: Apparatus: (A)Transmitter (*in-house built*), (B) Pulse generator (*HP B1130A*), (C) Oscilloscope (*Agilent MSO6104A*), (D) Interference filter (*Thorlabs FB650-40*), (E) SPAD (*SensL PCDMini0020*).

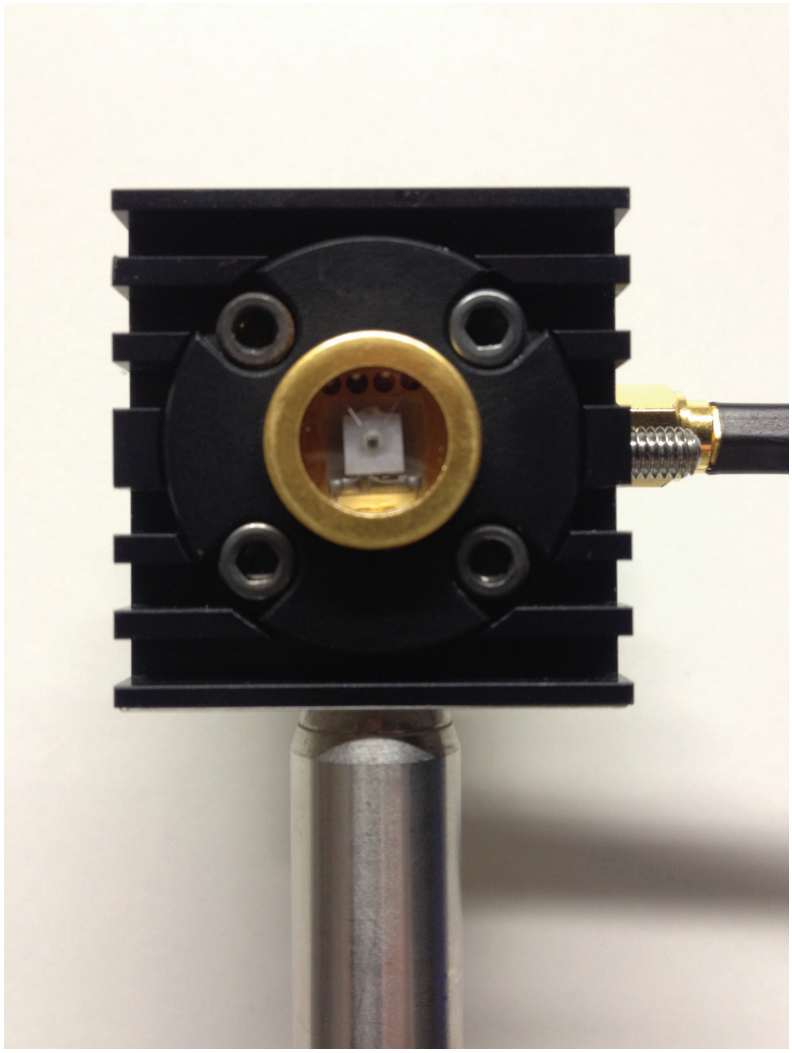

Figure 3.18: SPAD (*SensL PCDMini0020*).

3.4.1 Experimental Apparatus and Methods

Figure 3.19 shows block diagrams of the experimental setup. The apparatus consists of a PC, a pulse generator, an LED, a SPAD, and an oscilloscope.

The pulse generator drives an LED that illuminates a SPAD at the receiver. An interference filter placed in front of the SPAD is used to reduce noise photons caused by ambient light. Specifications of the filter with a summary of the experimental parameters are listed in Table 3.4. Once a photon is detected by a SPAD a pulse, called a photon-pulse, is generated and subsequently captured by an oscilloscope. Figure 3.20 shows an input signal to the LED and the output photon-pulses captured by the oscilloscope. The output of the oscilloscope is fed to a photon counter that is implemented on a PC.

In the experiment, input bits for the OOK and PPM system were randomly generated offline by a PC. For OOK, input bits were directly fed to a pulse generator, whereas for PPM an encoder that is implemented on a PC is used to map input bits into an M-PPM codeword (Table 3.1, Table 3.2, and Table 3.3 provide examples). PPM codewords were then passed to a pulse generator. The output of the photon counter is passed onto an OOK or M-PPM demodulator. Both demodulators are implemented on a PC. Flowcharts of software used in the experiments are presented in Appendix A.

The experiment was carried out in a room illuminated by white fluorescent light (~ 50 lux). The arrival-time of a photon is determined by the rising edge of a photon-pulse, which is depicted in Figure 3.20(b). In the experiment, an optical power-meter was used to estimate the intensity falling on a SPAD.

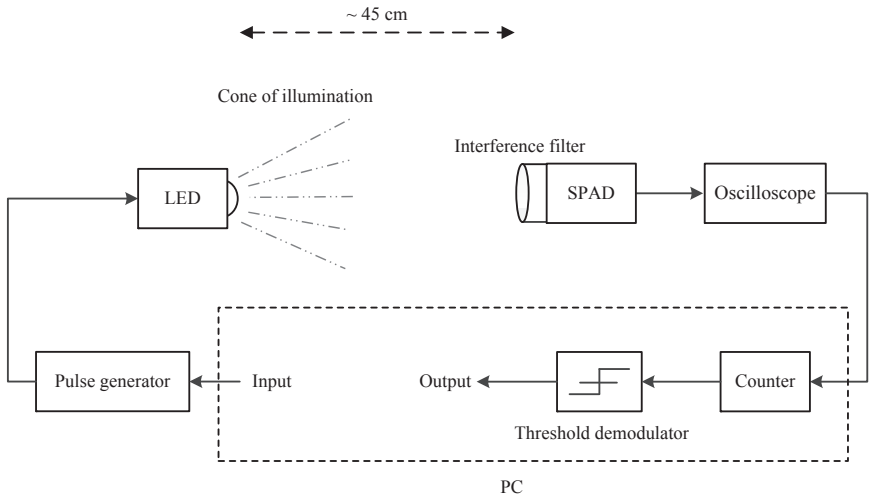

(a)

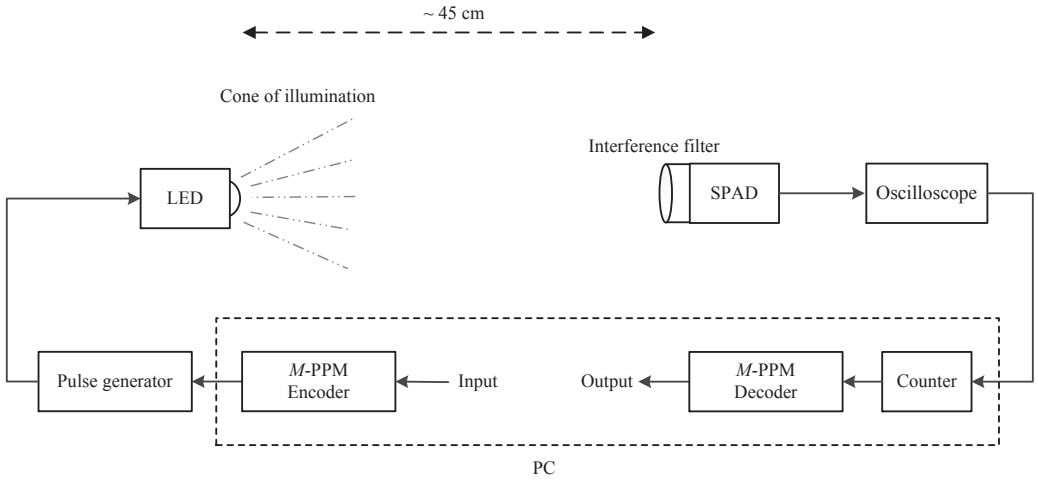

(b)

Figure 3.19: Block diagrams of experimental setup. (a) OOK, (b) PPM.

Table 3.1: Codebook for 2-PPM

Bits	Codeword
0	10
1	01

Table 3.2: Codebook for 4-PPM

Bits	Codeword
00	1000
01	0100
10	0010
11	0001

Table 3.3: Codebook for 8-PPM

Bits	Codeword
000	10000000
001	01000000
010	00100000
011	00010000
100	00001000
101	00000100
110	00000010
111	00000001

Table 3.4: Experimental parameters

Parameter	Value
Centre wavelength of LED	~ 640 nm
Slot duration	2 μsec
Centre wavelength of interference filter	~ 650 nm
FWHM[1] of interference filter	~ 40 nm
Transmittance of interference filter	$\sim 70\%$
Active area of SPAD	$\sim 3.14 \times 10^{-10}$ m^2
DCR[2]of SPAD	~ 130 Hz
Dead time of SPAD	~ 97 $n$sec
PDP[3]of SPAD at 640 nm	$\sim 14.5\%$

[1]Full width at half maximum. [2]Dark count rate.

[3]Photon-detection-probability.

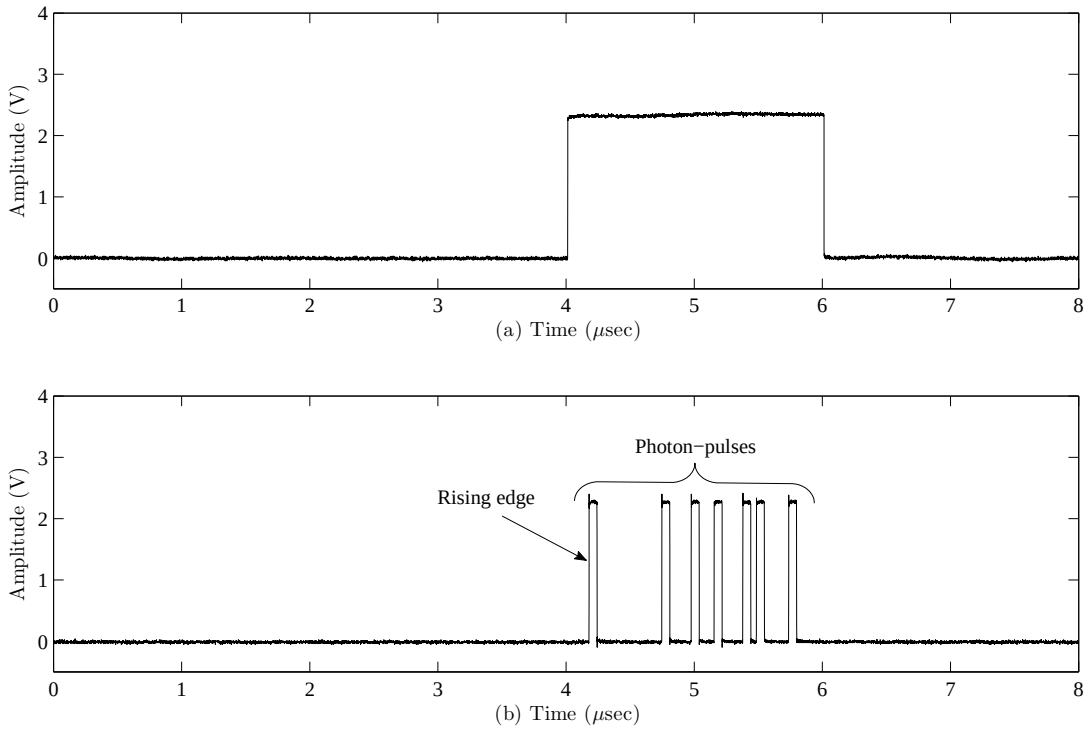

Figure 3.20: Signals recorded by the oscilloscope: (a) Input signal to LED, (b) Response of SPAD.

3.4.2 OOK Threshold Setting

The aim of this section is to illustrate how the threshold of OOK can be obtained experimentally. Figure 3.21 shows an example of histograms obtained by experiment. The histograms were obtained by sending 30,000 randomly generated bits; at this value the threshold of OOK was constant. The threshold of OOK was determined by the following method: the greatest number of photon counts for which the experimental histogram of transmitting binary *zero* is greater than that of binary *one*, was chosen as the threshold. This is illustrated in the inset of Figure 3.21.

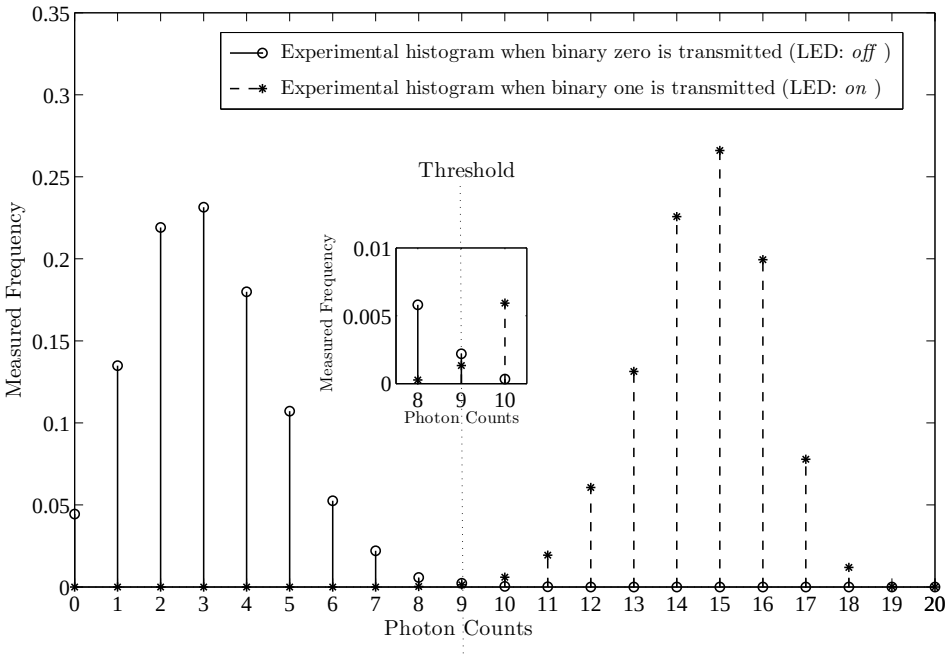

Figure 3.21: Threshold of OOK determined from experimental histograms. In the inset it can be seen that the greatest number of photon counts for which the histogram of transmitting binary *zero* is greater than that of binary *one* is at 9.

3.4.3 Experimental Results and Discussion

The aim of this section is to examine the performance of OOK and PPM when noise deviates. In the initial state, the threshold of OOK and modulation order of PPM are set. In the final state, room illumination is switched from off to on, or *vice versa*. After this transition, the performance of OOK and PPM are inspected.

Case I: Off to On

An initial run of the experiment was carried out to attain a BER of 10^{-3}. This was accomplished by varying the intensity of the LED light source until a BER of 10^{-3} was achieved. 3×10^4 bits were sent for OOK and PPM in the initial and final state.

In the initial state, the room illumination was off, the target BER was 10^{-3}, and λ_n was measured to be $\sim 2.6 \times 10^{-4}$ (photons/slot). In the final state, the room illumination was turned on. The room illumination incident on the optical filter was measured to be $\sim$ 50 lux. This illumination level corresponds to $\lambda_n \sim 1.5$ (photons/slot).

Table 3.5 summarizes the experimental results and compares it with theory. Histograms for this experiment are shown in Figure 3.22. The threshold of OOK was 3 in the initial state. This was obtained by the method described in Section 3.4.2.

Table 3.5: Case I

			Initial state: off		Final state: on	
	Power[1]	λ_s^*	BER*	BEP†	BER*	BEP†
OOK	~ 6.8	~ 12.8	$\sim 10^{-3}$	1.9×10^{-5}	$\sim 5.1 \times 10^{-2}$	2.2×10^{-1}
2-PPM	~ 4.5	~ 8.4	$\sim 10^{-3}$	1.1×10^{-4}	$\sim 1.0 \times 10^{-2}$	3.7×10^{-3}
4-PPM	~ 2.2	~ 8.2	$\sim 10^{-3}$	1.4×10^{-4}	$\sim 2.7 \times 10^{-2}$	7.1×10^{-3}
8-PPM	~ 1.1	~ 8.1	$\sim 10^{-3}$	1.5×10^{-4}	$\sim 4.2 \times 10^{-2}$	1.2×10^{-2}

[1]Power incident on the SPAD in pico-Watts. λ_s^* is the experimental average number of signal photons per slot. BER* is the experimental bit-error rate. BEP† is the bit-error probability (theoretical BER).

In Table 3.5, BEP is the bit-error probability (theoretical BER). BEP for OOK in the initial state is calculated from (3.30) with $\lambda_n = 2.6 \times 10^{-4}$, and $P_X(0) = P_X(1) = \frac{1}{2}$. In the final state, BEP is calculated from (3.34) with $\lambda_n = 1.5$, and $P_X(0) = P_X(1) = \frac{1}{2}$. For PPM, the BEP can be calculated from (3.31) or (3.43) with $\lambda_n = 2.6 \times 10^{-4}$ in the initial state, and $\lambda_n = 1.5$ in the final state.

The BER for OOK and PPM increased significantly, when the room illumination was turned on. This is due to the increase in λ_n. An additional factor that caused the BER of OOK to increase was that the threshold was at a suboptimal value, when the room illumination was turned on. This is illustrated in Figure 3.22(b). The optimal threshold in the final state is 5. However, when the room illumination was turned on λ_n increased, yet the threshold remained at its initial setting, 3. This suboptimal threshold, besides the increase in λ_n, caused the BER of OOK to rise. The reasons for discrepancies between theory and experiment will be discussed later in this section.

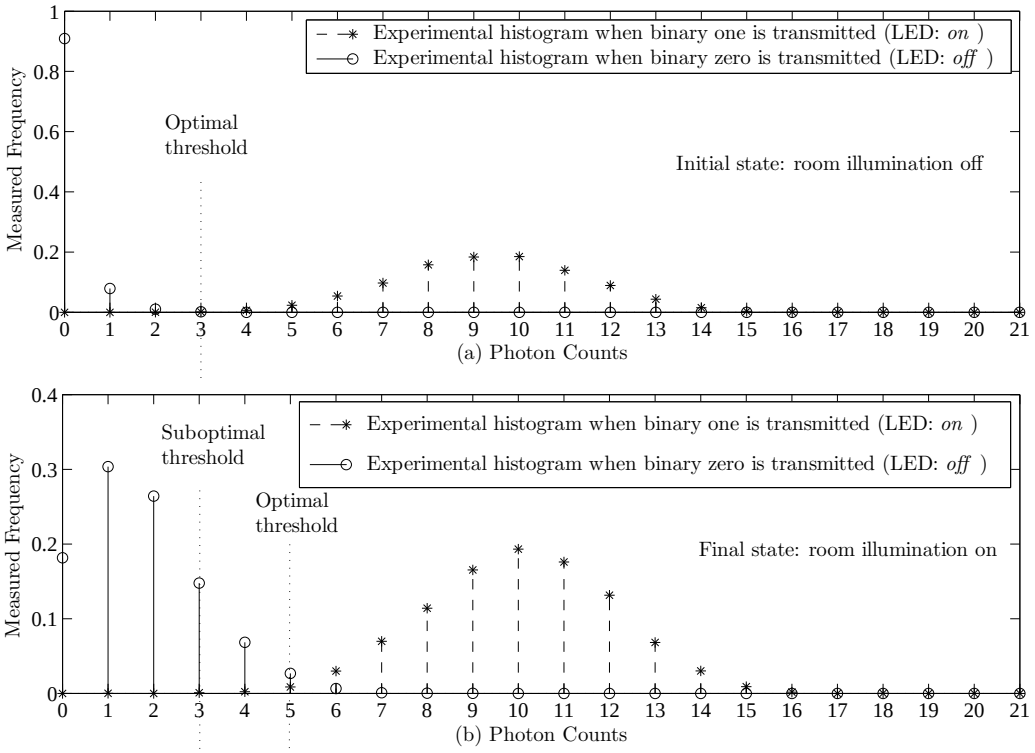

Figure 3.22: Experimental histograms of the photon counts (Case I). (a) In the initial state, the room illumination was off and the optimal threshold was 3. (b) In the final state, the room illumination was turned on. The experimental histograms changed in this state, and the threshold remained at its initial setting of 3. An optimal threshold in this state would be 5.

Case II: On to Off

An initial run of the experiment was carried out to attain a BER of 10^{-3}. This was accomplished by varying the intensity of the LED light source until a BER of 10^{-3} was achieved. For OOK, 3×10^4 bits were sent in the initial and final state. For PPM, 3×10^4 and 3×10^6 bits were sent in the initial and final state, respectively.

In the initial state, room illumination was on, and the target BER was 10^{-3}. The room illumination incident on the optical filter was ~ 50 lux, and λ_n was measured to be ~ 1.5 (photons/slot). In the final state, the room illumination was turned off.

Table 3.6 summarizes the experimental results and compares it with theory. Histograms for this experiment are shown in Figure 3.23. The threshold of OOK in the initial state was 7. This was obtained by the method described in Section 3.4.2.

In Table 3.6, BEP for OOK in the initial state is calculated from (3.30) with $\lambda_n = 1.5$, and $P_X(0) = P_X(1) = \frac{1}{2}$. In the final state, BEP is calculated from (3.34) with $\lambda_n = 2.6 \times 10^{-4}$, and $P_X(0) = P_X(1) = \frac{1}{2}$. For PPM, the BEP can be calculated from (3.31) or (3.43) with $\lambda_n = 1.5$ in the initial state, and $\lambda_n = 2.6 \times 10^{-4}$ in the final state.

The BER for OOK increased, when the room illumination was turned off. This is due to the threshold being at a suboptimal value. This is illustrated in Figure 3.23(b). In the final state, the optimal threshold is 4. However, when

Table 3.6: Case II

			Initial state: on		Final state: off	
	Power[1]	λ_s^*	BER*	BEP†	BER*	BEP†
OOK	~ 13.1	~ 24.4	$\sim 10^{-3}$	3.4×10^{-5}	$\sim 1.5 \times 10^{-2}$	5.7×10^{-5}
2-PPM	~ 7.3	~ 13.7	$\sim 10^{-3}$	9.2×10^{-5}	$\sim 6.3 \times 10^{-6}$	5.6×10^{-7}
4-PPM	~ 4.4	~ 16.4	$\sim 10^{-3}$	2.4×10^{-5}	$\sim 4.0 \times 10^{-6}$	3.8×10^{-8}
8-PPM	~ 2.3	~ 17.3	$\sim 10^{-3}$	2.3×10^{-5}	$\sim 5.3 \times 10^{-6}$	1.6×10^{-8}

[1]Power incident on the SPAD in pico-Watts. λ_s^* is the experimental average number of signal photons per slot. BER* is the experimental bit-error rate. BEP† is the bit-error probability (theoretical BER).

the room illumination was turned off, the threshold remained at its initial setting, 7. This caused the BER of OOK to increase. The BER of PPM improved, when the room was illumination was turned off as λ_n decreased.

Theory and experiment do not agree. However, they show similar trends. The reason for the discrepancy between them is the following: the mathematical models in Section 3.3 do not fully reflect the behaviour of a SPAD. In practice, SPADs have dead times. Figure 3.24 provides an illustration to show the effect of dead time on the detection of photons. The dead time limits the number of photons that can be detected, and propagates into subsequent time slots. These factors are not captured by the theoretical predictions. This causes a discrepancy between theory and experiment.

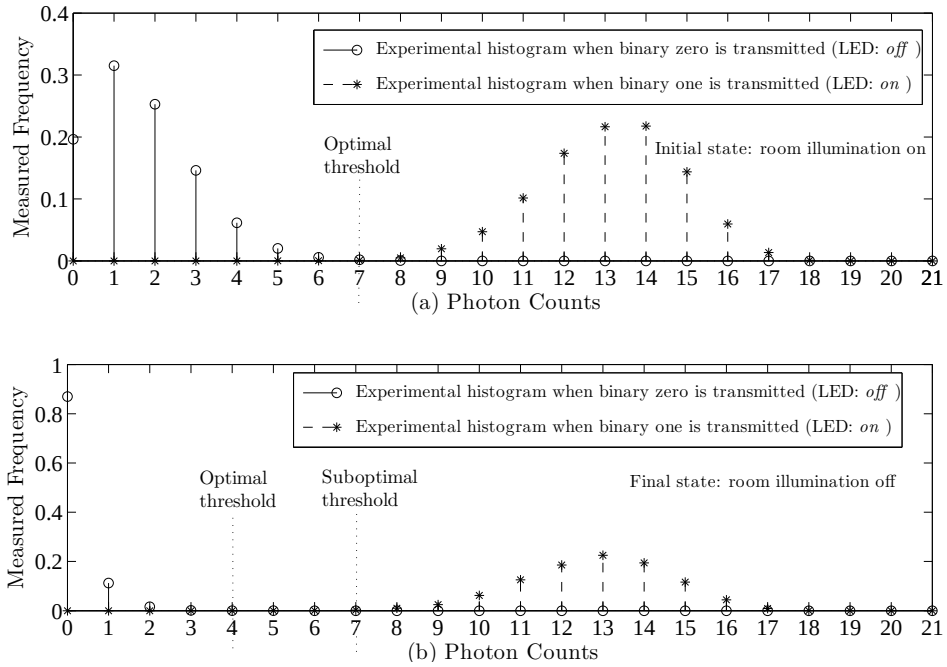

Figure 3.23: Experimental histograms of the photon counts (Case II). (a) In the initial state, the room illumination was on and the optimal threshold was 7. (b) In the final state, the room illumination was turned off. In this state, the experimental histograms changed, and the threshold remained at its initial setting of 7. An optimal threshold in this state would be 4.

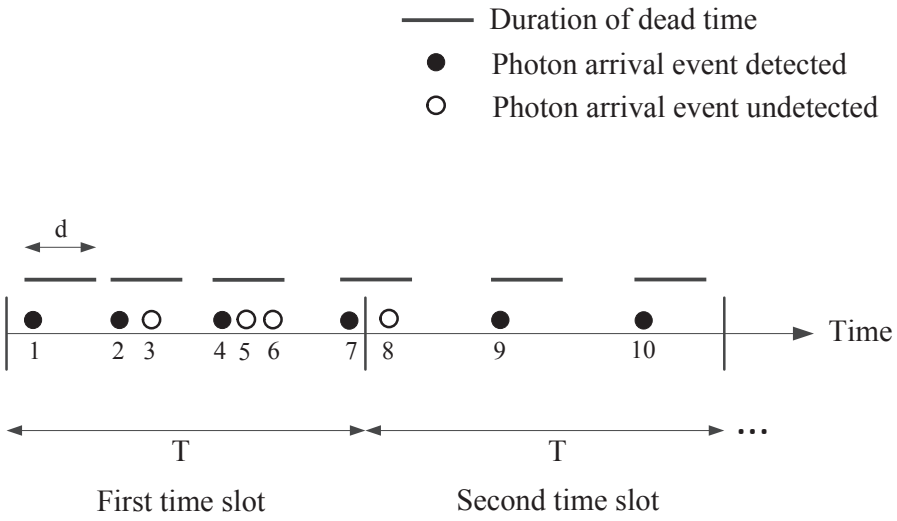

Figure 3.24: An illustration to show the effect of dead time on the detection of photons. Here, T and d denote the slot and dead time duration, respectively. In the first time slot, photon arrival events 1, 2, 4, and 7 are detected. However, photon arrival events 3, 5, and 6 are undetected as they lie within the dead time initiated by a previously detected photon. In the second time slot, only photon arrival event 8 is undetected as the dead time initiated by photon arrival event 7 propagates into the second time slot. The maximum number of photons that can be detected within a time slot is $\lceil \frac{T}{d} \rceil$, where $\lceil \cdot \rceil$ denotes the ceiling function.

3.5 Conclusion

The performance of OOK can degrade considerably once room illumination deviates from its assumed value. An increase or even a decrease in background illumination can impair the performance of OOK as its decision threshold could be at a suboptimal value. PPM is a suitable modulation scheme for indoor VLC systems as it is thresholdless, and therefore more robust to fluctuations in background illumination.

A limitation of the analysis is that it examined the case when the dead time of a SPAD is negligible. For an accurate analytical description of the performance of a SPAD-based VLC system, this assumption needs to be relaxed. Nevertheless, this work provides some insights into the performance of SPAD-based systems in indoor environments.

Chapter 4

Broadcasting to SPAD-based Receivers with Multiresolution PPM

Chapter Overview

This chapter describes a new scheme to improve throughput when SPAD-based receivers with diverse capabilities share a common downlink channel. The performance of the proposed scheme is first analyzed. Then, a proof-of-concept experiment is performed to demonstrate the viability of the proposed scheme.

Chapter's guide to notations: we denote the set of non-negative real numbers, $[0, \infty)$, by $\mathbb{R}_0^+$, the set of natural numbers, $\{0, 1, 2, \dots\}$, by $\mathbb{N}$, and the set of non-zero natural numbers, $\mathbb{N}\backslash\{0\}$, by $\mathbb{N}^+$. We use boldface fonts, *e.g.*, $\boldsymbol{a}$, to denote vectors and italic typeface, *e.g.*, a, to denote scalars. The ith element in the jth tuple[1] of a vector is denoted as a_j^i. The following example provides an illustration: a binary sequence (or vector) is denoted as $\boldsymbol{a} = (\overbrace{a_0^0, a_0^1, \dots, a_0^m}^{\text{0th tuple}}, \dots, \overbrace{a_j^0, a_j^1, \dots, \underbrace{a_j^m}_{m\text{th bit in the } j\text{th tuple}}}^{j\text{th tuple}})$, where $a_j^i \in \{0, 1\}$, $i \in \{0, 1, \dots, m\}$, and $m, j \in \{0, 1, 2, \dots\}$. In this example, the tuple is of size m, which is commonly referred to as m-tuple.

The union of an ordered pair, (x, y), taken over a given parameter α, is denoted by $\bigcup_\alpha$. For instance, let $x = \alpha$, $y = 1 - \alpha$, and $0 \leq \alpha \leq 1$; then the union of (x, y) over α is the following straight line:

$$S = \bigcup_{\{\alpha:\ 0 \leq \alpha \leq 1\}} \{\alpha, 1 - \alpha\}. \tag{4.1}$$

The symbol $\times$ denotes the Cartesian product. For example, let $H = \{1, 2\}$ and $T = \{a, b\}$ be two sets; then the Cartesian product of H and T is the following set: $H \times T = \{(1, a), (1, b), (2, a), (2, b)\}$. We denote mapping from one set to another as $H \to T$.

[1] A fixed size sequence of elements.

4.1 Introduction

In the previous chapter it was shown that PPM is an attractive modulation scheme for SPAD-based VLC systems as it is thresholdless. This chapter further explores the use of PPM for broadcasting to SPAD-based receivers.

VLC can provide broad spatial coverage via diffused links (Figure 4.1). In this configuration, light from a wide field of view transmitter scatters from indoor surfaces [89, 90]. This expands coverage area and thus permits mobility of receivers, as opposed to narrow beams of line-of-sight links. An advantage of this system is that it allows a transmitter to broadcast information to several receivers.

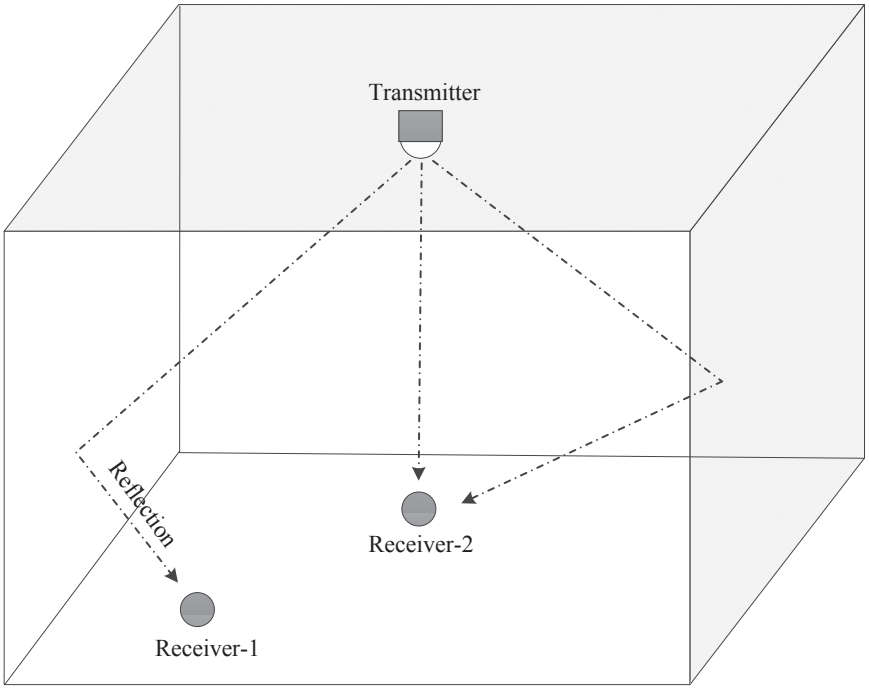

Figure 4.1: Diffuse links in an indoor VLC system.

Broadcasting to SPAD-based receivers is a challenging task as they may have different PPM slot duration requirements. For instance, to attain a given BER, a receiver with a large dead time may require a longer slot duration than a receiver with a small dead time as more photons can be collected when the slot duration increases. An example to illustrate this is provided in Figure 4.2. Broadcasting to receivers with different PPM slot durations is problematic as a receiver with a long slot duration can reduce system throughput. In this chapter, a new modulation scheme is proposed to improve throughput when broadcasting to receivers with diverse slot durations.

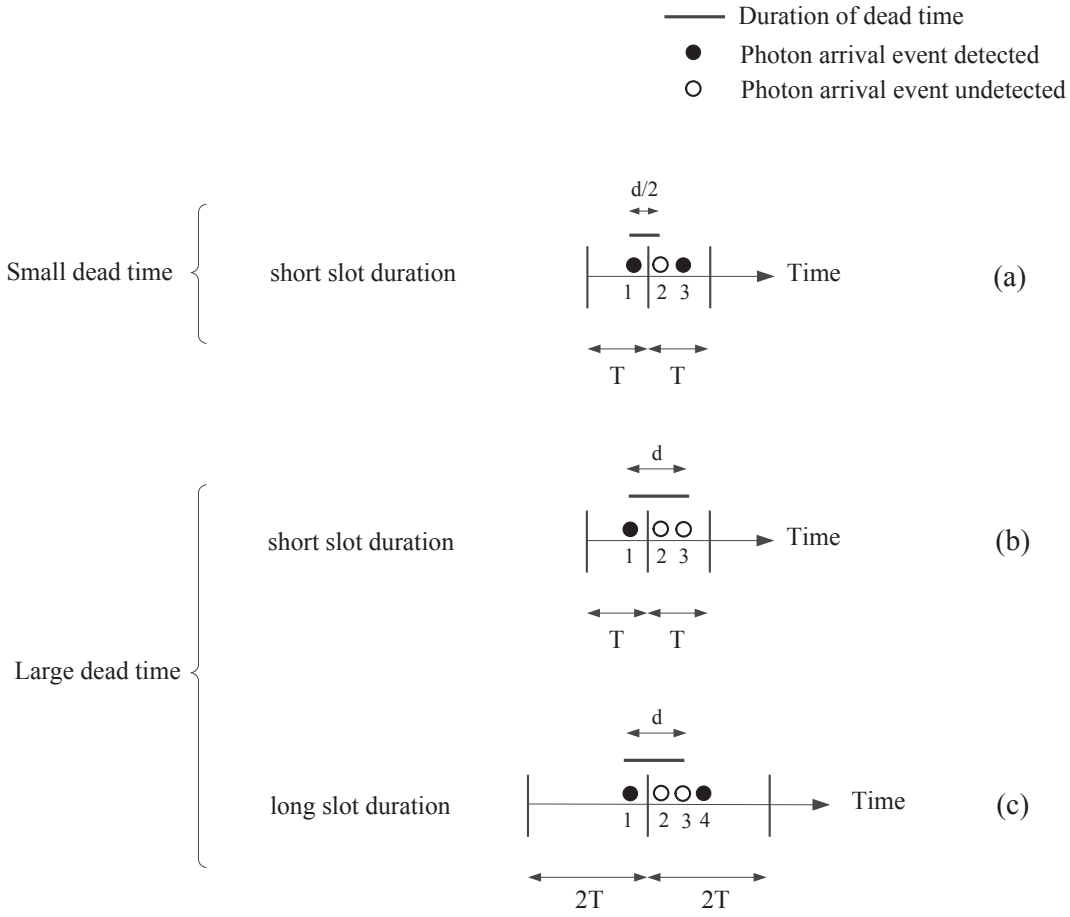

Figure 4.2: An illustration to show the effect of dead time and increasing the slot duration of PPM on the detection of photons. Here, T and d denote the slot and dead time duration, respectively. (a) Only photon arrival event 2 is undetected as the dead time initiated by photon arrival event 1 propagates into the second time slot. (b) Photon arrival event 1 is detected. Photon arrival event 2 and 3 go undetected as they lie within the dead time initiated by a previously detected photon. (c) This modulation scheme has the same dead time as the previous modulation scheme. However, the slot duration is longer. As a result, more photons are detected. Photon arrival events 1 and 4 are detected. Photon arrival event 2 and 3 are undetected as the dead time initiated by photon arrival event 1 propagates into the second time slot.

A simple broadcasting scheme is time-sharing. Figure 4.3 provides an illustration of a time-sharing protocol, and Figure 4.4 shows an example of time-sharing between PPM schemes. In this scheme, a transmitter sends information to receiver-1 for a fraction α of the total broadcasting time, and the remaining $(1-\alpha)$ to receiver-2. In [91] it was shown that time-sharing is suboptimal and more information can be sent by superimposing information [85].

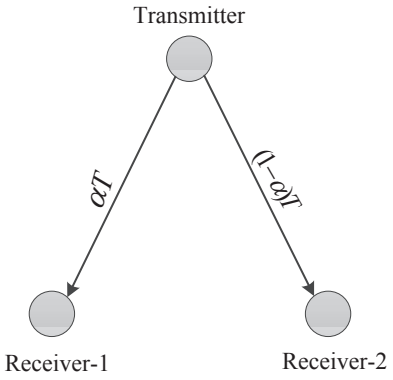

Figure 4.3: Broadcasting by time-sharing. Here, α is the fraction of the total broadcasting time T.

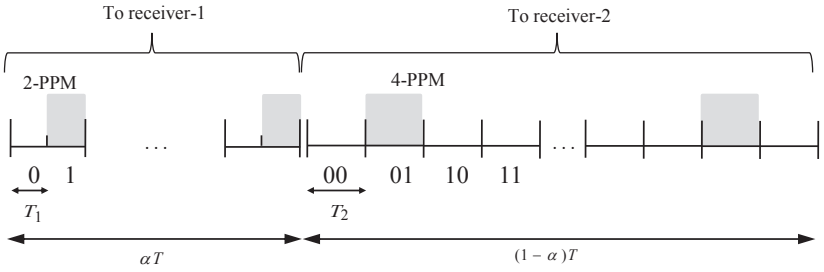

Figure 4.4: Time-sharing between PPM schemes. Here, α is the fraction of the total broadcasting time T. T_1 is the slot duration of receiver-1, and T_2 is the slot duration of receiver-2. $T_1 < T_2$.

In [92], the authors proposed multiresolution modulation schemes that can superimpose information to receivers with different signal-to-noise ratios (SNRs). Figure 4.5 shows an example of a multiresolution quadrature amplitude modulation (QAM) scheme. By this scheme a transmitter sends a satellite point of a constellation to two receivers. A receiver with a low SNR can only detect the clouds of the constellation, whereas a receiver with a high SNR can detect the satellites within a cloud. As a result, more information can be transmitted to two receivers by a single transmission of this multiresolution modulation scheme, compared to time-sharing between two 4-QAM schemes.

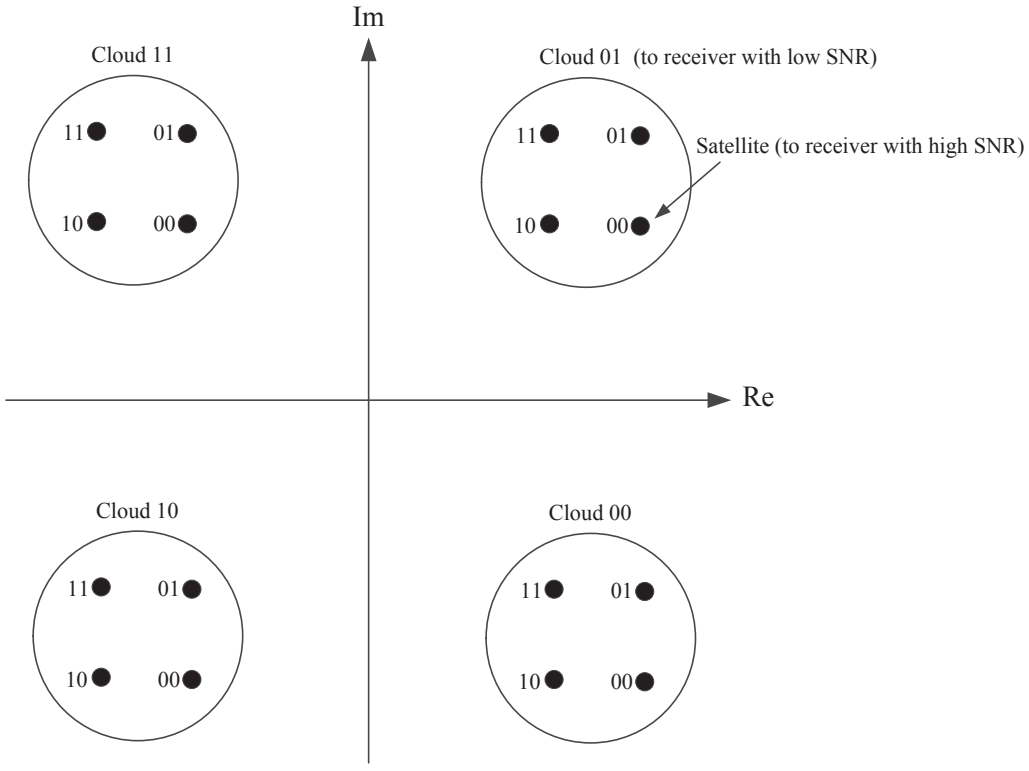

Figure 4.5: Multiresolution QAM.

Exact BER expressions for multiresolution QAM and phase-shift keying (PSK) (also known as hierarchical modulation) schemes have been found [93, 94, 95]. These multiresolution modulation schemes have been incorporated in many standards, such as DVB-S2 [96], DVB-SH [97], and DVB-T [98]. Multiresolution modulation schemes are attractive when broadcasting images [99] and videos [100] as they can provide grades of quality. For instance, when broadcasting an image to two receiver with different SNRs. A receiver with a low SNR obtains a basic image quality as it can only decode the cloud points of a multiresolution constellation (Figure 4.6). In contrast, a receiver with a high SNR can obtain an enhanced version of the image as it can decode satellite points of a multiresolution constellation (Figure 4.6).

Research to date focuses on studying multiresolution modulation schemes for broadcasting to receivers with different SNRs. So far, however, there has been little discussion about broadcasting to receivers with different time slot durations. In this chapter, a new multiresolution modulation scheme is proposed that can superimpose information when broadcasting to receivers with diverse time slot durations.

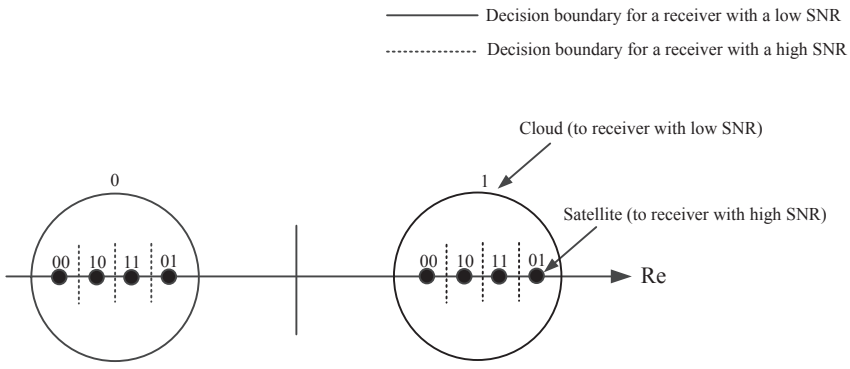

Figure 4.6: Example of a multiresolution constellation.

4.2 System Model

A transmitter sends independent information to two receivers with different PPM time slot durations. The PPM modulation order of receiver-1 is M, while the modulation order of receiver-2 is N. Receiver-1 has a shorter time slot than receiver-2, $T_1 < T_2$. The transmitter sends photons during a PPM signal slot and receivers count the number of photons that arrive, k, according to a Poisson distribution

$$P(k|\lambda) = \frac{\lambda^k}{k!} e^{-\lambda}, \quad k \in \mathbb{N}, \lambda \in \mathbb{R}_0^+, \tag{4.2}$$

where λ is the average number of signal photons per slot. The source of noise in the system is shot noise, which is due to the random arrival of photons. The receivers select the slot with photon as the transmitted signal slot. If no photons arrive in a transmitted symbol, *i.e.*, an erasure occurs, receivers declare an erasure event, $\mathscr{E}$.

4.3 Proposed Scheme

Here we present the proposed M/N-PPM scheme. Let $\boldsymbol{a}$ and $\boldsymbol{b}$ denote the binary sequences of receiver 1 and 2 at the transmitter, respectively

$$\boldsymbol{a} = (a_0^0, a_0^1, \ldots, a_0^m, \ldots, a_j^0, a_j^1, \ldots, a_j^m),$$

$$\boldsymbol{b} = (b_0^0, b_0^1, \ldots, b_0^n, \ldots, b_j^0, b_j^1, \ldots, b_j^n),$$

$$a_j^i, b_j^i \in \{0, 1\},\ m = \log_2 M,\ n = \log_2 N;\ \text{here } i, j \in \mathbb{N},\ \text{and } m, n \in \mathbb{N}^+,$$

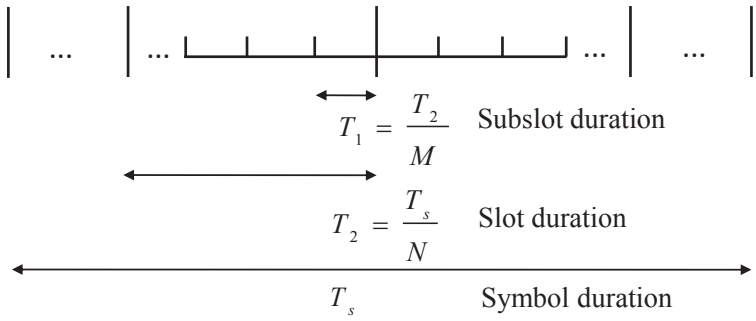

Figure 4.7: General structure of an M/N-PPM symbol.

where a_j^i is the ith bit in an m-tuple, and similarly b_j^i is the ith bit in an n-tuple.

Figure 4.7 illustrates the general structure of an M/N-PPM symbol. Various M/N-PPM frames are provided in Appendix B. The symbol interval, T_s, of M/N-PPM is divided into N time slots of duration T_2. Each of the N slots is further divided into M subslots of duration T_1. An M/N-PPM encoder maps a block of m bits from receiver-1 and n bits from receiver-2 to an M/N-PPM symbol. Based on the value of m and n, the transmitter sends photons in one of the MN subslots. Receiver-2 counts the number of photons in each slot, while receiver-1 counts the number of photons in each subslot to determine the transmitted symbol.

More formally, the encoding and decoding process can be described as follows:

Encoder: The M/N-PPM encoder maps m-tuple of bits from receiver-1 and n-tuple of bits from receiver-2 into a codeword

$$\psi : \{0, 1, \cdots, 2^m - 1\} \times \{0, 1, \cdots, 2^n - 1\} \to \mathcal{X}, \tag{4.3}$$

where $\mathcal{X}$ is the input alphabet of the channel.

Decoders: A decoder maps a received codeword into an m-tuple for receiver-1, and an n-tuple for receiver-2

$$\phi_1 : \mathcal{Y}_1 \to \{0, 1, \cdots, 2^m - 1, \mathscr{E}\} \tag{4.4}$$

$$\phi_2 : \mathcal{Y}_2 \to \{0, 1, \cdots, 2^n - 1, \mathscr{E}\}, \tag{4.5}$$

where ϕ_1 and ϕ_2 are the decoders for receivers 1 and 2, respectively. $\mathcal{Y}_1$ and $\mathcal{Y}_2$ are the output alphabets of the channel for receiver 1 and 2, respectively. The output alphabets have an additional erasure symbol, $\mathscr{E}$. This is due to the erasure case, which occurs when no photons are detected in a symbol interval. The probability of an erasure event, from (4.2), is $\Pr(\mathscr{E}) \triangleq P(0|\lambda) = e^{-\lambda}$.

Example: Figure 4.9 shows an example of transmission. Here, the PPM slot duration of receiver-2 is twice of that of receiver-1. In this example, a 2-PPM scheme is used for transmission to receiver-1, and an 4-PPM scheme for receiver-2. The transmitted bits are $a_j^0 = 1$, and $b_j^0 b_j^1 = 10$ to receiver-1 and receiver-2, respectively. The transmitter uses a multiresolution 2/4-PPM frame, and sends a photons in the depicted subslot in Figure 4.9. Receiver-1 counts the number of photons in each of the 8 subslots of the 2/4-PPM frame, while receiver-2 counts the number of photons in each of the 4 slots of the 2/4-PPM frame to determine the transmitted information. The 2/4-PPM scheme superimposes the message intended for receiver-1, $a_j^0 = 1$, on the message, $b_j^0 b_j^1 = 10$, intended for receiver-2.

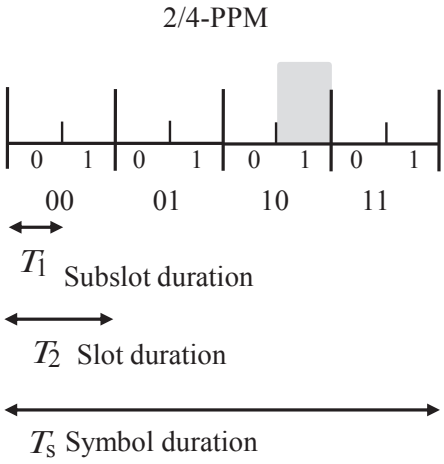

Figure 4.9: Example of transmission using a 2/4-PPM scheme. The transmitted bits are $a_j^0 = 1$, and $b_j^0 b_j^1 = 10$ to receiver-1 and receiver-2, respectively.

4.4 Analysis

The capacity of a Q-ary PPM scheme over a Poisson channel is given by [81],

$$C = (1 - e^{-\lambda}) \ln Q \qquad \text{nats/symbol,} \tag{4.6}$$

or equivalently[2]

$$C = \frac{(1 - e^{-\lambda})}{\log_2 e} \ln Q \qquad \text{bits/symbol.} \tag{4.7}$$

A channel symbol is transmitted every MT_1 seconds to receiver-1, when an M-PPM scheme is employed. Accordingly, from (4.7), its capacity is

$$C_1 = \frac{(1 - e^{-\lambda_1})}{MT_1 \log_2 e} \ln M \qquad \text{bits/sec.} \tag{4.8}$$

where λ_1 is the average number of signal photons per slot for receiver-1. When using the proposed scheme, an M/N-PPM symbol is transmitted every $T_1 MN$ seconds. This results in the following capacity of receiver-1

$$C_\Delta = \frac{(1 - e^{-\lambda_1})}{MNT_1 \log_2 e} \ln M \qquad \text{bits/sec.} \tag{4.9}$$

Likewise, the capacity of receiver-2 is

$$C_2 = \frac{(1 - e^{-\lambda_2})}{MNT_1 \log_2 e} \ln N \qquad \text{bits/sec.} \tag{4.10}$$

where λ_2 is the average number of signal photons per slot for receiver-2. When time-sharing is used for broadcasting, a fraction α of the total broad-

[2]One nat is equal to $\log_2 e$ bits ≈ 1.44 bits

casting time is allocated to receiver-1 and the remaining $(1-\alpha)$ to receiver-2. This transmission protocol achieves the following rate pairs

$$C_{TS} = \bigcup_{\{\alpha:\ 0\leq\alpha\leq 1\}} \{R_1 = \alpha C_1, R_2 = (1-\alpha)C_2\}, \tag{4.11}$$

where R_1 and R_2 are the data rates of receiver 1 and 2, respectively. Figure 4.10 shows the capacity region of time-sharing. It can be seen that time-sharing increases the rate of one receiver at the expense of reducing the rate of the other.

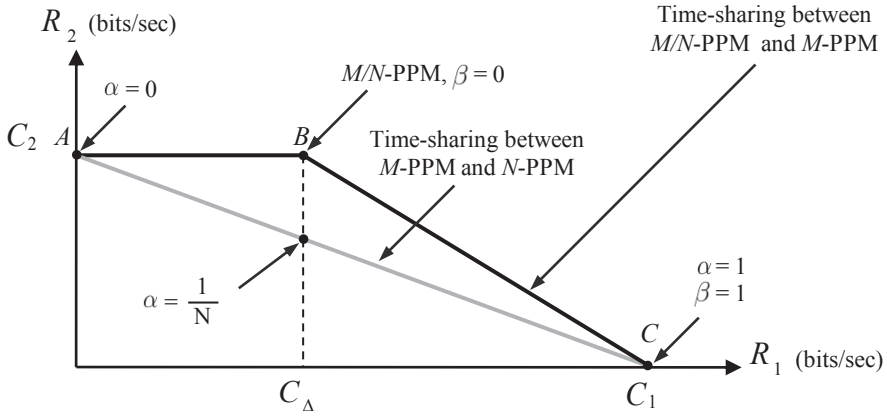

Figure 4.10: Capacity region.

However, the proposed scheme enables the transmitter to communicate to receiver-1 and receiver-2 simultaneously. This yields a larger capacity region than time-sharing as information is superimposed to receiver-1 at a rate of C_Δ. Figure 4.10 provides a comparison between traditional time-sharing and the proposed scheme. Data rates on the line segment AC can be achieved by time-sharing M-PPM with N-PPM. Point B marks the simultaneous data rates that can be obtained by using the proposed M/N-PPM scheme.

Figure 4.11 shows an example of transmission at point B. Data rates on the line segment BC can be attained by time-sharing M/N-PPM with M-PPM. An example of transmission along this line is shown in Figure 4.12. Data rates on the line segment AB occur when M/N-PPM is used, and the amount of information to receiver-1 is varied. The following rate pairs characterize the achievable rates of the proposed scheme

$$C_S = \bigcup_{\{\beta:\ 0\leq\beta\leq 1\}} \{R_1 = \beta C_1 + (1-\beta)C_\Delta, R_2 = (1-\beta)C_2\}, \tag{4.12}$$

where β is the fraction of the total broadcasting time of receiver-1 when M/N-PPM is time shared with M-PPM.

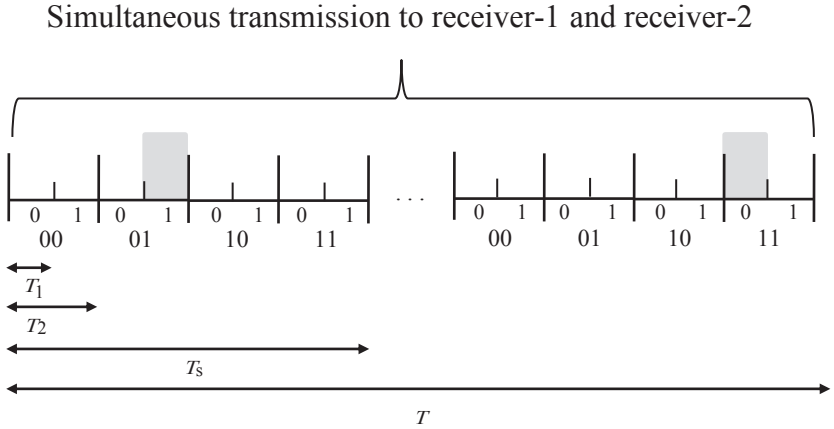

Figure 4.11: Transmission via a multiresolution 2/4-PPM scheme. Here, T_1 is the subslot duration, T_2 is the slot duration, T_s is the symbol duration, and T is the total broadcasting time.

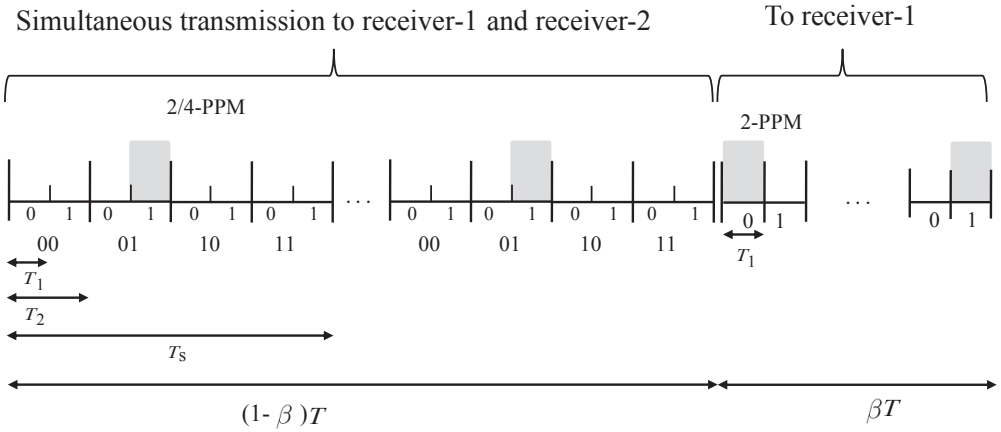

Figure 4.12: Time-sharing between 2/4-PPM with 2-PPM. Here, T_1 is the slot/subslot duration, T_2 is the slot duration, T_s is the symbol duration, and β is the fraction of the broadcasting time T of receiver-1.

4.5 Experiment

The aim of this section is to demonstrate viability of the proposed M/N-PPM scheme. A proof-of-concept experiment is conducted, in which an M/N-PPM scheme is used for broadcasting to two receivers equipped with SPADs and with different slot durations. Figure 4.13 and Figure 4.14 shows the experimental apparatus.

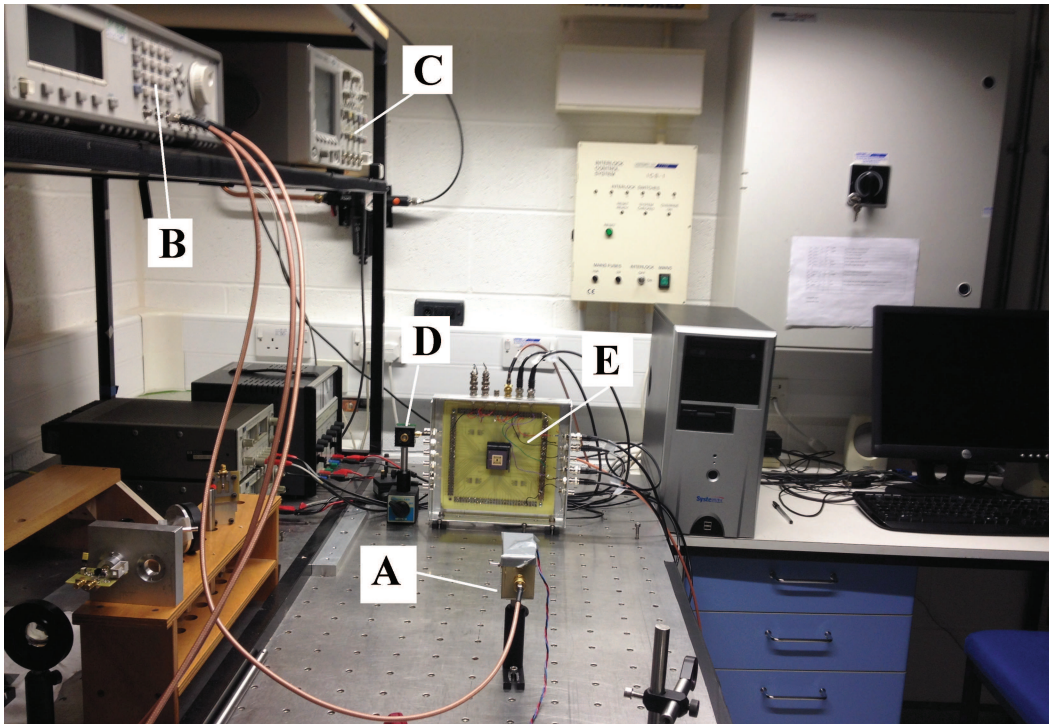

Figure 4.13: Apparatus: (A) Transmitter (*in-house built*), (B) Pulse generator (*HP B1130A*), (C) Oscilloscope (*Agilent MSO6104A*), (D) SPAD-1 (*SensL PCDMini0020*), (E) SPAD-2 (*Designed by Oxford MCAD Research Group*).

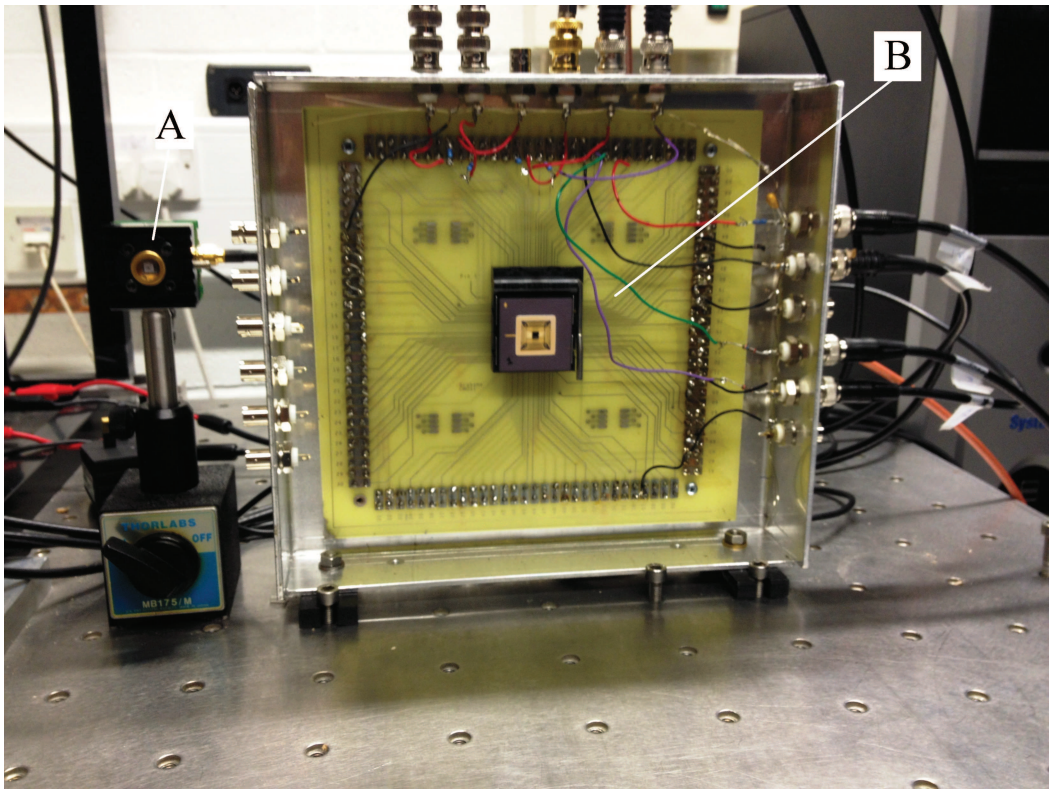

Figure 4.14: (A) SPAD-1 (*SensL PCDMini0020*), (B) SPAD-2 (*Designed by Oxford MCAD Research Group*).

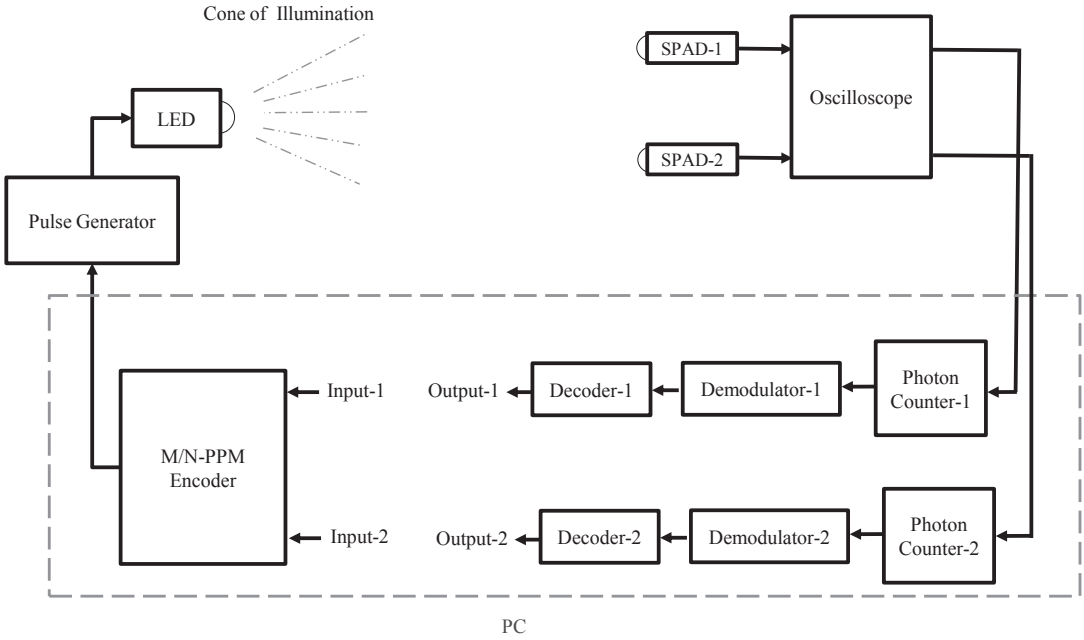

Figure 4.15: Schematic of the experimental setup.

4.5.1 Experimental Apparatus and Methods

Figure 4.15 shows a block diagram of the experimental setup. The apparatus consists of a PC, a pulse generator, an LED, two SPADs, and an oscilloscope.

The pulse-generator drives an LED that illuminates two SPADs. Specifications of the SPADs and the experimental parameters are summarized in Table 4.1. Photons detected by SPADs generate pulses, called photon-pulses, which are captured by an oscilloscope. Figure 4.16 shows an input signal to the LED and the photon-pulses captured by the oscilloscope. The output of the oscilloscope is passed to a photon-counter that is implemented on a PC.

Table 4.1: Experimental parameters

Parameter	Value
Centre wavelength of LED	~ 640 nm
Slot duration (T_2)	4 μsec
Slot/subslot duration (T_1)	2 μsec
Symbol duration (T_s)	16 μsec
Active area of SPAD-1 and 2	$\sim 3.14 \times 10^{-10}$ m^2
Average DCR[1]of SPAD-1	~ 230 Hz
Average DCR of SPAD-2	~ 3.70 kHz
Dead time of SPAD-1 (non-extensible)	~ 97 $n$sec
Dead time of SPAD-2 (extensible)	~ 103 $n$sec
PDP[2]of SPAD-1 at 640 nm	$\sim 15\%$
PDP of SPAD-2 at 640 nm	$\sim 20\%$

[1]Dark count rate. [2]Photon-detection probability.

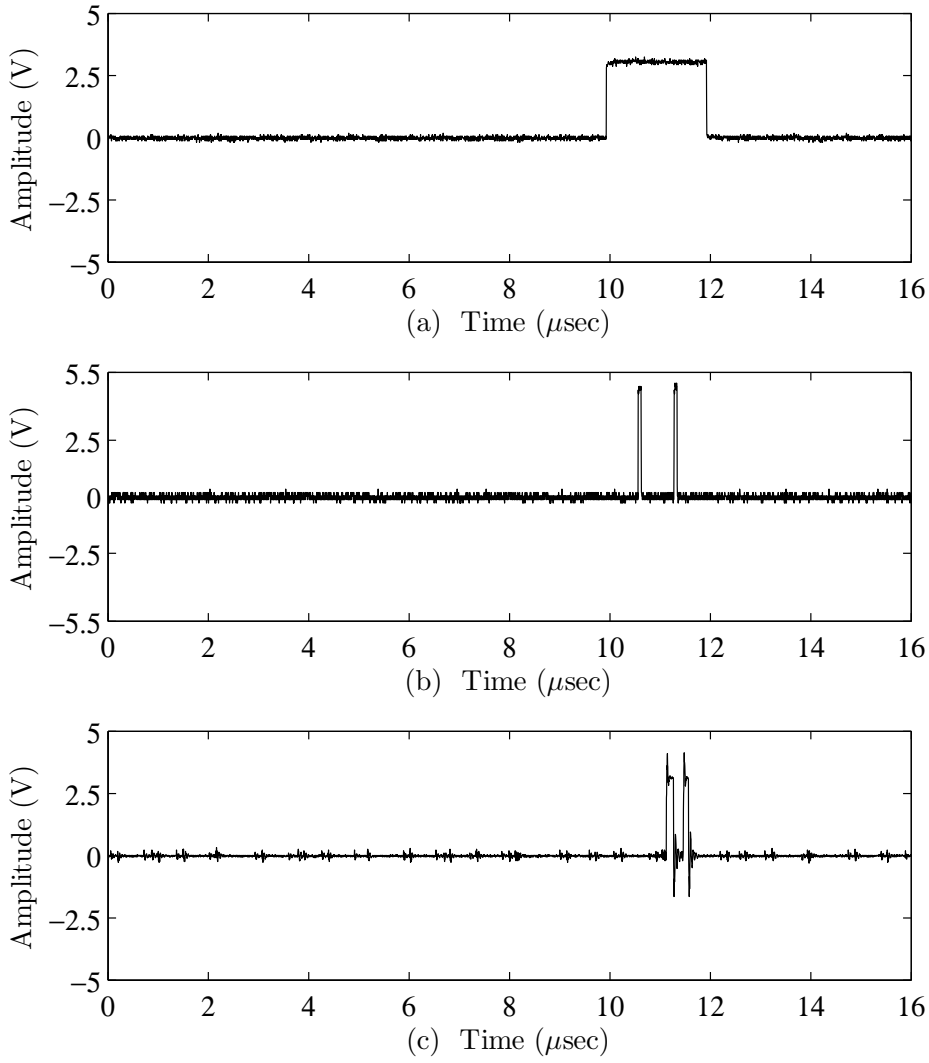

Figure 4.16: (a) Input 2/4-PPM signal to LED, (b) Response of SPAD-1, (c) Response of SPAD-2.

In the experiment, input bits for receiver-1 and receiver-2 were randomly generated, and encoded, offline by a PC. The encoder maps input bits to an M/N-PPM symbol. The photon-counter of receiver-1 counts the number of photons detected in each subslot of an M/N-PPM symbol, while the photon-counter of receiver-2 counts the number of photons detected in each slot of an M/N-PPM symbol. The output of the photon-counter is fed to a hard-decision demodulator, which estimates the transmitted M/N-PPM symbol. The slot/subslot with the most number of photon counts is chosen as the transmitted signal slot/subslot by the demodulator. The output of the demodulator is then passed to a decoder that maps an M/N-PPM symbol into output bits. The demodulators and decoders were both implemented on a PC. A flowchart of software used in the experiment is presented in Appendix C.

The experiment was carried out in a dark room to reduce noise photons. The arrival-time of a photon was determined by the rising edge of a photon-pulse. In the experiment, an optical power-meter was used to estimate the intensity falling on a SPAD.

For receiver-1 and receiver-2, an initial experiment was conducted to attain a BER of 10^{-3}. This was accomplished by varying the intensity of the LED light source until a BER of 10^{-3} was achieved. In the experiment, 3×10^4 bits were transmitted to each receiver.

4.5.2 Experimental Results and Discussion

An ideal photon-counting receiver (*i.e.,* quantum-limited receiver) will serve as a reference for comparison as it is the best sensitivity a receiver can attain [101]. An ideal photon-counting receiver has a photon-detection probability (PDP) of 100%, but no dark counts, afterpulses, and dead time. The BER of an ideal photon-counting receiver is determined by the probability of an erasure, $\mathscr{E}$, that is, the probability that no photons arrive in a symbol duration,

$$\text{BER} = \frac{1}{2}\Pr(\mathscr{E}) = \frac{1}{2}e^{-\lambda}, \tag{4.13}$$

where, λ is the average number of signal photons per slot.

At a BER of 10^{-3} the sensitivity of receiver-1 was measured to be ~ -84 dBm (at 250 $k$bits/sec for 2-PPM), and ~ -89 dBm for receiver-2 (at 125 $k$bits/sec for 4-PPM). In contrast, an ideal photon-counting receiver would require a power of ~ -93 dBm for receiver-1, and ~ -99 dBm for receiver-2 to attain a BER of 10^{-3}.

Figure 4.17 shows the capacity region when 2-PPM, 4-PPM, and 2/4-PPM are used. The point at which $\alpha = 0.25$ will serve as a basis for comparison; similar conclusions can be drawn for other value of α. Time-sharing 2-PPM with 4-PPM at $\alpha = 0.25$ yields a data rate of 62.5 and 93.75 ($k$bits/sec) to receiver-1 and receiver-2, respectively. In contrast, the 2/4-PPM scheme is able to superimpose a data rate of 62.5 ($k$bits/sec) to receiver-1, and simultaneously increase the data rate of receiver-2 from 93.75 to 125 ($k$bits/sec).

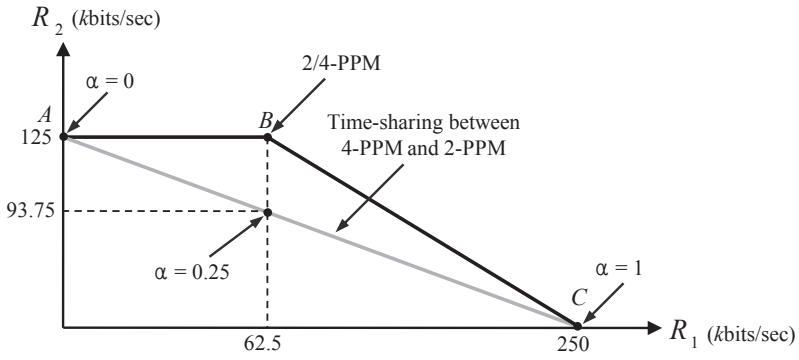

Figure 4.17: Capacity region. R_1 and R_2 are the data rates to receiver-1 and receiver-2, respectively. Here, α is a fraction of the total broadcasting time.

To attain a BER of 10^{-3} an intensity of $\sim 3.25 \times 10^6$ and $\sim 3.15 \times 10^6$(photons/sec) was required by receiver-1 and receiver-2, respectively, when time-sharing was used. In contrast, an intensity of $\sim 3.6 \times 10^6$ and $\sim 4.6 \times 10^6$ (photons/sec) was required by receiver-1 and receiver-2, respectively, for a BER of 10^{-3} when 2/4-PPM was used.

For receiver-1, the intensities required by time-sharing and 2/4-PPM to attain a BER of 10^{-3} at a data rate of 62.5 ($k$bits/sec) are similar (difference less than 0.5 dB); the deviation between the intensities is due to experimental variation. For receiver-2, the intensity required to attain a BER of 10^{-3} is $\sim$ 1.6 dB more for 2/4-PPM than time-sharing as the transmission rate of 2/4-PPM is higher (the difference between the data rates is 31.25 $k$bits/sec).

4.6 Conclusion

A new multiresolution modulation scheme has been proposed for broadcasting to receivers with different slot durations. The proposed M/N-PPM scheme can superimpose information, and therefore improve system throughput over the traditional time-sharing approach. Two receivers equipped with SPADs were used in an experiment to assess the performance of the proposed M/N-PPM scheme. A data rate of 62.5 $k$bits/sec was superimposed by a 2/4-PPM scheme operating at a subslot and slot duration of 2 μsec and 4 μsec, respectively. Results suggest that M/N-PPM has a potential to improve system throughput. A limitation of the study is that it considered only two receivers. In an indoor environment, however, many receivers with diverse time slot requirements may share a common downlink channel. Nevertheless, this work is a step towards solving this issue.

Chapter 5

Conclusions and Future Work

Chapter Overview

So far this thesis has focused on practical considerations when using SPADs in VLC. In this chapter, conclusions are drawn from the project and ideas for future research are proposed. The thesis concludes with some final remarks.

5.1 Conclusions

SPADs can potentially enhance data rates of VLC systems. However, one must also consider that they are sensitive to background illumination. In this thesis, the impact of changes in background illumination on the performance of a SPAD-based VLC system is investigated analytically and experimentally. Analytical expressions are derived to quantify performance in terms of capacity, photon-efficiency, and BER. In addition, an experiment was carried out to gain an understanding of the performance of a SPAD-based VLC system in an indoor environment. The conclusion drawn from the study can be summarized as follows: *Though PPM has a lower data rate than OOK, it is a suitable modulation scheme for SPAD-based VLC systems as it is less sensitive to changes in background illumination.*

This thesis also addresses the problem of broadcasting to SPAD-based receivers with diverse capabilities. A multiresolution PPM scheme is developed to enhance data rates when receivers with different PPM slot durations share a downlink channel. The performance of the proposed scheme is analyzed and compared with the traditional time-sharing approach. Furthermore, an experiment in which two receivers equipped with SPADs was conducted to assess the performance of the proposed scheme in practice. A data rate of 62.5 $k$bits/sec was superimposed by the proposed scheme operating at operating at a subslot and slot duration of 2 μsec and 4 μsec, respectively. The conclusion drawn from the study can be summarized as follows: *The proposed multiresolution PPM scheme can superimpose information, and therefore has*

the potential to improve system throughput over the traditional time-sharing approach.

5.2 Future Work

This work can be extended both theoretically and experimentally. The avenues for future research are as follows:

- *Mathematical model*

  One direction for exploration is the development a mathematical model to predict the BERs of modulation schemes with a dead time constraint. With such a mathematical model, one can optimize system parameters (*e.g.*, signal intensity, and slot duration).

  The BER is a function of signal photons, noise photons, and the fraction $\delta = \frac{d}{T}$; where d is the dead time duration, and T is the slot duration. The BER increases with δ for the following reasons:

  - As δ increases less signal photons are detected, since the maximum number of photons that can be detected within a time slot is $\lceil \frac{T}{d} \rceil$ (or equivalently $\lceil \frac{1}{\delta} \rceil$); where $\lceil \cdot \rceil$ denotes the ceiling function.
  - The dead time causes intersymbol interference when it propagates into a subsequent OOK slot. This is illustrated in Figure 5.1.

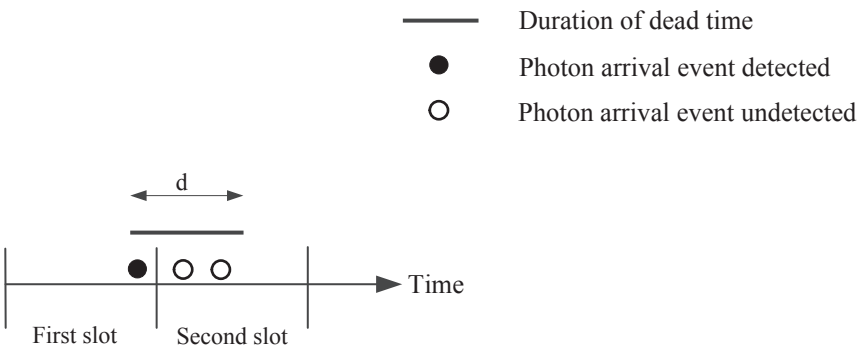

Figure 5.1: Intersymbol interference caused by dead time. The dead time initiated by the photon in the first slot interferes with photons in the second slot.

- *Multiresolution OOK*

  Consider the following broadcast scenario, where two receivers equipt with SPADs share a downlink channel. Receiver-1 has less noise photons than receiver-2. Time-sharing can be used to broadcast to both receivers. However, more information can be transmitted by a multiresolution OOK scheme.

  An example of transmission using a multiresolution OOK is shown in Figure 5.2. Receiver-1 has a low noise intensity and therefore can detect the fine satellite, while receiver-2, with a high noise intensity, detects the cloud. Using this scheme a single transmission of a satellite point conveys information, simultaneously, to both receivers.

  An interesting research topic is investigating the performance of multiresolution OOK, on a Poisson channel, theoretically/experimentally.

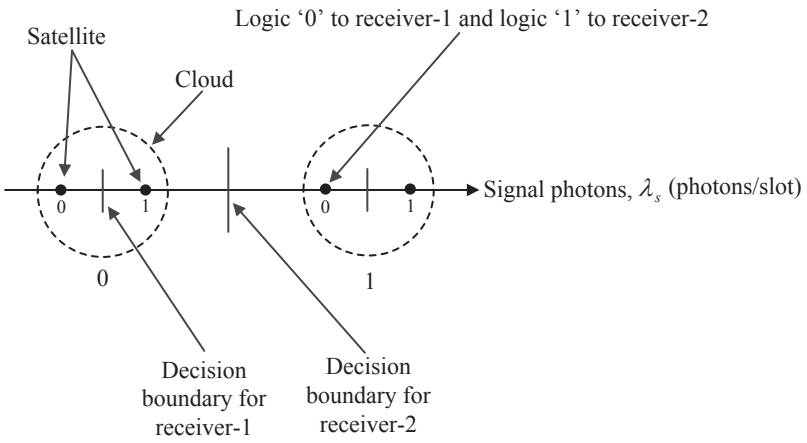

Figure 5.2: Constellation diagram of multiresolution OOK.

- *Array of SPADs*

  A limitation of SPADs is that they have a dead time. However, this can be overcome by using an array of SPADs. As the number of SPADs of a receiver increases, the BER can improve. The intuitive explanation for this is the following: when a SPAD detects a photon it becomes inactive during the dead time. Signal photons that arrive during this period will go undetected. However, as the number of SPADs increase the probability that all SPADs of a receiver are inactive at the same moment decreases. As a result, the BER can improve.

  This configuration poses some interesting questions for future research: how many SPADs are needed to achieve a given BER? and how does capacity scale with the number of SPADs?

5.3 Final Remarks

SPADs are novel devices that have a great potential. Their high sensitivity and compactness makes them appealing. It is hoped that this thesis will motivate future research in this area.

APPENDICES

Appendix A

Flowcharts of Software

This appendix illustrates the software used in the experiment of *Chapter 3*.

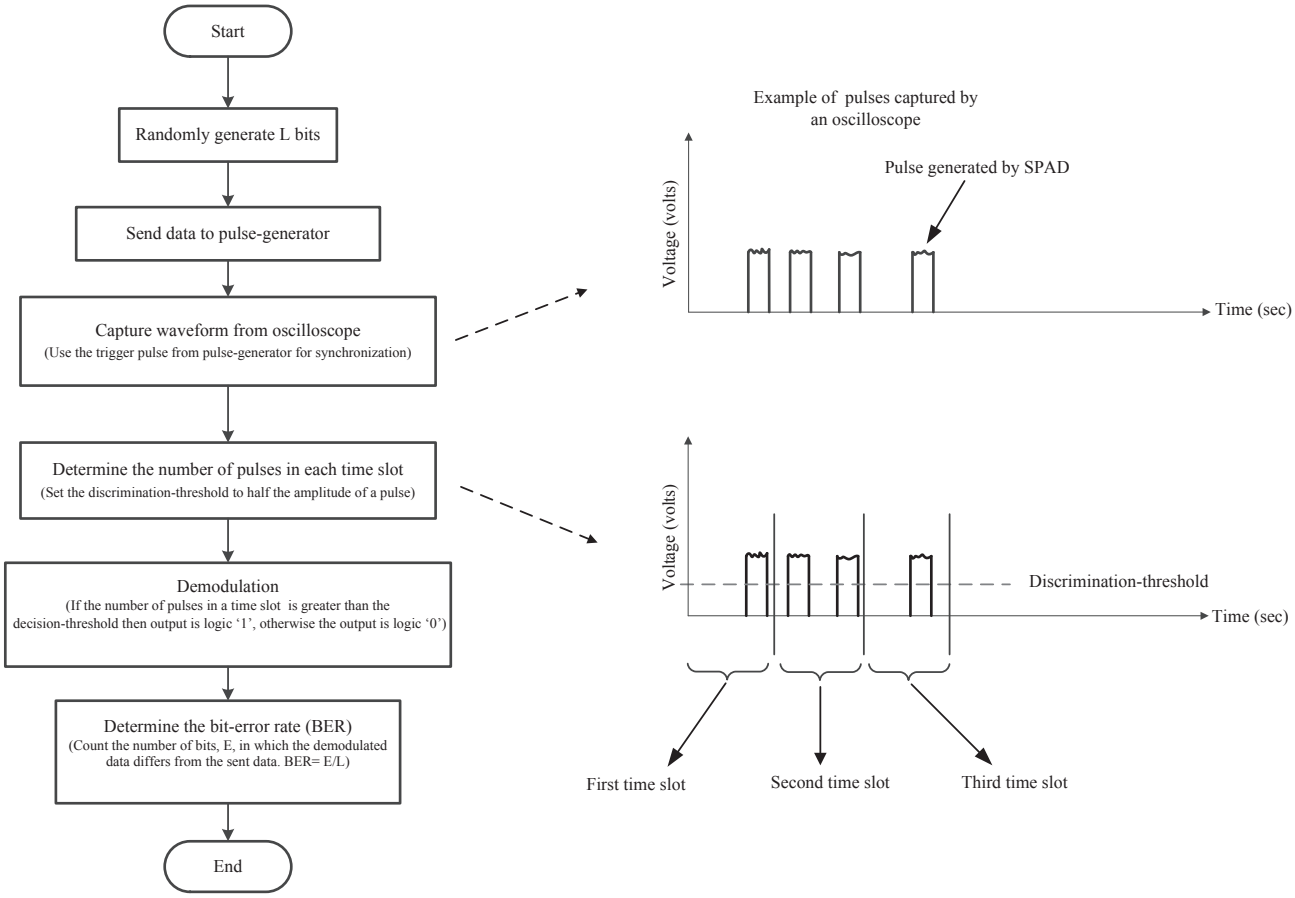

Figure A.1: Flowchart of software used in experiment for OOK.

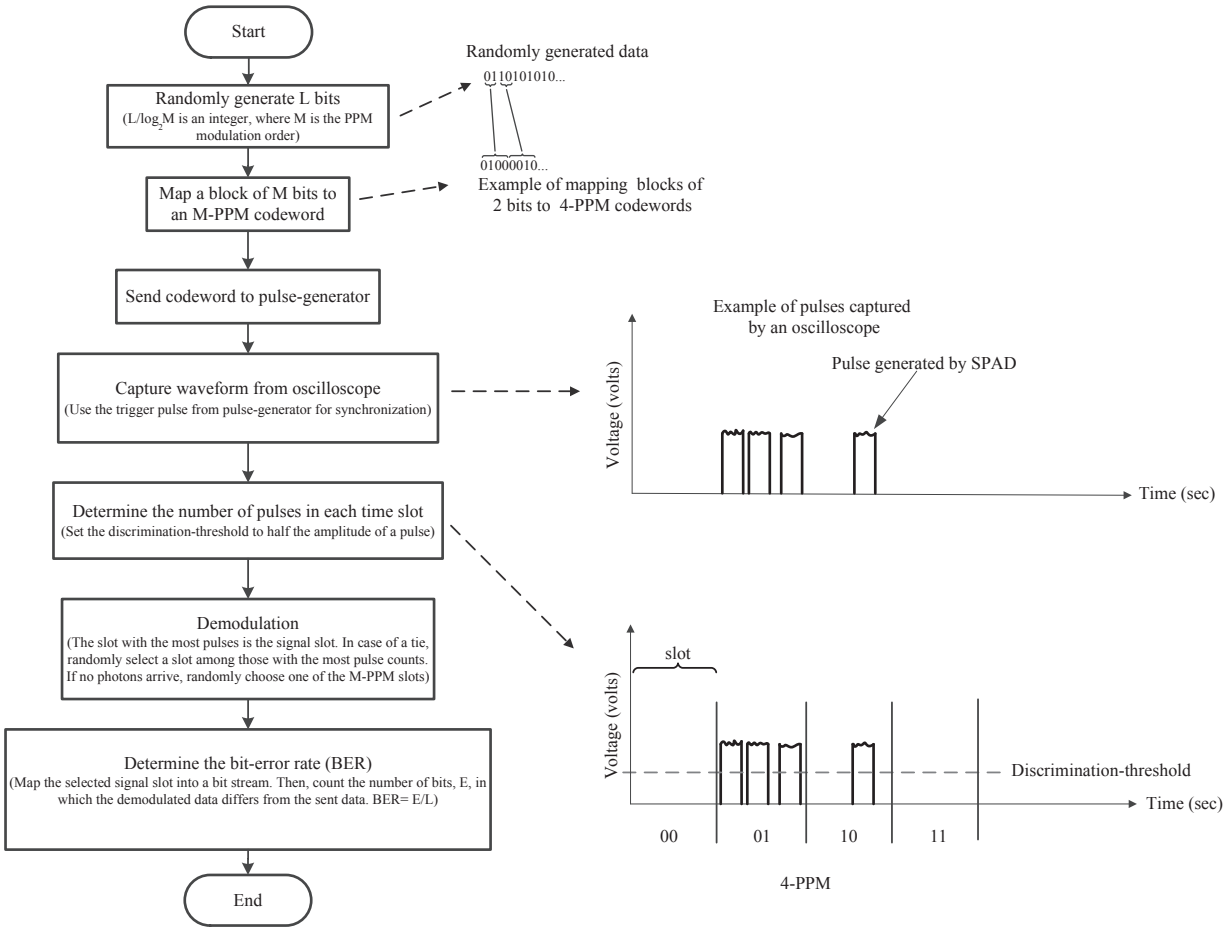

Figure A.2: Flowchart of software used in experiment for PPM.

Appendix B

Multiresolution PPM Frames

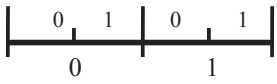

Figure B.1: Multiresolution 2/2-PPM frame.

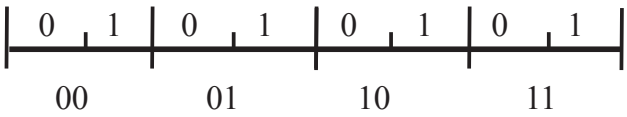

Figure B.2: Multiresolution 2/4-PPM frame.

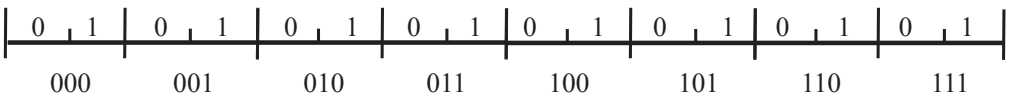

Figure B.3: Multiresolution 2/8-PPM frame.

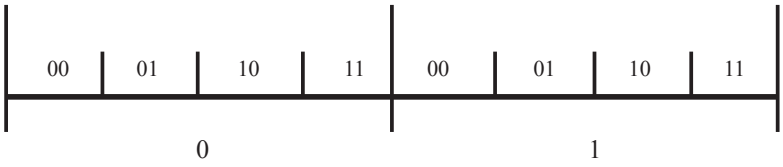

Figure B.4: Multiresolution 4/2-PPM frame.

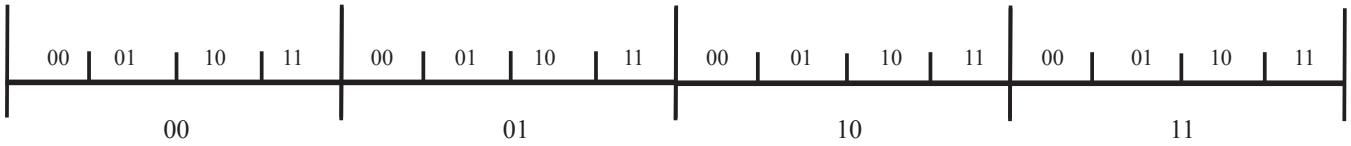

Figure B.5: Multiresolution 4/4-PPM frame.

Figure B.6: Multiresolution 8/4-PPM frame.

Appendix C

Flowchart of Software

This appendix illustrates the software used in the experiment of *Chapter 4*.

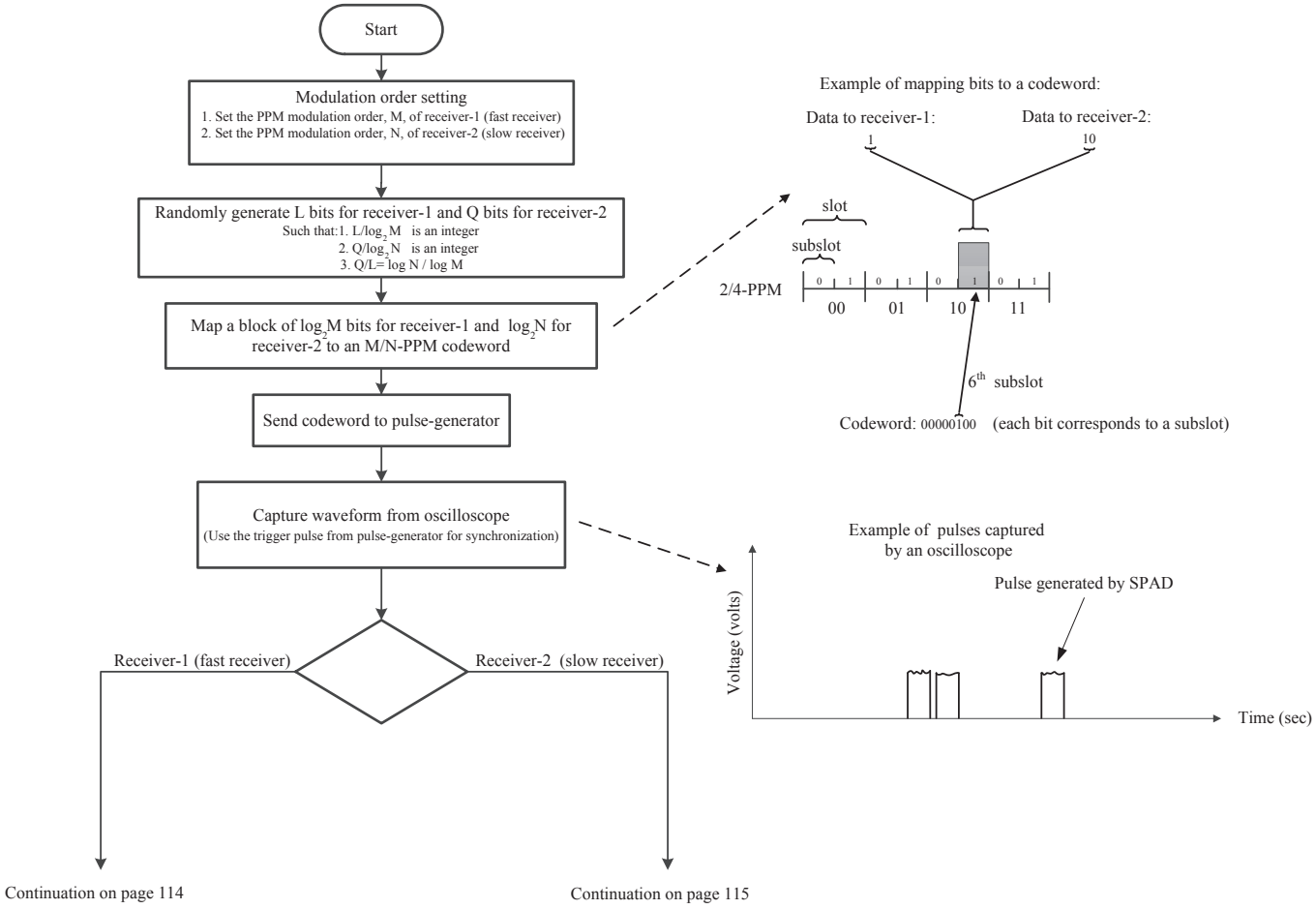

Figure C.1: Flowchart of software used in experiment for multiresolution PPM.

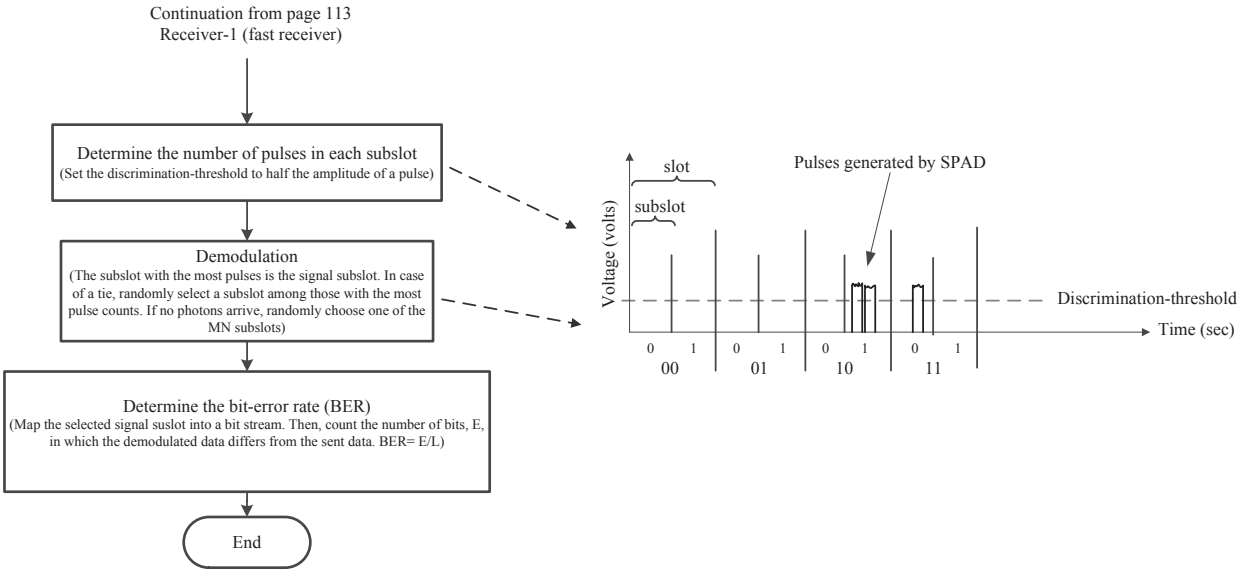

Figure C.2: Continuation of Figure C.1: receiver-1.

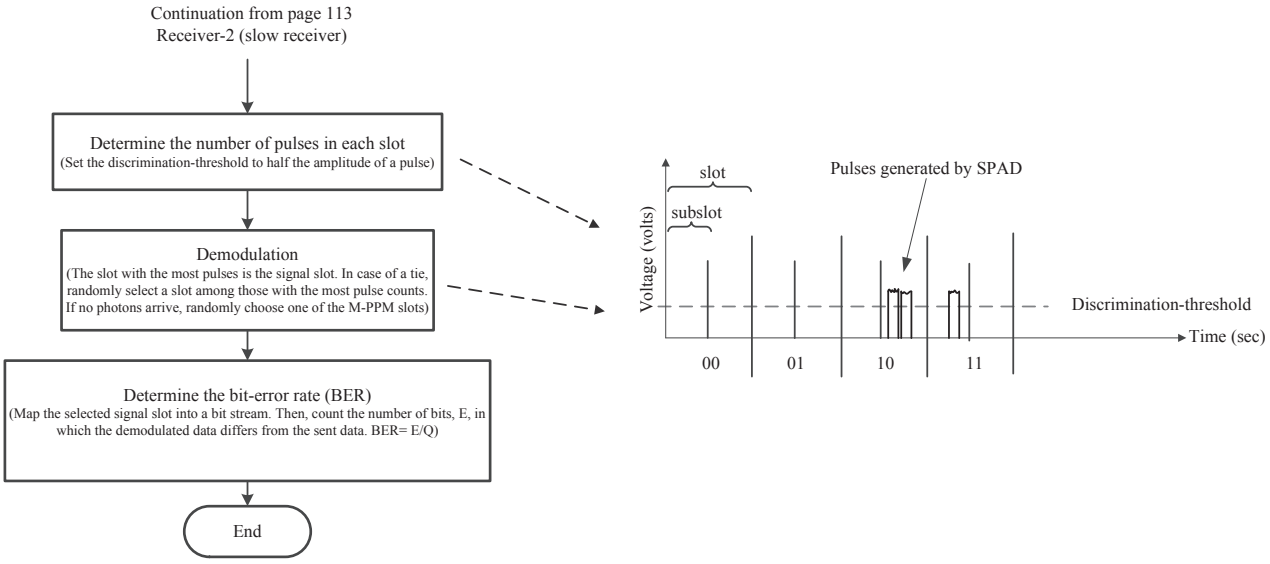

Figure C.3: Continuation of Figure C.1: receiver-2.

References

[1] Cisco Corporation, "Cisco visual networking index: Global mobile data traffic forecast update, 2013-2018," *White Paper, February*, 2014.

[2] The U.S. Census Bureau, "World Population," April 2014. [Online]. Available: http://www.census.gov

[3] Real Wireless, "UK will need 300 MHz more cellular and 350 MHz more Wi-Fi spectrum by 2020 says real wireless," October 2013. [Online]. Available: http://www.realwireless.biz/2013/11/28/uk-will-need-300mhz-more-cellular-and-350mhz-more-wi-fi-spectrum-by-2020-says-real-wireless/

[4] H. Haas, "High-speed wireless networking using visible light," *SPIE Newsroom*, April 2013.

[5] H.-H. Lu, Y.-P. Lin, P.-Y. Wu, C.-Y. Chen, M.-C. Chen, and T.-W. Jhang, "A multiple-input-multiple-output visible light communication system based on VCSELs and spatial light modulators," *Optics Express*, vol. 22, no. 3, pp. 3468–3474, 2014.

[6] M. Craford, R. Dupuis, M. Feng, F. Kish, and J. Laskar, "50th anniversary of the light-emitting diode (LED): An ultimate lamp," *Proceedings of the IEEE*, vol. 101, no. 10, pp. 2154–2157, October 2013.

[7] J. K. Kim and E. F. Schubert, "Transcending the replacement paradigm of solid-state lighting," *Optics Express*, vol. 16, no. 26, pp. 21 835–21 842, 2008.

[8] E. F. Schubert, J. K. Kim, H. Luo, and J. Xi, "Solid-state lighting - a benevolent technology," *Reports on Progress in Physics*, vol. 69, no. 12, p. 3069, 2006.

[9] Philips Corporation, "LED bulbs," April 2014. [Online]. Available: http://www.philips.co.uk/c/led-light-bulbs/19964/cat/

[10] S. Rajagopal, R. D. Roberts, and S.-K. Lim, "IEEE 802.15. 7 visible light communication: modulation schemes and dimming support," *IEEE Communications Magazine*, vol. 50, no. 3, pp. 72–82, 2012.

[11] H. Elgala, R. Mesleh, and H. Haas, "Indoor optical wireless communication: Potential and state-of-the-art," *IEEE Communications Magazine*, vol. 49, no. 9, pp. 56–62, September 2011.

[12] G. Pang, T. Kwan, H. Liu, and C.-H. Chan, "LED wireless," *Industry Applications Magazine, IEEE*, vol. 8, no. 1, pp. 21–28, January 2002.

[13] R. V. Steele, "The story of a new light source," *Nature photonics*, vol. 1, no. 1, pp. 25–26, 2007.

[14] J. Prat, P. E. Balaguer, J. M. Gené, O. Díaz, and S. Figuerola, *Fiber-to-the-Home Technologies*. Dordrecht: Kluwer Academic Publishers, 2002.

[15] "IEEE standard for local and metropolitan area networks–part 15.7: Short-range wireless optical communication using visible light," *IEEE Std 802.15.7-2011*, pp. 1–309, 2011.

[16] D. Kedar and S. Arnon, "Urban optical wireless communication networks: the main challenges and possible solutions," *IEEE Communications Magazine*, vol. 42, no. 5, pp. S2 – S7, May 2004.

[17] M. Saadi, L. Wattisuttikulkij, Y. Zhao, and P. Sangwongngam, "Visible light communication: Opportunities, challenges and channel models," *International Journal of Electronics & Informatics*, vol. 2, no. 1, 2013.

[18] Y. H. Chung and S. bin Oh, "Efficient optical filtering for outdoor visible light communications in the presence of sunlight or artificical light," in *Intelligent Signal Processing and Communications Systems (ISPACS), 2013 International Symposium on*, November 2013, pp. 749–752.

[19] T. Komine, S. Haruyama, and M. Nakagawa, "A study of shadowing on indoor visible-light wireless communication utilizing plural white LED lightings," *Wireless Personal Communications*, vol. 34, no. 1-2, pp. 211–225, 2005.

[20] J. Alwan, "Eye safety and wireless optical networks (WONs)," *white paper*, 2001.

[21] L. Grobe, A. Paraskevopoulos, J. Hilt, D. Schulz, F. Lassak, F. Hartlieb, C. Kottke, V. Jungnickel, and K.-D. Langer, "High-speed visible light communication systems," *IEEE Communications Magazine*, vol. 51, no. 12, pp. 60–66, December 2013.

[22] H.-S. Kim, D.-R. Kim, S.-H. Yang, Y.-H. Son, and S.-K. Han, "An indoor visible light communication positioning system using a RF carrier allocation technique," *Journal of Lightwave Technology*, vol. 31, no. 1, pp. 134–144, January 2013.

[23] A. Jovicic, J. Li, and T. Richardson, "Visible light communication: opportunities, challenges and the path to market," *IEEE Communications Magazine*, vol. 51, no. 12, pp. 26–32, December 2013.

[24] "Vehicle safety communications project task 3 final report identify intelligent vehicle safety applications enabled by DSRC," *U.S. Nat'l. Highway Traffic Safety Admin., Tech. Rep.*, 2005.

[25] S.-H. Yu, O. Shih, H.-M. Tsai, and R. Roberts, "Smart automotive lighting for vehicle safety," *IEEE Communications Magazine*, vol. 51, no. 12, pp. 50–59, 2013.

[26] J.-H. Yoo, R. Lee, J.-K. Oh, H.-W. Seo, J.-Y. Kim, H.-C. Kim, and S.-Y. Jung, "Demonstration of vehicular visible light communication based on LED headlamp," in *Fifth International Conference on Ubiquitous and Future Networks (ICUFN)*. IEEE, 2013, pp. 465–467.

[27] R. Roberts, P. Gopalakrishnan, and S. Rathi, "Visible light positioning: Automotive use case," in *IEEE Vehicular Networking Conference (VNC)*. IEEE, 2010, pp. 309–314.

[28] D. Pompili and I. F. Akyildiz, "Overview of networking protocols for underwater wireless communications," *IEEE Communications Magazine*, vol. 47, no. 1, pp. 97–102, 2009.

[29] J. Heidemann, W. Ye, J. Wills, A. Syed, and Y. Li, "Research challenges and applications for underwater sensor networking," in *Wireless Communications and Networking Conference, 2006. WCNC 2006. IEEE*, vol. 1, April 2006, pp. 228–235.

[30] G. Baiden, Y. Bissiri, and A. Masoti, "Paving the way for a future underwater omni-directional wireless optical communication systems," *Ocean Engineering*, vol. 36, no. 9, pp. 633–640, 2009.

[31] G. Pang, K.-L. Ho, T. Kwan, and E. Yang, "Visible light communication for audio systems," *IEEE Transactions on Consumer Electronics*, vol. 45, no. 4, pp. 1112–1118, 1999.

[32] T. Komine and M. Nakagawa, "Integrated system of white LED visible-light communication and power-line communication," *IEEE Transactions on Consumer Electronics*, vol. 49, no. 1, pp. 71–79, February 2003.

[33] ——, "Fundamental analysis for visible-light communication system using LED lights," *IEEE Transactions on Consumer Electronics*, vol. 50, no. 1, pp. 100–107, February 2004.

[34] Japan Electronics and Information Technology Industries Association, "CP-1221 - Visible light communications systems," 2007. [Online]. Available: http://www.jeita.or.jp/japanese/standard/book/CP-1221/page=1

[35] ——, "CP-1222 - Visible light ID systems," 2007. [Online]. Available: http://www.jeita.or.jp/japanese/standard/book/CP-1222/page=1

[36] OLEDCOMM, Paris-France, April 2014. [Online]. Available: http://www.oledcomm.com/index.html

[37] pureLiFi, Edinburgh-United Kingdom, April 2014. [Online]. Available: http://purelifi.com/about-us/

[38] The Visible Light Communications Consortium, April 2014. [Online]. Available: http://www.vlcc.net/

[39] Light-Fidelity Consortium, April 2014. [Online]. Available: http://www.lificonsortium.org/index.html

[40] K. Lee, H. Park, and J. R. Barry, "Indoor channel characteristics for visible light communications," *IEEE Communications Letters*, vol. 15, no. 2, pp. 217–219, 2011.

[41] C. G. Lee, C. S. Park, J.-H. Kim, and D.-H. Kim, "Experimental verification of optical wireless communication link using high-brightness illumination light-emitting diodes," *Optical Engineering*, vol. 46, no. 12, pp. 125 005–125 005, 2007.

[42] T. D. Little, P. Dib, K. Shah, N. Barraford, and B. Gallagher, "Using LED lighting for ubiquitous indoor wireless networking," in *Networking and Communications, 2008. WIMOB'08. IEEE International Conference on Wireless and Mobile Computing,*. IEEE, 2008, pp. 373–378.

[43] J. Grubor, S. Randel, K.-D. Langer, and J. W. Walewski, "Broadband information broadcasting using LED-based interior lighting," *Journal of Lightwave technology*, vol. 26, no. 24, pp. 3883–3892, 2008.

[44] L. Zeng, D. O'Brien, H. Minh, G. Faulkner, K. Lee, D. Jung, Y. Oh, and E. T. Won, "High data rate multiple input multiple output (MIMO) optical wireless communications using white LED lighting," *IEEE Journal on Selected Areas in Communications*, vol. 27, no. 9, pp. 1654–1662, 2009.

[45] A. Azhar, T. Tran, and D. O'Brien, "A Gigabit/s indoor wireless transmission using MIMO-OFDM visible-light communications," *IEEE Photonics Technology Letters*, vol. 25, no. 2, pp. 171–174, January 2013.

[46] K. D. Dambul, D. O'Brien, and G. Faulkner, "Indoor optical wireless MIMO system with an imaging receiver," *IEEE Photonics Technology Letters*, vol. 23, no. 2, pp. 97–99, 2011.

[47] M. Z. Afgani, H. Haas, H. Elgala, and D. Knipp, "Visible light communication using OFDM," in *2nd International Conference on Testbeds and Research Infrastructures for the Development of Networks and Communities, TRIDENTCOM .* IEEE, 2006, pp. 6–pp.

[48] H. Elgala, R. Mesleh, and H. Haas, "Indoor broadcasting via white LEDs and OFDM," *IEEE Transactions on Consumer Electronics*, vol. 55, no. 3, pp. 1127–1134, August 2009.

[49] D. Tsonev, H. Chun, S. Rajbhandari, J. McKendry, S. Videv, E. Gu, M. Haji, S. Watson, A. Kelly, G. Faulkner, M. Dawson, H. Haas, and D. O'Brien, "A 3-Gb/s Single-LED OFDM-Based Wireless VLC Link Using a Gallium Nitride μLED," *IEEE Photonics Technology Letters, vol.* 26, *no.* 7, *pp.*637 − −640, *April*2014.

[50] M. E. Van Valkenburg, *Reference Data for Engineers: Radio, Electronics, Computers and Communications*, 9th ed. Massachusetts: Newnes, 2001.

[51] E. Charbon and S. Donati, "SPAD sensors come of age," *Optics & Photonics News*, vol. 21, no. 2, p. 34, 2010.

[52] S. Cova, M. Ghioni, A. Lacaita, C. Samori, and F. Zappa, "Avalanche photodiodes and quenching circuits for single-photon detection," *Applied optics*, vol. 35, no. 12, pp. 1956–1976, 1996.

[53] E. Fisher, I. Underwood, and R. Henderson, "A reconfigurable 14-bit 60 GPhoton/s single-photon receiver for visible light communications," in *2012 Proceedings of the ESSCIRC*. IEEE, 2012, pp. 85–88.

[54] ——, "A reconfigurable single-photon-counting integrating receiver for optical communications," *IEEE Journal of Solid-State Circuits*, vol. 48, no. 7, pp. 1638–1650, July 2013.

[55] I. Alsolami and D. O'Brien, "Multiresolution PPM for broadcasting over asymmetric photon counting channels," *IEEE Communications Letters*, vol. 15, no. 12, pp. 1268–1270, 2011.

[56] I. Alsolami, D. Chitnis, D. O'Brien, and S. Collins, "Broadcasting over photon-counting channels via multiresolution PPM: Implementation and experimental results," *IEEE Communications Letters*, vol. 16, no. 12, pp. 2072–2074, 2012.

[57] B. Culshaw, A. Mignani, and R. Riesenberg, *Optical Sensing*, ser. Proceedings of SPIE - the International Society for Optical Engineering. SPIE, 2004, no. v. 5459.

[58] E. Fisher, I. Underwood, and R. Henderson, "A reconfigurable single-photon-counting integrating receiver for optical communications," *IEEE Journal of Solid-State Circuits*, vol. 48, no. 7, pp. 1638–1650, 2013.

[59] R. H. Hadfield, "Single-photon detectors for optical quantum information applications," *Nature photonics*, vol. 3, no. 12, pp. 696–705, 2009.

[60] K. Han and G. Zhao, *Hydrogen Bonding and Transfer in the Excited State*. John Wiley & Sons, 2011.

[61] P. Seitz and A. Theuwissen, *Single-Photon Imaging*, ser. Springer Series in Optical Sciences. Springer, 2011.

[62] B. F. Aull, A. H. Loomis, D. J. Young, R. M. Heinrichs, B. J. Felton, P. J. Daniels, and D. J. Landers, "Geiger-mode avalanche photodiodes

for three-dimensional imaging," *Lincoln Laboratory Journal*, vol. 13, no. 2, pp. 335–349, 2002.

[63] G.-F. Dalla Betta, L. Pancheri, D. Stoppa, R. Henderson, and J. Richardson, "Avalanche photodiodes in submicron CMOS technologies for high-sensitivity imaging," *Advances in Photodiodes InTechOpen*, 2011.

[64] A. Karlsson, M. Bourennane, G. Ribordy, H. Zbinden, J. Brendel, J. Rarity, and P. Tapster, "A single-photon counter for long-haul telecom," *Circuits and Devices Magazine, IEEE*, vol. 15, no. 6, pp. 34–40, 1999.

[65] S. Tudisco, F. Musumeci, L. Lanzano, A. Scordino, S. Privitera, A. Campisi, L. Cosentino, G. Condorelli, P. Finocchiaro, G. Fallica, S. Lombardo, M. Mazzillo, D. Sanfilippo, and E. Sciacca, "A new generation of SPAD - single-photon avalanche diodes," *IEEE Sensors Journal*, vol. 8, no. 7, pp. 1324–1329, July 2008.

[66] A. Migdall, S. V. Polyakov, J. Fan, and J. C. Bienfang, *Single-Photon Generation and Detection: Physics and Applications*. Academic Press, 2013, vol. 45.

[67] M. Larsen and A. Kostinski, "Simple dead-time corrections for discrete time series of non-Poisson data," *Measurement Science and Technology*, vol. 20, no. 9, September 2009.

[68] H. Hemmati, *Deep space optical communications*. New Jersey: John Wiley & Sons, 2006.

[69] R. M. Gagliardi and K. Sherman, *Optical Communications*, 2nd ed. New York: John Wiley & Sons, 1995.

[70] C. E. Shannon, "A mathematical theory of communication," *Bell Systems Technical Journal*, vol. 27, 1948.

[71] S. Dolinar, B. Erkmen, B. Moision, K. Birnbaum, and D. Divsalar, "The ultimate limits of optical communication efficiency with photon-counting receivers," in *IEEE International Symposium on Information Theory Proceedings (ISIT)*, July 2012, pp. 541–545.

[72] M. Jeruchim, P. Balaban, and K. Shanmugan, *Simulation of Communication Systems: Modeling, Methodology and Techniques*, ser. Information Technology Series. Springer, 2000.

[73] J. Pierce, E. C. Posner, and E. R. Rodemich, "The capacity of the photon counting channel," *IEEE Transactions on Information Theory*, vol. 27, no. 1, pp. 61–77, January 1981.

[74] R. M. Gagliardi and S. Karp, "M-ary poisson detection and optical communications," *IEEE Transactions on Communication Technology*, vol. 17, no. 2, pp. 208–216, 1969.

[75] M. Charbit and C. Bendjaballah, "Efficient capacity for a PPM weak noisy photon-counting channel," *Optical and quantum electronics*, vol. 18, no. 1, pp. 49–55, 1986.

[76] R. McEliece, "Practical codes for photon communication," *IEEE Transactions on Information Theory*, vol. 27, no. 4, pp. 393–398, July 1981.

[77] M. R. Bell and S.-M. Tseng, "Capacity of the low-photon-rate direct-detection optical pulse-position-modulation channel in the presence of noise photons," *Applied optics*, vol. 39, no. 11, pp. 1776–1782, 2000.

[78] A. S. Fletcher, "High-efficiency error correction for photon counting," *LINCOLN LABORATORY JOURNAL*, vol. 18, no. 2, 2010.

[79] T. Xie, S. Wilson, M. Brandt-Pearce, and C. Brown, "LDPC code design for OOK modulated Poisson optical channels," in *47th Annual Conference on Information Sciences and Systems (CISS)*, March 2013, pp. 1–6.

[80] Y. Li and Z. Xu, "Transmitted reference schemes for wireless optical communications," in *Global Telecommunications Conference. GLOBECOM '06. IEEE*, 2006, pp. 1–5.

[81] B. Moision and J. Hamkins, "Deep-space optical communications downlink budget: Modulation and coding," *Interplanetary Network Progress Report 42-154: Jet Propulsion Laboratory*, August 2003.

[82] G. Cancellieri, "Transmission efficiency in photon counting channels," *IEEE Transactions on Communications*, vol. 37, no. 2, pp. 183–187, 1989.

[83] Advanpix, "Multiprecision Computing Toolbox for MATLAB ," April 2014. [Online]. Available: http://www.advanpix.com/

[84] J. Hamkins, "Accurate computation of the performance of M-ary orthogonal signaling on a discrete memoryless channel," *IEEE Transactions on Communications*, vol. 52, no. 11, pp. 1844 – 1845, November 2004.

[85] T. M. Cover and J. A. Thomas, *Elements of Information Theory*, 2nd ed. New York: John Wiley & Sons, 2006.

[86] H. Hemmati, *Near-Earth Laser Communications*. CRC Press, 2009.

[87] R. G. Gallager, *Information Theory and Reliable Communication,*. New York: John Wiley & Sons, 1968.

[88] F. Chapeau-Blondeau, "Noise-enhanced capacity via stochastic resonance in an asymmetric binary channel," *Phys. Rev. E*, vol. 55, pp. 2016–2019, Feb 1997.

[89] D. O'Brien, G. Parry, and P. Stavrinou, "Optical hotspots speed up wireless communication," *Nature Photonics*, vol. 1, no. 5, pp. 245–247, 2007.

[90] S. Hranilovic, *Wireless optical communication systems*. Springer, 2005.

[91] T. Cover, "Broadcast channels," *IEEE Transactions on Information Theory*, vol. 18, no. 1, pp. 2 – 14, 1972.

[92] K. Ramchandran, A. Ortega, K. M. Uz, and M. Vetterli, "Multiresolution broadcast for digital HDTV using joint source/channel coding,"

IEEE Journal on Selected Areas in Communications, vol. 11, no. 1, pp. 6–23, 1993.

[93] P. Vitthaladevuni and M.-S. Alouini, "BER computation of 4/M-QAM hierarchical constellations," *IEEE Transactions on Broadcasting*, vol. 47, no. 3, pp. 228–239, September 2001.

[94] ——, "Exact BER computation of generalized hierarchical PSK constellations," *IEEE Transactions on Communications*, vol. 51, no. 12, pp. 2030–2037, December 2003.

[95] ——, "A closed-form expression for the exact BER of generalized PAM and QAM constellations," *IEEE Transactions on Communications*, vol. 52, no. 5, pp. 698–700, May 2004.

[96] European Broadcasting Union, "Digital video broadcasting (DVB); second generation framing structure, channel coding and modulation systems for broadcasting, interactive services, news gathering and other broadband satellite applications (DVB-S2)," *European Standard (Telecommunications Series)*, 2013.

[97] ——, "Digital video broadcasting (DVB); framing structure, channel coding and modulation for satellite services to handheld devices (SH) below 3 GHz," *European Standard (Telecommunications Series)*, 2010.

[98] ——, "Digital video broadcasting (DVB); Framing structure, channel coding and modulation for digital terrestrial television," *European Standard (Telecommunications Series)*, 2004.

[99] H. Datta and J. Ilow, "UEP framework in multiresolution modulation for robust image broadcasting," in *IEEE 22nd International Symposium on Personal Indoor and Mobile Radio Communications (PIMRC)*, September 2011, pp. 551–555.

[100] C. Hellge, S. Mirta, T. Schierl, and T. Wiegand, "Mobile TV with SVC and hierarchical modulation for DVB-H broadcast services," in *IEEE International Symposium on Broadband Multimedia Systems and Broadcasting. BMSB '09.*, May 2009, pp. 1–5.

[101] R. Papannareddy, *Lightwave Communications Systems: A Practical Perspective*. Penram International Publishing, 2004.